Dissertation

Numerical investigations on the two-phase ignition hypothesis triggering low-speed pre-ignitions in boosted SI engines

Ausgeführt zum Zwecke der Erlangung des akademischen Grades eines Doktors der technischen Wissenschaften, eingereicht an der Technischen Universität Wien Fakultät für Maschinenwesen und Betriebswissenschaften

von

DI Norbert Zöbinger

[redacted]

Unter der Leitung von

Prof. Dr. Thomas Lauer

Institut für Fahrzeugantriebe und Automobiltechnik
Technische Universität Wien

Begutachtet von

Prof. Dr. Thomas Koch

Institut für Kolbenmaschinen

Karlsruher Institut für Technologie

Prof. Dr. Michael Harasek

Institut für Verfahrenstechnik, Umwelttechnik und technische Biowissenschaften

Technische Universität Wien

Eidesstattliche Erklärung

Ich habe zur Kenntnis genommen, dass ich zur Drucklegung meiner Arbeit unter der Bezeichnung

Numerical investigations on the two-phase ignition hypothesis triggering low-speed pre-ignitions in boosted SI engines

nur mit Bewilligung der Prüfungskommission berechtigt bin. Ich erkläre weiters an Eides statt, dass ich meine Dissertation nach den anerkannten Grundsätzen für wissenschaftliche Arbeiten selbständig ausgeführt habe und alle verwendeten Hilfsmittel, insbesondere die zugrunde gelegte Literatur genannt habe.

Weiters erkläre ich, dass ich dieses Dissertationsthema bisher weder im In- noch im Ausland (einer Beurteilerin / einem Beurteiler zur Begutachtung) in irgendeiner Form als Prüfungsarbeit vorgelegt habe und dass diese Arbeit mit der von den Begutachtern beurteilten Arbeit übereinstimmt.

Ich nehme zur Kenntnis, dass die vorgelegte Arbeit mit geeigneten und dem derzeitigen Stand der Technik entsprechenden Mitteln (Plagiat-Erkennungssoftware) elektronisch-technisch überprüft wird. Dies stellt einerseits sicher, dass bei der Erstellung der vorgelegten Arbeit die Qualitätsvorgaben im Rahmen der geltenden Regeln zur Sicherung guter wissenschaftlicher Praxis „Code of Conduct“ an der TU Wien eingehalten wurden. Zum anderen werden durch einen Abgleich mit anderen studentischen Abschlussarbeiten Verletzungen meines persönlichen Urheberrechts vermieden.

Wien, am 21.07.2022 _____

Zöbinger Norbert

Danksagung

Die vorliegende Arbeit entstand während meiner Tätigkeit als Universitäts- und Projektassistent am Institut für Fahrzeugantriebe und Automobiltechnik der Technischen Universität Wien.

Dem Institutsvorstand Prof. Dr. Bernhard Geringer danke ich für die Möglichkeit, dass ich im Simulationsteam des Instituts an aktuellen Forschungsthemen mitwirken durfte. Ein besonderer Dank gilt Prof. Dr. Thomas Lauer für die wissenschaftliche Betreuung und fachliche Unterstützung. Weiters gilt mein Dank Prof. Dr. Thomas Koch und Prof. Dr. Michael Harasek für die Bereitschaft der Begutachtung dieser Arbeit.

Meinem Projektkollegen Thorsten Schweizer (IFKM, KIT) möchte ich für seinen besonderen Einsatz bei der Durchführung der experimentellen Untersuchungen am optischen Motorenprüfstand und die stets produktive Zusammenarbeit bei wissenschaftlichen Veröffentlichungen danken.

Weiters möchte ich mich bei meinen Kollegen am Institut, insbesondere bei Jens Frühhaber, Johannes Höflinger, Max Quissek und Christoph Steindl sehr herzlich für die schöne Zeit, angenehme Arbeitsatmosphäre und die unzähligen fachlichen Diskussionen bedanken. Ich bin sehr froh, jeden von ihnen kennengelernt zu haben.

Abschließend möchte ich mich bei meiner Familie für ihr vertrauen in mich bedanken. Ganz besonders hervorheben möchte ich meine Frau Mildred, die mich in diesen entbehrungsreichen Zeiten stets unterstützt hat und immer für mich da ist.

Abstract

Although there is an ongoing diversification in propulsion systems for passenger cars, there is still a need for efficient, clean, and powerful internal combustion engines in the near future. In the case of SI engines, the concept of downsizing and downspeeding is a successful approach to improve fuel efficiency and engine torque while fulfilling emission targets. However, investigations have shown that the stochastic occurrence of premature ignitions limits the achievable cylinder pressures during a transient as well as steady-state engine operation. The root cause of this phenomenon is not yet clarified. Based on optical observations inside the combustion chamber, the literature suggests that it is most likely a two-phase phenomenon. However, there are different hypotheses regarding the actual initiator, whether it is a detached oil droplet or a solid particle.

This work comprises a systematic numerical study of the entire process chain leading to LSPI, considering liquid and solid ignition sources. Therefore, the physical and chemical processes inside the combustion chamber were analyzed using 2D & 3D-CFD simulation, including reaction kinetic models accompanied by experimental data.

In order to determine the thermodynamic conditions inside the combustion chamber, a 3D-CFD engine model was established. To account for the physical interaction of the fuel spray with in-cylinder walls as well as the fuel evaporation and vapor distribution, an 11-component fuel surrogate model was introduced. The selection of the components was based on a validated 0D distillation model. The droplet impingement and film accumulation were validated against optical testbed measurements performed at the KIT University. The investigation of the mixture preparation revealed a correlation between the formation of liquid fuel puddles and LSPI occurrence. Especially, accumulations near the piston crevice significantly increased the observable frequency, indicating the importance of lubricating oil during sub-stoichiometric combustion resulting in deposit formation.

Based on this model, the ignition risk of oil droplets and solid particles was investigated using a statistical object release approach. By post-processing the thermodynamic evolution along possible trajectories inside the combustion chamber, the ignition risk is calculated using reaction kinetic sub-models. In the case of oil droplets, the evaporation behavior is modeled using a 4-component surrogate based on a gas chromatography measurement. The chemical reactivity was modeled using the well-studied n-heptane chemistry. While oil droplets accelerate ignition processes by supplying reactive species, particles mainly induce ignition by heat transfer. Therefore, they were generalized by a hot surface transferring heat to a reactive ambient gas phase. The fuel reactivity was modeled in both cases using a TRF surrogate according to RON / MON measurements.

The numerical analysis showed that oil droplet-induced pre-ignition is very unlikely considering the thermodynamic conditions of small-displacement SI engines in highly boosted operation points. In the case of solid particles, a minimum temperature threshold could be evaluated. Studies on inert particles have shown that only reactive particles reach the necessary temperature to ignite the mixture due to exothermic surface reactions. Furthermore, the reduction of particles due to the gas exchange limits the number of pre-heating conventional combustions.

The presented methods and the validated numerical models enable a detailed analysis of the two-phase induced pre-ignition phenomenon. Therefore, these results and methods can be used in the development process of future SI-engines to reduce CO2 emissions.

Kurzfassung

Der Bereich der Antriebssysteme für PKW-Anwendungen unterliegt aktuell einem ständigen Wandel, jedoch besteht auch in der nahen Zukunft weiterhin der Bedarf an effizienten, sauberen and leistungsstarken Verbrennungskraftmaschinen. Bei Ottomotoren ist das Konzept des Downsizing und Downspeeding ein erfolgsversprechender Ansatz zur Verbesserung der Kraftstoffeffizienz und des Motordrehmoments bei gleichzeitiger Erfüllung der Emissionsziele. Untersuchungen haben jedoch gezeigt, dass das stochastische Auftreten von Frühzündungen (LSPI) die erreichbaren Zylinderdrücke im transienten sowie im stationären Motorbetrieb begrenzen. Die eigentliche Ursache dieses Phänomens ist noch nicht geklärt. Basierend auf optischen Beobachtungen innerhalb der Brennkammer legt die Literatur nahe, dass es sich höchstwahrscheinlich um ein Zwei-Phasen-Phänomen handelt. Über den Initiator selbst gibt es unterschiedliche Hypothesen, die entweder abgelöste Öltropfen oder feste Partikel als Ursache in Betracht ziehen.

Diese Arbeit umfasst daher eine systematische numerische Untersuchung der gesamten LSPI auslösenden Prozesskette, unter Berücksichtigung flüssiger und fester Zündquellen. Die physikalischen und chemischen Prozesse innerhalb des Brennraums wurden mithilfe von 2D- und 3D-CFD Simulationen, unter zusätzlicher Einbindung reaktionskinetischer Modelle, analysiert. Weiters wird die Entwicklung der numerischen Modelle durch experimentell gewonnene Daten unterstützt.

Zur Bestimmung der thermodynamischen Verhältnisse im Brennraum wurde ein 3D-CFD-Motormodell erstellt. Um die physikalische Wechselwirkung des Kraftstoffsprays mit den Zylinderwänden sowie die Verdampfung und Verteilung des Gemisches zu berücksichtigen, wurde ein 11-Komponenten-Kraftstoff-Ersatzmodell eingeführt. Die Auswahl der Komponenten basierten auf einem validierten 0D Destillationsmodell. Der Tröpfchenaufprall und die Filmbildung wurden anhand optischer Prüfstandsmessungen validiert, die an der Universität KIT durchgeführt wurden. Die Untersuchung der Gemischbildung zeigte eine Korrelation zwischen der Bildung von Kraftstofffilmen und dem Auftreten von LSPI. Insbesondere Ansammlungen von Kraftstoff nahe des Kolbenringspalts steigerten die beobachtbare Frequenz signifikant, was die Bedeutung des Schmieröls während der unterstöchiometrischen Verbrennung und daraus resultierenden Ablagerungsbildung unterstreicht.

Basierend auf diesem Modell wurde das Zündrisiko von Öltröpfchen und festen Partikeln mit einem statistischen Zwei-Phasen-Freisetzungsansatz untersucht. Durch Auswerten der thermodynamischen Verläufe entlang möglicher Trajektorien durch den Brennraum wurde das Zündrisiko unter Verwendung von reaktionskinetischen Untermodellen berechnet. Bei Öltröpfchen wurde das Verdampfungsverhalten mit einem 4-Komponenten-Ersatzmodell basierend auf einer gaschromatographischen Analyse modelliert. Die chemische Reaktivität wurde anhand von n-Heptan modelliert. Während Öltropfen Zündprozesse durch reaktive Spezies beschleunigen, ist der Wärmeübergang bei heißen Partikeln der entscheidende Faktor. Daher können Partikel durch eine wärmeübertragende Oberfläche an ein reaktives Medium verallgemeinert werden. Die Reaktionskinetik des Kraftstoffes wurde in beiden Fällen durch ein TRF-Ersatzfluid, unter Einbeziehung von ROZ / MOZ Messungen, modelliert.

Die numerische Analyse zeigte, dass eine öltröpfcheninduzierte Frühzündung unter den thermodynamischen Bedingungen von kleinvolumigen Ottomotoren in hochaufgeladenen Betriebspunkten als sehr unwahrscheinlich einzustufen ist. Im Fall von heißen Partikeln konnte eine minimale Grenztemperatur ermittelt werden. Eine detaillierte Analyse der thermodynamischen Einflussparameter zeigte Hinweise darauf, dass ein zündauslösendes Partikel selbst eine chemische Wärmefreisetzung ermöglichen könnte. Untersuchungen an inerten Partikeln haben gezeigt, dass nur

reaktive Partikel durch exotherme Reaktionen die notwendige Oberflächentemperatur erreichen, um das umgebende Gemisch zu entzünden. Darüber hinaus reduziert der Ladungswechsel die Partikelanzahl mit jedem Arbeitsspiel signifikant. Folglich ist die Anzahl an vorkonditionierenden konventionellen Verbrennungszyklen begrenzt.

Die vorgestellten Methoden und die validierten numerischen Modelle ermöglichen eine detaillierte Analyse des Phänomens der Zwei-Phasen induzierten Frühzündung (LSPI). Daher können diese Ergebnisse und Methoden im Entwicklungsprozess zukünftiger Ottomotoren zur Reduzierung der CO_2 Emissionen einen Beitrag leisten.

Contents

Nomenclature and Abbreviations

Variable	Description	Unit
$\dot{Q}_{LF}$	Enthalpy source/sink (liquid film)	[J/s]
$\vec{S}_{src}$	Momentum source/sink vector	[N/m²]
$\dot{m}_{eff}$	Effective mass flow	[kg/s]
$\dot{m}_{src}$	Mass source/sink	[kg/s]
$\dot{m}_{th}$	Theoretical mass flow	[kg/s]
$\vec{u}_{LF}$	Velocity vector (liquid film)	[m/s]
$\vec{u}_{d}$	Velocity vector (droplet)	[m/s]
$\vec{u}_{g}$	Velocity vector (gas-phase)	[m/s]
Δh_v	Enthalpy of vaporization	[J/kg]
ΔH_R	Enthalpy difference of chemical reaction	[J/kg]
Δt_{TS}	Time step size	[s]
h_{LF}	Enthalpy (liquid film)	[J/kg]
A_{eff}	Effective nozzle cross-section	[m²]
A_{geo}	Nozzle cross-section (geometric)	[m²]
A_i	Area	[m²]
$A_{s,i}$	Droplet or particle surface area	[m²]
D_2, D_3	Vapor mass flow (0D Distillation model)	[kg/s]
D_{AB}	Binary diffusion coefficient	[m²/s]
D_i	Diameter	[m]
$K_{g,i}$	Mass transfer coefficient of species i	[-]
M_i	Molar mass of species i	[kg/kmol]
Q_s	Surface heat transfer	[J]
R_C	Critical spherical radius	[m]
R_k, Q_k	Group k volume and area parameter	[-]
THK_{LF}	Liquid film thickness	[m]
THK_{lam}	Laminar flame thickness	[m]
T_{LF}	Temperature (liquid film)	[K]
T_P	Temperature particle	[K]
T_d	Temperature droplet	[K]
T_i	Temperature	[K]
V_i	Volume	[m³]
a_{mn}	Group interaction parameter between groups (UNIFAC model)	[-]
c_A	Area coefficient (nozzle)	[-]
c_d	Discharge coefficient (nozzle)	[-]
$c_{p,i}$	Specific heat capacity	[J/kgK]
c_v	Velocity coefficient (nozzle)	[-]
c_w	Drag coefficient	[-]
k_i	Conductivity	[W/mK]
m_i	Mass	[kg]
nc	Total number of components in the mixture (UNIFAC model)	[-]
$ng(i)$	Total number of groups in component I (UNIFAC model)	[-]
p_i	Pressure	[bar]
$p_{vap,i,\infty}$	Partial pressure of species i (far field)	[bar]
$p^s_{vap,i}$	Saturation pressure of species i	[bar]
s_L	Laminar flame speed	[m/s]
s_T	Turbulent flame speed	[m/s]
t_{ign}	Time at ignition	[°CA], [s]
v^i_k	Group k number in component I (UNIFAC model)	[-]
$x_{i,l}$	Molar fraction of species i (liquid phase)	[-]
y_i	Molar fraction of species i (gas phase)	[-]
γ_i	UNIFAC activity coefficient	[-]
γ_i^C	UNIFAC activity coeffient contribution due to combinatoric interactions	[-]
γ_i^R	UNIFAC activity coeffient contribution due to molecular interactions	[-]
ν_i	Kinematic viscosity	[Pa*s]
ρ_i	Density	[kg/m³]

τ_{LF}	Stress tensor within the liquid film	[N/m²]
τ_{ign}	Ignition delay integral	[-]
λ	Air-fuel equivalence ratio	[-]
λ_{TRF}	Air-fuel equivalence ratio (TRF-surrogate)	[-]
δ	Dirac delta function	[-]
φ	Degree crank angle	[°CA]
aTDCf	After top dead center firing	[°CA]
BDC	Bottom dead center	-
BEV	Battery electric vehicle	-
BMEP	Brake mean effective pressure	[bar]
bTDCf	Before top dead center firing	[°CA]
CDF	Cumulated density function	[-]
CFD	Computational fluid dynamics	-
DDM	Discrete droplet method	-
DI	Direct injection	-
DNS	Direct numerical simulation	-
DoE	Design of Experiment	-
DOHC	Double overhead camshaft	-
DV90	90% of the spray volume fall below that diameter threshold	[µm]
ECN	Engine combustion network	-
EOS	Equation of State	-
EVC	Exhaust valve close	-
EVO	Exhaust valve open	-
GC	Gas chromatography	-
HEV	Hybrid electric vehicle	-
HS	High-Speed	-
HTHS	High-Temperature high-Shear	-
ICE	Internal combustion engine	-
IGN	Ignition timing	[°CA]
IVC	Intake valve close	-
IVO	Intake valve open	-
Le	Lewis number	[-]
LED	Light-emitting diode	-
LIF	Light induced fluorescence	-
LP-F	Long-pass filter	-
LSPI	Low-speed premature ignition	-
M	Torque-Testbed measurement	[Nm]
MFB	Mass fraction burned	[-]
MLbV	Modified Liquid-by-Volume Method	-
MON	Motor octane number	[-]
NBP	Normal boiling point	[K]
NTC	Negative temperature coefficient	-
PDA	Phase Doppler Anemometry	-
PHEV	Plug-in hybrid electric vehicle	-
RANS	Reynolds averaged Navier-Stokes	-
RCM	Rapid compression machine	-
Re	Reynolds number	[-]
RNG	Renormalization group (name of the turbulence model)	-
RON	Research octane number	[-]
rpm	Revolutions per minute	-
RT	Release timing	[°CA]
Sc	Schmidt number	[-]
SI	Spark ignition	-
SMD	Sauter mean diameter	[µm]
SOI	Start of injection	[°CA]
T_G	Gas Temperature	[K]
TGA	Thermal gravimetric analysis	-
TKE	Turbulent kinetic energy	[m²/s²]
T_L*	Leidenfrost temperature limit (liquid film model)	[K]
TRF	Toluene reference fuel (mixture of Iso-octane, n-heptane, and toluene)	-
T_S*	Deposition temperature limit (liquid film model)	[K]

VF	Volume fraction	[-]
VLE	Vapor-liquid equilibrium	-
VoF	Volume-of-Fluid (two phase simulation approach)	-
WOT	Wide open throttle (full load)	-

1. Introduction

Over the last years, environmental protection and reducing global warming have become key challenges of our time. The CO_2 emissions have been rising linearly in the previous 50 years due to increasing energy demands. [1] One of the major contributors to the total CO_2 emission is the road transportation sector accounting for a share of ~19 % of the total emissions, shown in Figure 1.1.

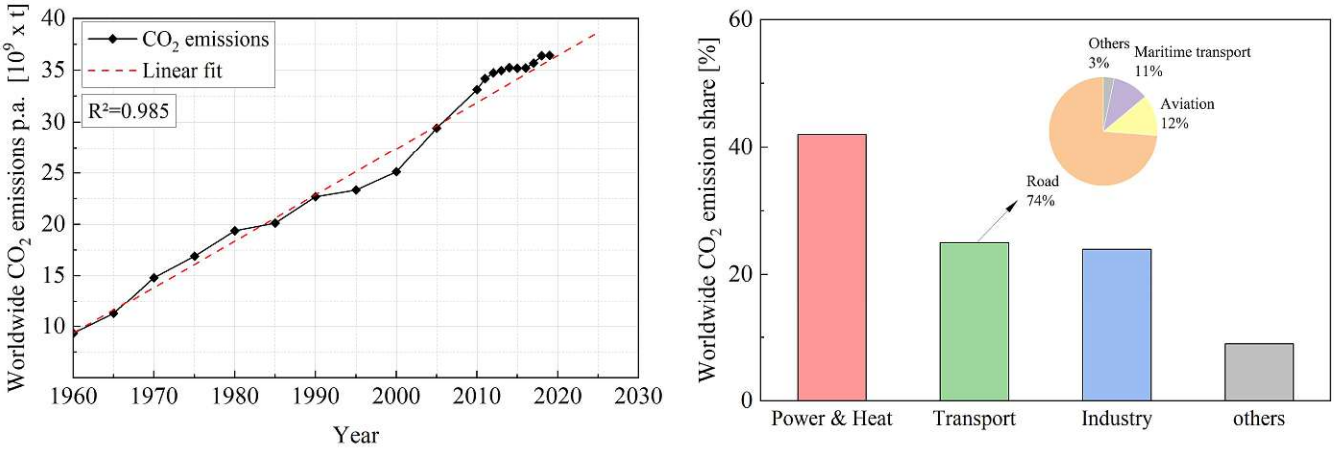

(**a**) (**b**)

Figure 1.1:(**a**) Temporal evolution of the annual worldwide CO_2 emissions [1], (**b**) Distribution of the total CO_2 emission in 2018 [1].

In order to reduce the effect of global warming resulting from road traffic, the EU introduced an average CO_2 fleet emission limit extending the current regulations on tail pipe emissions. The emission threshold is decreasing step-by-step from currently 95 g/km (4,1 l RON95/100km) to 61,75 g/km (2,7 l RON95/100km) in 2030 [1, 2]. This stringent regulation leads to diversification and electrification of propulsion systems since it is evaluated using a "tank-to-wheel" approach. Therefore, all environmental benefits resulting from climate-neutral produced fuels ("eFuels" or "ReFuels") are neglected in the current legislation. Nevertheless, considering the market share of sold new vehicles in 2020, it appears that ~92 % of all propulsion systems in Europe are using internal combustion engines (ICE), as shown in Figure 1.2. Although forecasts predict a decreasing share, the majority of powertrains will incorporate ICE as their main or secondary power source in the near future. [3, 4, 5] Therefore, the development of efficient engines can contribute significantly to environmental protection.

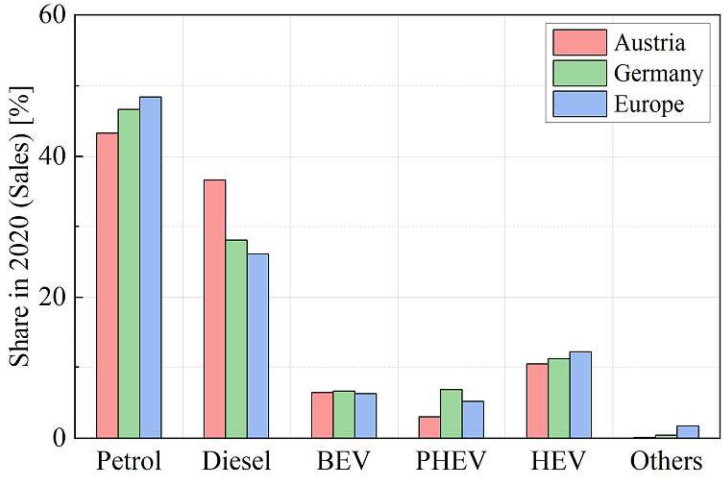

Figure 1.2: Share of the propulsion system in 2020 [1].

In the case of SI-engines, the concept of downsizing and downspeeding is a successful approach that has been introduced. These concepts aim to shift the main operating range towards higher mean effective pressures (BMEP) by reducing the engine displacement and utilizing longer gear ratios. This measure decreases friction and pumping losses due to engine throttling in frequently used part-load operation conditions. In order to maintain full load engine performance, air boosting is necessary to increase charge density. As a result, the thermal and mechanical load raises, leading to higher TDC pressure and temperature levels. Therefore, the so-called degree of downsizing is limited by the occurrence of irregular combustion phenomena.

Besides well-known gas-phase induced autoignitions like knocking, premature ignitions (PIs) have been observed recently at low-end torque operation conditions. Whereas a smooth transition between conventional and knocking combustions can be observed, the appearance of PIs is of statistical nature. The undesired early ignition timing results in severe knocking combustion ("mega-knock") surpassing 200 bar peak cylinder pressure. Such high mechanical loads lead to an increased engine damage potential, especially of pistons, piston rings and -carriers, and connecting rods. The unpredictability of these events inhibits effective countermeasures and limits the efficiency potentials of SI engines.

2. State of knowledge and research

2.1. Irregular combustion phenomena

The striving toward highly efficient SI engines led to combustion concepts using high compression ratios and boost pressures. Both measures increase the temperature and pressure level inside the combustion chamber, resulting in enhanced chemical kinetics of the pre-mixed fuel-air cylinder charge. As a result, SI engines are prone to irregular combustion phenomena, especially under wide-open throttle (WOT) conditions.

The irregular combustions can be categorized by the appearance during the engine cycle relative to spark timing (pre- vs. post-ignition) and the type of induced combustion (autoignition/detonation vs. deflagration). Furthermore, transitions between different categories are possible, resulting in various sub-types of abnormal combustion phenomena.

Three important representatives of irregular combustions concerning downsized engines are engine spark knock, surface ignition, and more recent low-speed pre-ignitions (LSPI).

2.1.1. Engine knock & surface ignition

Engine knock was first documented and named by Clerk [6] in 1882, who recognized a metallic, pinging combustion noise during an engine run. It describes the autoignition in portions of the unburnt gas phase ahead of a propagating deflagrative flame front regardless of the ignition source. [7, 8] The sudden heat release of the mixture results in an inhomogeneous pressure field. This generates propagating pressure waves through the combustion chamber, causing the typical oscillating measurement signals. The autoignition of the end gas is a reaction kinetic controlled phenomenon and is significantly influenced by the ignition timing. An early heat release raises the temperature and pressure level and thus reduces the ignition delay time. In the case of spark knock[1], the retardation of the desired ignition timing is an effective countermeasure at the cost of thermal efficiency, shown in Figure 2.1 (**a**).

The deterioration of the thermal boundary layer due to the induced oscillating near-wall flows enhances the wall heat transfer. [9, 10, 11, 12, 13, 14] In the case of ongoing knocking cycles, insufficiently cooled combustion chamber wall regions suffer from elevated temperature levels enabling surface-induced premature ignitions. Such early induced deflagrative flames and thus heat release result in elevated gas pressure and temperature levels, advancing the knock onset and consequently increasing knock intensity. This self-amplifying effect is known as “thermal runaway”, shown in Figure 2.1 (**b**). In combination with the increased mechanical load, this can lead to erosion and melting of exhaust valves, piston top land area, and piston rings. Therefore, excessive engine knock has to be avoided in series production engines.

[1] The flame front initiated by the spark plug

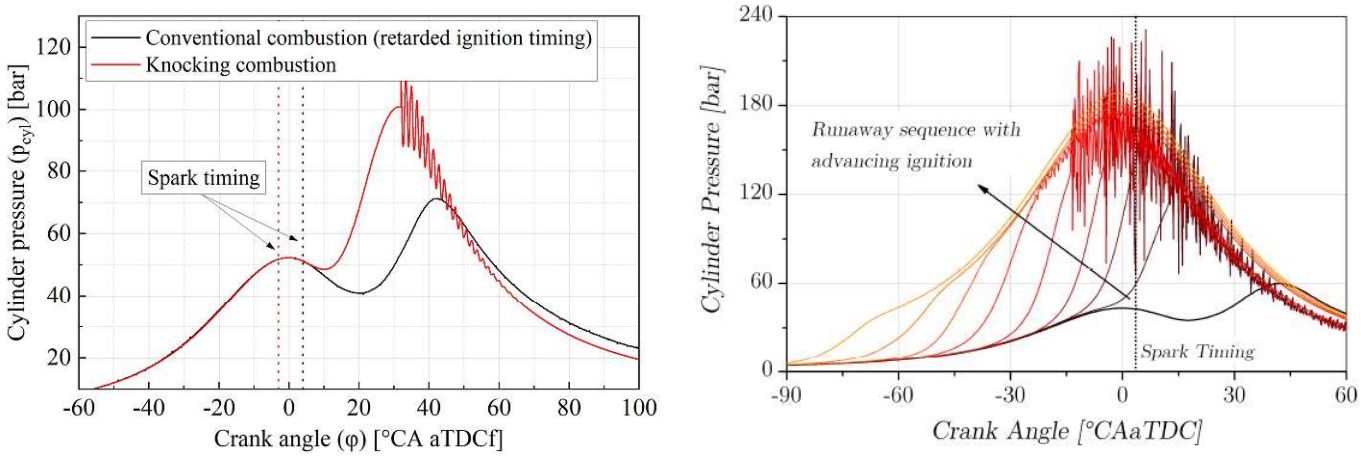

(**a**) (**b**)

Figure 2.1: (**a**) Exemplarily in-cylinder pressure signal of knocking combustion, (**b**) Thermal runaway due to surface ignition, reprinted from [15].

2.1.2. *Low-speed premature ignition (LSPI)*

As the name indicates, low-speed pre-ignitions typically occur at low engine speeds (< 2500 rpm) and high specific engine loads (BMEP > 20 bar). It is characterized by an undesired early ignition initiating a deflagrative flame front leading to violent knocking combustion ("super-knock" or "mega-knock"). [16] In contrast to the surface-induced pre-ignition phenomenon, the appearance of LSPI events is of statistical nature (1-5x / 30,000 cycles) and no self-amplifying effect can be observed. Due to the unpredictability and the lack of preliminary indications, no countermeasures can be applied during engine runs resulting in a possible substantial engine breakdown after a single event.

Despite the statistical nature, LSPIs often appear in sequences or clusters of 1-5 events within several consecutive engine cycles. [15, 17, 18] Typically, such sequences show an intermittent pattern between LSPI and conventional combustions, although no clear and repetitive structures can be observed. Therefore, such clusters are distinguished in initial LSPIs and triggered follow-up events, shown in Figure 2.2.

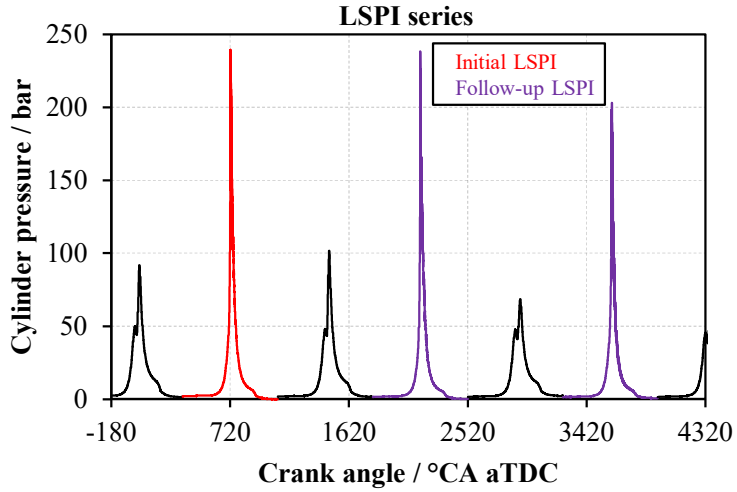

Figure 2.2: Typical sequence of LSPI clusters [18].

2.2. Presumed ignition sources

Many experimental and numerical studies have been carried out in the past to determine the root cause of LSPIs and the influencing effects of engine operating conditions and hardware configurations. Figure 2.3 shows an overview of putative ignition sources.

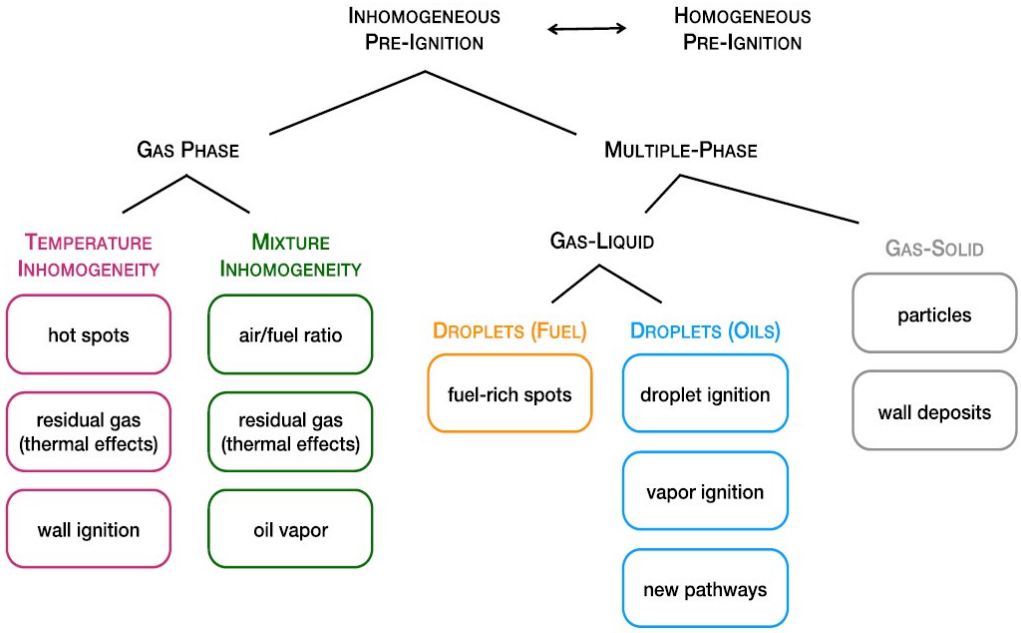

Figure 2.3: Putative ignition sources triggering LSPI events [19].

Regarding the ignition location, the first major findings were reported by Zahdeh [20] using a fiber optical spark plug. He reported a fairly random distribution of ignition locations in the combustion chamber, although a focus of PIs near hot surfaces (spark plug, exhaust valves, piston top land) was found. Kieberger [21] reported a similar observation using high-speed imaging on an optically accessible testbed engine. However, the PI ignition locations did not change significantly after replacing the spark plug with a laser-induced ignition system. Hülser [22] confirms this behavior by running ethanol on a single-cylinder research engine. Dahnz [23] investigated the possibility of gas-phase induced autoignitions due to temperature and air-fuel inhomogeneities numerically. By applying a TRF surrogate fuel (67 vol-% iso-octane, 20 vol-% toluene, 17 vol-% n-heptane[2]) to a homogeneous reactor model, the author found that a gas temperature level above 740 K is necessary to effectively trigger autoignition within 5 ms at 40 bar ambient pressure. Such high gas temperature levels are typically not found during the compression stroke with respect to the rather long time period of 5 ms (= 60 °CA @ 2000 rpm) without considering an external heat source. Günther [24] investigated the ability of hot surfaces to induce a premature ignition by implementing a tunable glow plug in a single-cylinder research engine. The experiments concluded that hot spot-induced ignitions are rather improbable since a glow plug temperature above 1070 K was needed to trigger an LSPI artificially.

[2] Comment from the author: The shown values are taken from the cited literature ([23]). Unfortunately, the sum of the fluid components exceeds 100 % volume fraction.

Further research on optical engine testbeds reveals the presence of light-emitting glowing objects during the compression stroke inside the combustion chamber, indicating a two-phase induced ignition mechanism. Döhler and Pritze [25], Dahnz [23], Kassai [26], and Birkigt [27] suggested that these objects behave like diffusively burning oil-fuel droplets. In contrast, Palaveev [28], Okada [29], and Spicher [30] interpreted them as solid-like glowing structures or particles. However, all authors reported a sharp increase in the number of light-emitting objects after the initial LSPI event. They concluded that the high number of objects results from deposit detachment due to the high-pressure oscillations of the previous "mega-knock" combustion. Figure 2.4 illustrates the situation inside the combustion chamber during the initial LSPI event and the consecutive engine cycle.

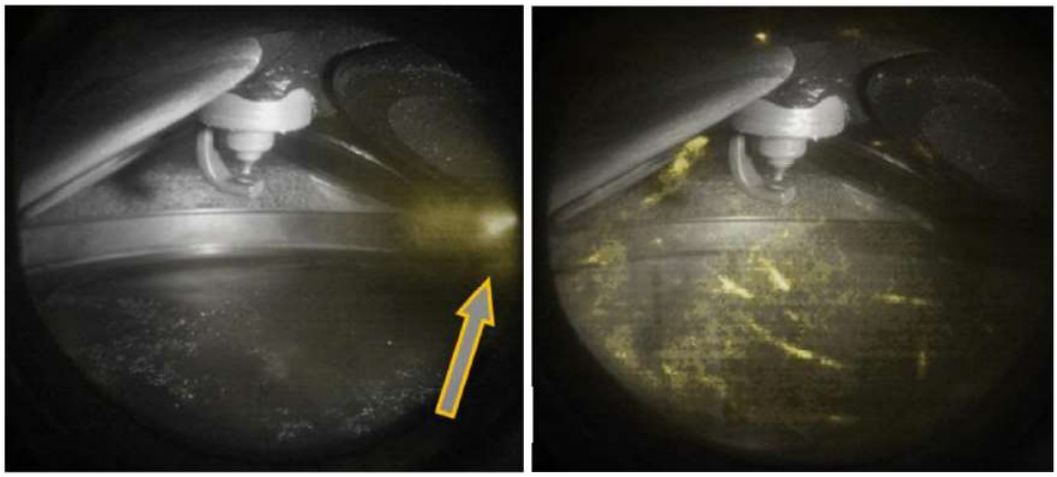

(**a**)

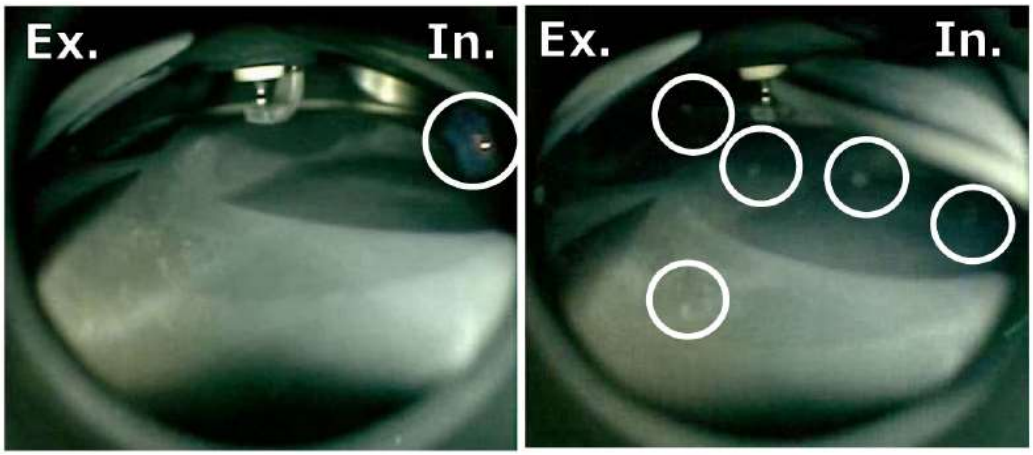

(**b**)

Figure 2.4: In-cylinder high-speed imaging results of the initial LSPI event and the consecutive engine cycle by (**a**) Lauer [31] and (**b**) Okada [29].

Lauer et al [31] and Schünemann [32] suggested that the root cause of the initial event does not have to be the same as for the follow-up LSPI sequence since the situation during the compression stroke differs significantly. Nevertheless, none of the investigations could determine the origin of these objects in the initial and follow-up events, nor could they be identified as liquid droplets or solid-like particles.

Based on these findings, two hypotheses emerged in the literature explaining the mechanism of LSPI.

2.2.1. *Droplet-induced LSPI hypothesis*

This hypothesis assumes that oil-fuel droplets are detached from the piston crevice due to the reciprocating motion of the piston. Such droplets are transported by the in-cylinder flow field and finally act as an ignition source due to the evaporation of fast ignitable hydrocarbons.

The possibility of droplet detachments out of the piston crevice has been investigated by Kassai [26] and Tanaka [33, 34]. Both authors observed droplet detachments under motored (non-fired) conditions with activated (Kassai [26]) and deactivated (Tanaka [33, 34]) fuel injection, shown in Figure 2.5. The droplets were released near TDC, and their diameters were in the range of the piston crevice gap width. Additionally, it could be demonstrated that the fluid viscosity significantly influences the droplet release probability. Tanaka [33, 34] investigated three oil viscosity grades (SAE 0W-20, 10W-30 and 10W-40). He could observe an increased number of droplet detachments from the piston top land and the piston crevice volume using low viscosity lubricating oil. Kassai [26] observed the same relationship when the oil in the piston crevice is diluted with fuel impinged on the cylinder liner. However, the author suggested that the droplet release without oil-fuel dilution seems to be unlikely using an SAE 5W-30 grade oil on the investigated engine configuration.

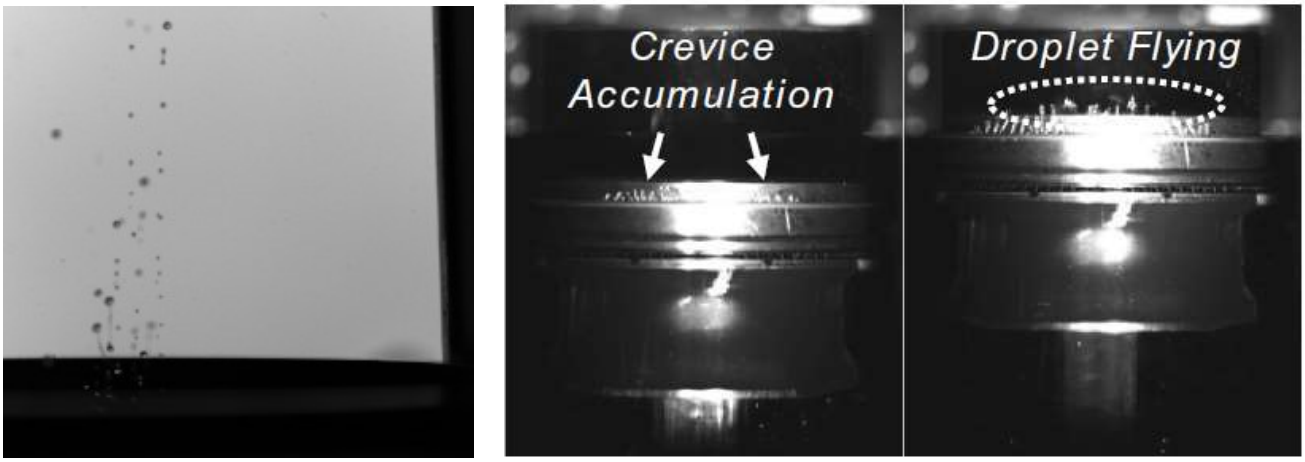

(**a**) (**b**)

Figure 2.5: Droplet detachment under motored (non-fired) conditions. (**a**) SAE 0W-20 without fuel injection (Tanaka [34]), (**b**) SAE 5W-30 with activated fuel injection (Kassai [26]).

Moriyoshi [35] and Doppler [36] could replicate the droplet detachment behavior numerically using a Volume-of-Fluid (VoF) approach. The simulation results showed a transition in detachment behavior depending on the fluid mixture viscosity. Whereas pure lubricating oil tends to slowly creep up towards the piston top land, where the accumulated liquid starts to lift from the piston surface and form a droplet, an increasing share of fuel dilution leads to a more aggressive spilling of the fluid inside the piston crevice volume. Dahnz [23] and Palaveev [37] also found a correlation between the cylinder wall wetting and LSPI-frequency in fired testbench setups, confirming the importance of oil-fuel dilution. Further on, Zahdeh [20] and Singh [38] reported that a split-injection strategy decreases the LSPI-tendency on their investigated engine configurations. However, both authors mentioned that the last injection pulse was somewhat retarded and thus could influence the results. Although the experiments showed similar trends, the explanations found in the CFD analysis were different. Zahdeh [20] observed

an increase in wall wetting, especially near TDC, whereas Singh [38] reported an overall reduction of the film mass. Leach [39] investigated the influence of the fuel evaporation characteristic, represented by the T90 temperature value, on the LSPI probability. The investigation showed that high T90 values enhance LSPI frequency significantly. Additionally, Morikawa [40] and Amann [41] confirmed the importance of fuel accumulations by reducing the coolant temperature operation range. This measure leads to decreased cylinder liner temperature and thus reduces the evaporation rates of accumulated fuel puddles. Consequently, the deactivation of oil jet piston cooling resulted in a reduced LSPI frequency. [42]

Since the piston crevice volume appears to be a decisive region, Amann [43] investigated the influence of the piston crevice shape. He observed that chamfered piston shapes and a decreased piston top land height reduce PI-frequencies by an order of magnitude. He concluded that the propagating flame could penetrate deeper into the piston crevice volume, reducing the cycle-to-cycle accumulation of fluids.

If the boundaries for a droplet detachment are fulfilled, another question arises. Can the detached droplet ignite the mixture? Many investigations were made in rapid compression machines (RCM) to confirm the influence of lubricant oil on the ignition delay time [15, 23, 44, 45, 46, 47]. These experiments showed a significant impact of lubricating oil on the observed ignition delay times of a fuel-air mixture. However, the reduction in ignition delay time was not enough to effectively enable pre-ignition timings of about -20°CA aTDCf, as it could be shown in engine testbed investigations. This phenomenon could also be found by applying numerical models to neat hydrocarbon droplets. [15, 48] Consequently, somewhat more reactive species included in the oil droplet are supposed to accelerate the droplet combustion chemistry.

Simiand [49] could demonstrate that n-heptane-air mixtures can build up low quantities of ketohydroperoxides. This investigation was performed using a motored CFR engine running under conditions close to autoignition but without combustion. Mager [50, 51, 52] could make similar observations, modeling multiple consecutive compression and expansion strokes without gas exchange. Ketohydroperoxides are intermediate species formed during the low-temperature oxidation regime of hydrocarbons and are reported to be very reactive even in small concentrations. Such reactive semi-stable species may result from repetitive heat cycles due to the compression and expansion stroke or incomplete combustion. This theory is supported by the investigation of Marran [53], who observed partially oxidized species entering the combustion chamber originating from small artificially introduced holes (< 2.0 mm). The species were detected using an optical accessible engine setup utilizing a planar laser-induced fluorescence (PLIF) method. Heiß [15] investigated the theory of ketohydroperoxide-induced droplet ignition intensively by using a chemical reactor model. High shares of ketohydroperoxides significantly decrease the ignition delay time, enabling LSPI events at -17 °CA aTDCf. However, the reported crank timing correlated with the observed decomposition temperature of 680 K, at which the investigated species showed noticeable exothermic heat release. Therefore, the practical crank timings depend on the thermodynamic conditions of the engine setup and operation point. Nevertheless, the variation of the compression ratio in engine testbed experiments showed only a minor influence on the LSPI frequency [20].

In order to investigate the sensitivity of the oil droplet ignitability, Palaveev [28] doped the lubricating oil with up to 1 %-vol 2-ethyl-hexyl-nitrate (2-EHN). This substance is known as an ignition improver and is usually used as an additive in diesel fuels [54]. Surprisingly, the LSPI frequency decreased compared to the non-doped setup. However, the engine operation showed an increased number of knocking cycles and intensities and thus illustrating the potential of EHN to enhance chemical kinetics in the air-fuel mixture.

2.2.2. *Particle-induced LSPI hypothesis*

Although the detachment of oil-fuel droplets could be validated numerically and observed experimentally, there are still some uncertainties with respect to the droplet ignitability under engine-relevant conditions. Therefore, an alternative hypothesis regarding a particle-induced LSPI mechanism is discussed in the literature. This hypothesis assumes that oil or oil-fuel mixtures are burned incompletely, forming deposit structures on the cylinder liner and piston top land area. After reaching a sufficient size, these structures are able to flake off the walls. Such particles may survive the gas exchange and achieve a sufficiently high surface temperature to ignite the fuel-air mixture.

Besides the increased fluid mobility and droplet detachment probability of fuel diluted oil inside the piston crevice, it is also known that enhanced fuel wall wetting correlates with deposit formation. Therefore, the investigations correlating enhanced fuel spray / liner interaction with increased LSPI frequency remain valid for the particle-induced ignition hypothesis. Furthermore, Amann [41] investigated the influence of the chemical composition of fuels on LSPI occurrence. To do so, he used four different fuels with similar RON, MON, and evaporation behavior but vastly different chemical compositions. The investigation revealed that the share of aromatics influences the LSPI frequency drastically. By using a fuel blend with ~50 % less aromatic share, no LSPI events could be detected in the used engine configuration. The LSPI enhancing effect of aromatic species is confirmed by the work of Mansfield [55]. Typically, aromatic species such as toluene are reported to show inhibiting effects on autoignition and thus boost RON numbers [56]. However, these species tend to increase soot and carbon-based deposits formation. [57] Although RON / MON fuel specifications describe the autoignition tendency of fuel-air mixtures, the observed correlations are insignificant with respect to the LSPI frequency. Consequently, the introduction of additional fuel-based LSPI ratings suffers from weak correlations. [58, 59, 60, 61, 62] Nevertheless, it is observed that high RON / MON readings reduce the subsequent knock intensity. [39, 41, 55, 57]

Complementary to the fuel-related investigations, the influence of lubricating oil is further studied. Investigations regarding the volatility (defined by the NOAK volatility test [63]) and viscosity of the base stock oils appeared to be insignificant. [64, 65, 66] Furthermore, Morikawa [67] reported that the ignitability of the lubricating oils (defined by the cetane number [68]) showed only minor effects on the LSPI-frequency, indicating that the reactivity of liquid oil droplets is neglectable. Nevertheless, many authors reported that the additive system of a modern engine oil significantly impacts LSPI probability. [39, 46, 69, 70, 71] Leach [39] reported that LSPI events could be entirely avoided by using lubricating oil with low Calcium levels, independently of the aromatic content of the used fuel. Similar findings are reported by Onodera [69] and Hirano [70]. Fletcher [71] did a systematic evaluation of the impact of detergent packages, including single-metal and bi-metal detergent systems as well as anti-wear additives on a boosted engine configuration. He reported that the overall Calcium share in the lubricating oil is a dominating factor with respect to LSPI frequency, independently of the used detergent system (such as Ca-sulfonate, Ca-phenate, or Ca-salicylate). The use of Magnesium-based single-metal configurations (such as Mg-sulfonate) showed no LSPI events under the same engine operating conditions.

Furthermore, an increased share of molybdenum and phosphorus-based anti-wear additives (i.e., ZnDTP) reduced the occurrence of LSPI events. However, it has to be mentioned that the content of anti-wear agents is limited due to the poisoning effects of the three-way catalyst (TWC) system. The work of Liang [72] further confirms the catalytic effect of metallic residues of oil ashes concerning soot oxidation reactions. The author mixed ash generated by commercially available additive packages and soot taken from the exhaust pipe of a Diesel engine. The non-isothermal thermogravimetric analysis

(TGA) revealed that the oxidation rate is enhanced as well as the start of noticeable sample weight loss (defined by the temperature T10 at 10% sample weight reduction). Furthermore, it could be observed that the increased reaction speed results from enhanced surface oxidation of the soot particles. Liang [72] concluded that this change in the oxidation behavior results from the loose ash / soot contact generated by simply mixing and stirring the samples.

The reported catalytic effect suggests that the reactivity of detached deposit structures significantly impacts LSPI frequency. This result correlates with the enhancing effect of lean air-fuel ratios. [29] The oxygen partial pressure level may influence the surface temperature of reactive particles by accelerating exothermal reactions.

In order to get further insights into the possibility of particle-induced pre-ignitions, Okada [29] and Wang [73] extended their engine testbed setup with a particle injection device. Using such a device made it possible to inject a variety of defined particles into the intake manifold. Wang [73] studied the influence of injected activated carbon particles on the PI-characteristic. The investigation revealed that sufficiently hot and big carbon particles were able to initiate an LSPI event. However, particles smaller than 50 µm did not generate irregular combustions in the investigated initial particle temperature range of 573 K ~ 723 K. This result is confirmed by the experiments of Okada [29], who injected soot collected from the exhaust pipe and artificial generated carbon black (20 nm ~ 100 nm). Additionally, he injected extracted deposits out of the combustion chamber. This artificial deposit detachment event could reproduce the "conventional" LSPI behaviors in terms of ignition timings. However, the use of milled coffee beans (< 2 mm) led to a similar result. Besides these combustible substances, none of the non-combustible injected substances could initiate a premature ignition. It should be noted that the initial particle temperatures were at room temperature. Therefore, it can be assumed that inert particles were flushed out of the combustion chamber before achieving a sufficient surface temperature. Gupta [74] investigated the experimental results of Wang [73] numerically, using a simplified 0D model incorporating an Arrhenius-based ignition approach. The results suggest that initial particle temperatures of < 723 K could not trigger an LSPI in the initial cycle. That concludes that even combustible particles may need several consecutive cycles to heat up sufficiently.

3. Research objective

Many putative ignition sources could lead to premature ignitions. Previous investigations and literature data ruled out single-phase root causes under engine-relevant conditions. The utilization of optical accessible testbed configurations revealed flying light-emitting objects indicating a two-phase induced ignition mechanism. Such objects are probably the result of multi-cycle accumulation and transformation processes leading to detachable structures. However, at present knowledge, it is unclear whether these observed objects are oil-fuel droplets or solid particles nor if such objects are able to ignite the surrounding air-fuel mixture. Therefore, the work at hand aims to detailly investigate the entire process chain of hydrocarbon droplet-induced ignitions as well as solid particle-induced ignition mechanisms, leading to the initial LSPI event.

In a first step, the thermodynamic conditions inside the combustion chamber of a highly boosted and LSPI-prone operation point are determined using CFD simulation. Special focus is applied to liquid phase models concerning evaporation behavior, thus dictating mixture inhomogeneities as well as fuel spray / wall interactions. Therefore, multi-component fuel and oil surrogate models incorporating UNIFAC activity coefficients are established using a 0D distillation model and gas chromatography analysis. This level of detail allows for analyzing critical droplet wall interactions leading to oil dilution and promoting droplet detachment and deposit build-up.

In order to account for the inherent stochastic character of LSPI occurrence and thus detachment events, a stochastic object release is developed and implemented in a full engine CFD model to determine the LSPI risk under given thermodynamic engine configurations. The post-processed thermodynamic history of detached objects inside the combustion chamber is recorded and used as boundary conditions in detailed sub-models as input data.

Since the computable resolutions in CFD models incorporating the engine geometry are limited to some extent, the detailed analysis of the physical and chemical processes initiating an ignition are investigated using highly resolved 2D-CFD sub-models. By separating the micro-scale ignition processes from the description of the engine-scale turbulent flow field, it is possible to efficiently explore the sensitivity of thermodynamic parameters as well as the influence of accumulated semi-stable reactive substances on the ignitability of the surrounding gas phase. The results of the detailed models are then used to determine the ignition risk of given objects' histories by introducing an ignition integral approach.

The establishment of a generalized workflow can be transferred to any engine configuration and used to determine the statistical LSPI risk and thus improve engine developments in the near future.

4. Ignition fundamentals

4.1. Oxidation of hydrocarbons

The complete oxidation of hydrocarbons can be expressed by the general equation 4.1.

$$C_xH_y + \left(x + \frac{y}{4}\right) O_2 \leftrightarrow x\, CO_2 + \frac{y}{2}\, H_2O\ (+\Delta H_R) \tag{4.1}$$

The conversion of the fuel molecule to carbon dioxide and water is an exothermic reaction and therefore releases heat, denoted as ΔH_R. This simplified equation is the final result of a complex reaction system involving a large number of elementary reactions and intermediate species. In order to fully understand the temporal evolution of ignition and combustion, one has to look into the reaction kinetics of all substeps. Figure 4.1 illustrates the oxidation pathways in the case of alkanes.

In the following, RH denotes the non-oxidized alkane molecule. Active radicals are highlighted by a dot ($\dot{R}$). Additionally, organic radicals with free valences due to internal hydrogen abstraction are denoted via (R').

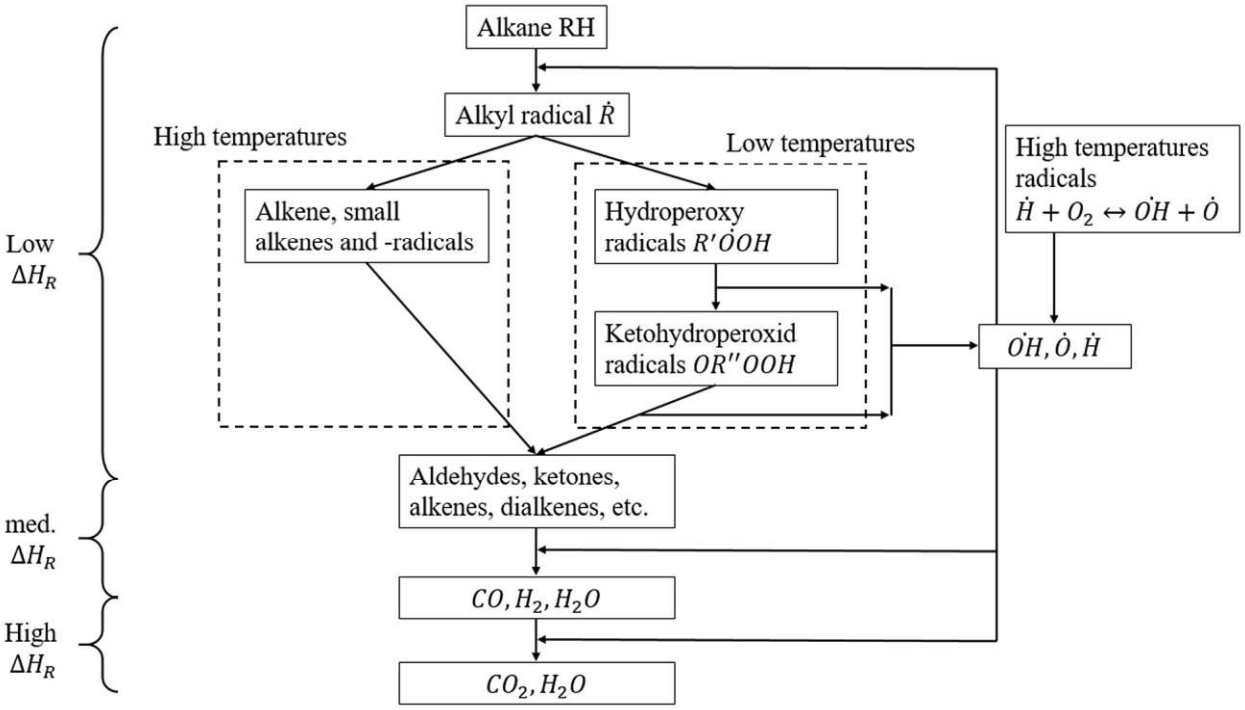

Figure 4.1: Simplified illustration of reaction pathways in the case of alkanes [75].

The initial step is an oxidation of RH using oxygen (equation 4.2).

$$RH + O_2 \leftrightarrow \dot{R} + H\dot{O}_2 \tag{4.2}$$

This chain initiation step is endothermic (~ 160 kJ/mol [76]) and therefore needs a sufficiently high gas temperature to initiate fuel oxidations. This initial step creates the first radicals in the species pool. Since this reaction is comparatively slow, it is responsible for the first rather long induction period. [8] With the ongoing oxidation process, highly reactive radicals (i.e., $\dot{O}$, $\dot{H}$, $H\dot{O}_2, O\dot{H}$) are already present and preferably used for the initial hydrogen abstraction reaction increasing alkane consumption, shown in equation 4.3 in the case of a hydroxy-radical.

$$RH + O\dot{H} \leftrightarrow \dot{R} + H_2O \tag{4.3}$$

In the next step, the alkyl radical is further oxidized with molecular oxygen, shown in equation 4.4.

$$\dot{R} + O_2 \leftrightarrow R\dot{O}_2 \tag{4.4}$$

The activation energy of the forward reaction (product side) is very low, whereas the reverse reaction shows a relatively high value of ~120 – 150 kJ/mol. [75, 76] This leads to a highly temperature-sensitive chemical equilibrium preferring the formation of alkyl-peroxy radicals at low-temperature levels. Above 900 K, the chemical equilibrium shifts towards the dissociation reaction. As a result, it slows down the further oxidation of the alkyl radicals via chain-branching reactions, even at elevated temperature levels. This effect is also known as the negative temperature coefficient (NTC) effect, outlined in Figure 4.2. Due to the temperature sensitivity of this reaction, the subsequent oxidation steps can be distinguished into “low-temperature” and “high-temperature” chemistry pathways.

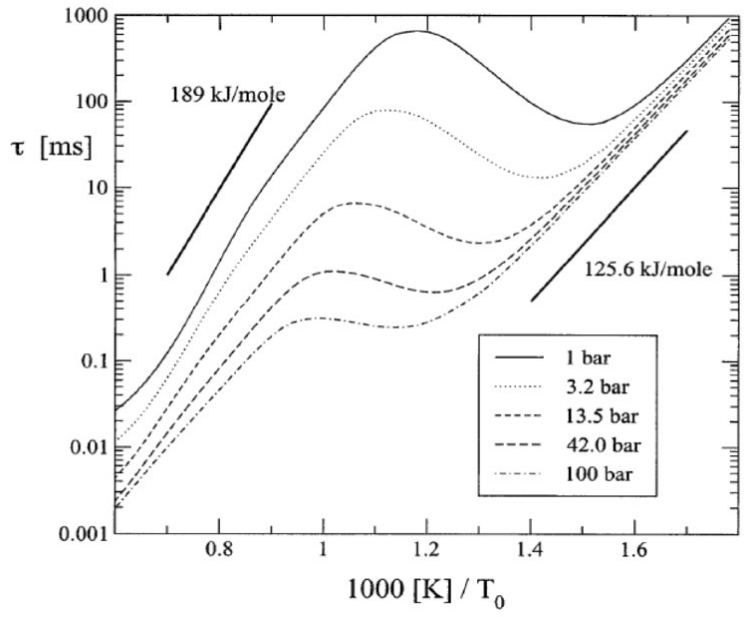

Figure 4.2: Effect of a negative temperature coefficient (NTC) on the ignition delay exemplarily shown for stoichiometric n-heptane mixtures [77].

4.1.1. Low-temperature chemistry

This pathway is dominant at temperature levels below 900 K. In this case, the forward reaction of equation 4.4 is governing. The peroxy-radical $R\dot{O}_2$ undergoes an isomerization reaction, where a hydrogen atom is abstracted from the alkylic component and is added to the peroxy group (equation 4.5). The further oxidation with molecular oxygen and subsequent isomerization results in a build-up of ketohydroperoxids ($OR''OOH$) and additional highly reactive $\dot{O}H$ radicals (equations 4.6 – 4.7).

$$R\dot{O}_2 \leftrightarrow R'\dot{O}OH \tag{4.5}$$

$$R'\dot{O}OH + O_2 \leftrightarrow OOR'\dot{O}OH \tag{4.6}$$

$$OOR'\dot{O}OH \leftrightarrow OR''OOH + \dot{O}H \tag{4.7}$$

The production of $\dot{O}H$ is then feedbacked to equation 4.3 to accelerate the initial chain initiation step of reaction 4.2.

The production rate of alkylhydroperoxy radicals ($R'\dot{O}OH$) finally resulting in ketohydroperoxids increases with the initial fuel molecule size RH, whereas the production rate of long-chained linear alkanes is fastest compared to complex branch-chained or isomerized configurations. This circumstance is crucial regarding the autoignition sensitivity of hydrocarbons (lubricant oil and fuel) used in internal combustion engines. [78, 79]

Up to this point, the described reactions only served the purpose of chain propagation. Therefore, the amount of radicals generated is comparatively low, and no significant heat release can be observed. The decomposition of the ketohydroperoxid introduces the first chain branching reaction (equation 4.8).

$$OR''OOH \leftrightarrow O\dot{R}''O + \dot{O}H \tag{4.8}$$

The activation energy for the decomposition of ketohydroperoxid is reasonably high (~180 kJ/mol [80, 81]). Therefore, ketohydroperoxides can be considered as semi-stable intermediate species acting as a "bottleneck" in the low-temperature hydrocarbon ignition and oxidation process. Consequently, $OR''OOH$ species accumulate during the consumption of the fuel molecule RH via $\dot{O}H$ radicals. With the increasing concentration of ketohydroperoxids, the decomposition reaction speed slowly enhances and acts self-amplifying due to its heat release. At this point, a noticeable heat release accompanied by detectable light emissions can be observed. This phenomenon is also known as "cool flame". As a result, the temperature rises to ~900 K reducing the production of $R\dot{O}_2$ of equation 4.4. This compromises the supply of ketohydroperoxide species and reducing the heat released via the chain-branching reaction 4.8. Instead, the formation of alkenes and hydroperoxyl radicals is promoted. The $H\dot{O}_2$ radicals recombine to hydrogen peroxide, which is relatively stable at temperatures below 1000 K. As the temperature further raises and surpasses the mentioned threshold, the accumulated H_2O_2 decompose and releases a high concentration of highly reactive hydroxy-radicals (equation 4.9). This leads to a second significant heat release and raises the temperature well above 1200 K. At this point, the low-temperature oxidation mechanism transitions into high-temperature oxidation chemistry. [75]

$$H_2O_2 \leftrightarrow \dot{O}H + \dot{O}H + M \tag{4.9}$$

The two stages of ignition are visible looking into an autoignition experiment performed in a rapid compression machine (RCM) using n-pentane-air mixture, shown in Figure 4.3.

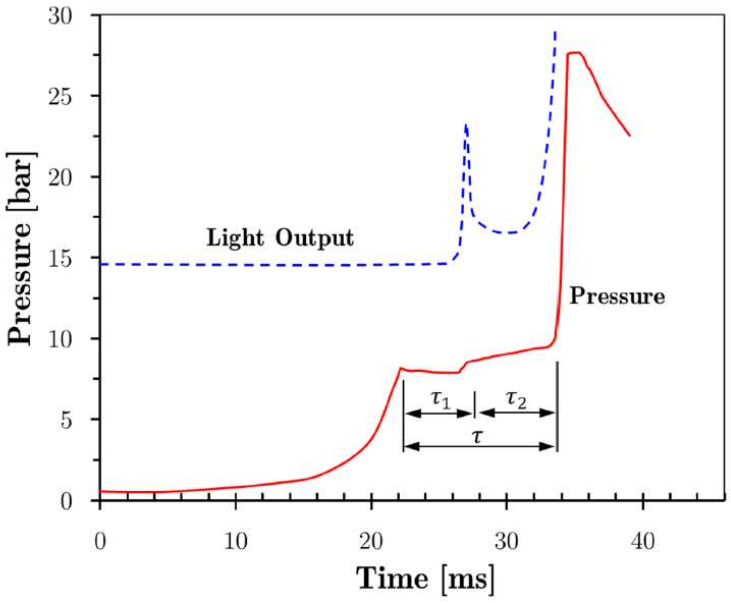

Figure 4.3: Recorded pressure trace of an RCM ignition investigation using an n-pentane-air mixture [82].

After applying high pressure and temperature via compression, the first induction period τ_1 can be observed. During this time, the accumulation of ketohydroperoxid species takes place. At the end of the first induction period, the self-amplifying decomposition leads to the observable "cool flame" effect. Here, a step increase in temperature and pressure can be observed, enabling the build-up of peroxides which finally decompose at the end of the second induction time τ_2.

4.1.2. High-temperature chemistry

This oxidation regime is dominant at temperature levels above 1200 K. In this case, the formed alkyl-radicals via reaction 4.4 are unstable, especially for long-chained alkanes. They decompose into smaller alkenes and alkyl radicals up to a size of $C\dot{H}_3$ and $C_2\dot{H}_5$. [75, 83] Therefore, the high-temperature oxidation mechanism of higher-order hydrocarbons can be simplified to a methane and ethane oxidation scheme, shown in Figure 4.4. [84]

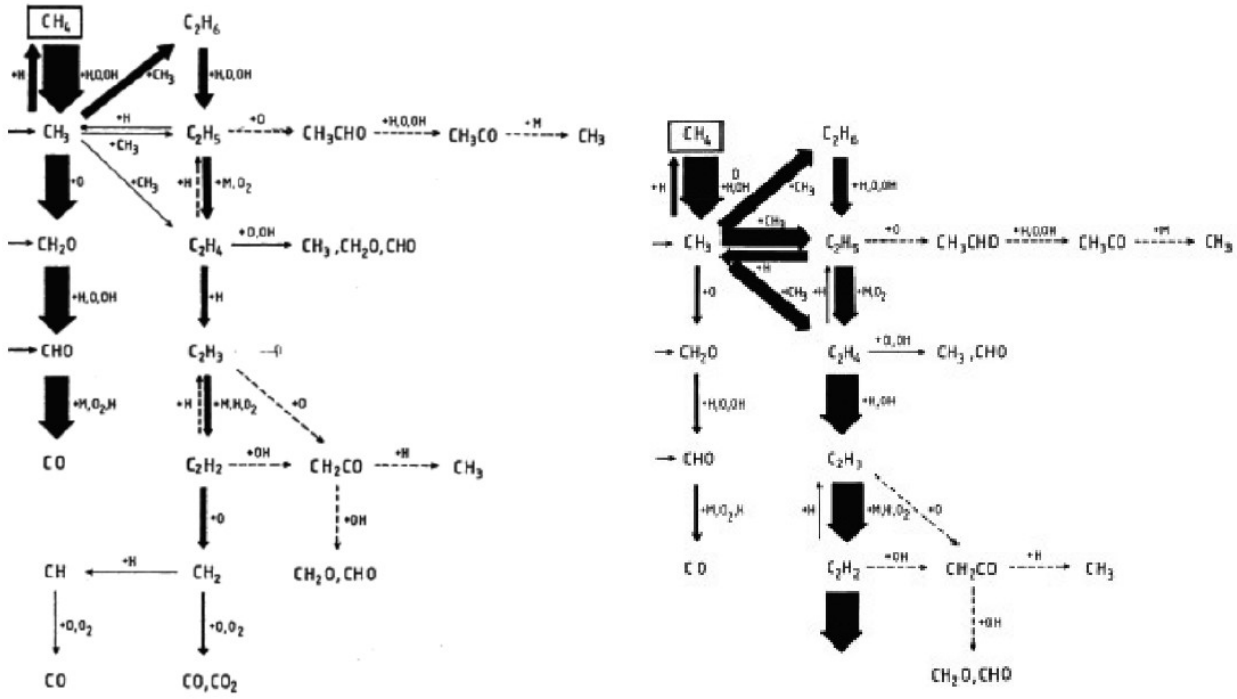

Figure 4.4: Oxidation regime of methane and ethane. [84] (**a**) stoichiometric conditions, (**b**) fuel-rich conditions.

In this case, the reaction mechanism is supplied after the first hydrogen abstraction reaction. In stoichiometric combustions the $C\dot{H}_3$ are directly oxidized via highly reactive radicals (i.e., $\dot{O}$, $\dot{H}$, $O\dot{H}$) ending up in carbon monoxide. In contrast, in fuel-rich conditions, the recombination of larger molecules is preferred before being oxidized in a similar sequence of hydrogen abstraction and oxygen addition. The final oxidation step leads to carbon dioxide releasing ~45 % of the overall heat contained in the initial hydrocarbon fuel. [75] Therefore, the pressure signals inside a combustion chamber increase only slightly during the low-temperature oxidation stage.

4.2. Induced ignition vs. autoignition phenomena

Ignition describes the onset of a combustion process and can be subdivided into autoignition and induced ignitions.

As the name suggests, induced ignitions rely on external heat sources to accelerate chemical kinetics leading to thermal runaway (also known as a thermal explosion). In typical applications (i.e., sparks, flames, and hot surfaces), the supplied temperature by the heat source is well above 1200 K. As a result, induced ignitions undergo the described high-temperature chemistry pathway (section 4.1.2), not showing a distinctive ignition delay time. According to Semenov [85], the ignition process is defined as a thermal explosion when the chemical heat release surpasses the heat lost due to heat conduction, diffusion, and radiation leading to an instantaneous increase in temperature without an apparent delay time.

An induced ignition is considered successful if the hot reaction zone leads to subsequent flame propagation. In order to generate a self-sustaining propagating flame, the kernel should have grown to

a critical size by the time the external heat source extinguishes and the origin has decreased to flame temperature. Considering the "flame ball" concept introduced by Zeldovich [57, 86, 87], this critical size is defined as a critical spherical radius R_c and can be determined by equation 4.10. Spherical flames smaller than R_c are unable to overcome the heat transferred to the environment and consequently extinguish.

$$\frac{R_c}{THK_{lam}} = e^{0.5*\beta*(1-\frac{1}{Le})} \tag{4.10}$$

$$Le = \frac{Sc}{Pr} = \frac{\frac{\nu}{D_{AB}}}{\frac{\nu}{a}} = \frac{a}{D_{AB}}$$

According to the investigations of Zeldovich, the critical radius depends on the laminar flame thickness THK_{lam} and is further corrected by the Zeldovich number β $(= E * \frac{(T_b - T_u)}{RT_b^2})$, and the Lewis number Le. As a result, the laminar flame thickness dictates the minimum self-sustaining flame kernel size. Assuming $Sc = 1$, the laminar flame thickness is given by equation 4.11.

$$THK_{lam} = \frac{D_{AB}}{s_L} \rightarrow (Sc = 1) \rightarrow THK_{lam} = \frac{\mu}{\rho * s_L} \tag{4.11}$$

This analysis shows that the laminar flame thickness is defined by the laminar flame speed s_L and the gas density ρ. Whereas the laminar flame speed depends on the fuel itself, a high overall gas pressure promotes the likelihood of successful induced ignitions.

In contrast to induced ignitions, autoignition occurs without the support of an external heat source. Instead, the thermodynamic condition of the fuel-air mixture is determinating the ignitability. In the case of internal combustion engines, these conditions are mainly determined by the effective compression ratio of the engine setup as well as the initial condition of the cylinder charge at IVC. Considering SI engines, the temperature and pressure level during the compression phase typically fall below 800 K and 60 bar. As a result, observable autoignition (i.e., knocking combustion) is dominated by the low-temperature oxidation pathway, described in section 4.1.1. [8, 75]

5. Experimental characterization of the LSPI phenomena

The experimental investigations aim to characterize the pre-ignition phenomenon. The utilization of an optically accessible engine setup enables the identification of LSPI-prone areas or distinctive phenomena. Additionally, the use of light-induced fluorescence (LIF) techniques by adding tracer substances to the engine operating media (lubricating oil and fuel) enables the differentiation of solid-like particles and liquid oil droplets. Furthermore, the gained measurement data are essential for establishing accurate numerical models predicting the thermodynamic conditions inside the combustion chamber and potential ignition phenomena.

Furthermore, it has to be highlighted that the experimental investigations were performed in cooperation with the Institute of Internal Combustion Engines (IFKM) at the Karlsruhe Institute of Technology. The testbed setup, validation, and the achieved experimental results are published in [18, 19, 88, 89].

5.1. Engine testbed setup

In order to achieve a comprehensive understanding of the phenomenology of LSPI combustions, a turbocharged SI engines with central gasoline direct injection is mounted on a research engine testbed. For the purpose of increasing the resilience against high in-cylinder pressure peaks resulting from continuous operation under LSPI-prone conditions, the engine is equipped with reinforced connecting rods and cast-in piston ring carriers. The specifications are listed in Table 5.1.

Table 5.1: Engine specifications [88, 89].

Property	**Specification**
Type	Inline 3, 12 valves
Cylinder displacement	333 cm³
Bore x Stroke	71.9 x 82 mm
Compression ratio	10.5
Valve train	DOHC
Air charging	Single scroll turbocharger, Intercooler
Fuel system	Direct injection, 6-hole injector, central position
Firing Order	1-2-3

The use of a prototyping engine control unit offers complete control over operational parameters and furthermore the deactivation of coded protective measures (i.e., knock control). Thermodynamic monitoring was achieved via three water-cooled piezoelectric pressure sensors of type Kistler 6041B in the cylinder head, a water-cooled piezoelectric pressure sensor of type Kistler 4049A10 in the exhaust manifold, and a piezoelectric pressure sensor of type Kistler 4075A10 in the intake airbox. In pursuance of optical pre-ignition characterization, the engine is equipped with three minimally invasive optical accesses using sapphire windows in the first cylinder. Two water-cooled high-power LED (blue) lighting systems (Ø 4 and 8 mm) with additional light spectrum adaption using a short-pass filter provide combustion chamber illumination as well as fluorescence excitation of traced operating media (lubricating oil and fuel). The air-cooled observation access holds a Ø 8 mm endoscope which guides

the light to the decoupled high-speed camera (Phantom 1612 with 12-bit CMOS Bayer-sensor). The achievable image rate for all measurements was 4.8 kHz which correlates to an angular resolution of ~2 °CA at 1600 rpm. A long-pass filtered observation enables the separation of excitation light and fluorescence light. Figure 5.1 shows an overview of the used experimental testbed setup.

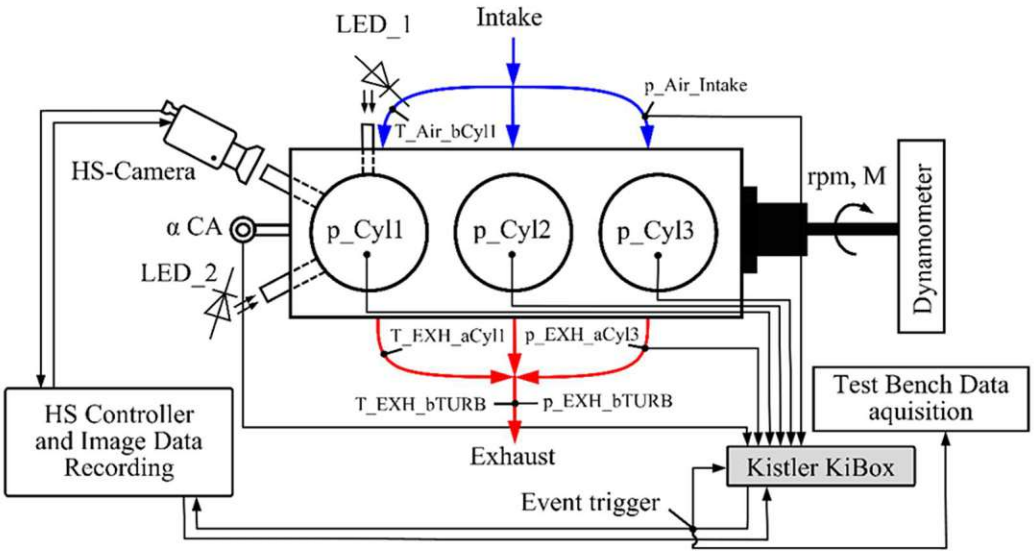

Figure 5.1: Experimental testbed setup [88, 89].

The detection of an LSPI cycle is performed by using a ±4 sigma deviation from the average pressure signal. Statistical representations of LSPI frequencies are evaluated by running 20,000 to 50,000 engine cycles. The used cycle count was chosen to mediate statistical accuracy and engine testbed lifetime. Optical results are limited to the first 10,000 cycles due to continuous window fouling.

For the investigation at hand, a high load steady-state engine operation at a speed of 1600 rpm and 200 Nm (= 25.2 bar BMEP) engine torque is used. In order to minimize the influence of residual gases and achieve the necessary boost pressure, the valve timing was set to a valve overlap of 53 °CA resulting in a scavenging operation. The operational parameters were selected based on the knowledge gained in the literature to increase the probability of LSPI events enabling the optical setup to observe pre-ignitions within the first 10,000 cycles. Therefore, a slightly lean global fuel-air ratio, as well as a reduced cooling water temperature, were used. Table 5.2 shows the complete set of parameters considering the investigated load point.

Considering the operating media of the engine setup, the engine is running on Coryton Advanced Fuels "High LSPI" fuel. This synthetic blend offers the advantage of being consistent in composition throughout all performed experiments. The fuel fulfills DIN EN 228 standards [90], although it exploits the upper threshold of the distillation end temperature, indicating an enhanced share of low-volatile species. For lubrication purposes, the engine is running on commercially available Fuchs Titan Supersyn F Eco DT 5W-30 engine oil. Concerning the used additive package, the exact formulation was not available. However, the manufacturer supplied an elemental-based analysis, summarized in Table 5.3.

For the characterization of fuel and oil droplet trajectories inside the combustion chamber, the operating media is mixed with a sufficient amount of fluorescence tracer (Lumilux CD345). Since the spectra of the fluorescence response of oil and fuel overlap, they can only be examined separately. The use of a 525 nm long-pass filter (LP-F) on the recording camera enables an unambiguous separation of excitation and fluorescence light. A detailed review and validation of the fluorescence tracer in combination with the specific operating media is shown in [89].

Table 5.2: Load point specifications [88, 89].

Property	Specification
Engine Speed	1600 rpm
Engine torque / BMEP	200 Nm / 25.2 bar
Spark timing	4 °CA aTDCf
Charge air temperature (Airbox)	313 K
Boost pressure	2.25 bar (abs)
Air-fuel ratio - $\boldsymbol{\lambda_{Exhaust}}$	1.08
Temperature cooling water	338 K
Start of Injection (SOI)	250 °bTDCf
Injection pressure (rail)	100 bar

Table 5.3: Elemental-based additive package characterization [88, 89].

Element	Mass fraction [mg/kg]
Calcium (Ca)	2842
Magnesium (Mg)	14
Boron (B)	84
Zinc (Zn)	1072
Phosphorus (P)	907
Barium (Ba)	0
Molybdenum (Mo)	0
Sulfur (S)	2175

5.2. Optically derived phenomenology of LSPI

The usage of optical imaging reveals two different consistent patterns with respect to LSPI initiation. These differ in the history of combustion cycles resulting in a mega-knock event. In the following, these patterns are referred to as “object-driven” LSPI and “deposit-driven” LSPI events.

Considering the “object-driven” LSPI mechanism, Figure 5.2 shows an overview of the observed pattern. In the engine cycles prior to the LSPI event, the regular combustions are accompanied by the presence of pool fires located on the piston top land as well as the piston crevice area (first circle in Figure 5.2). After several engine cycles, the LSPI event is initiated by a flying, glowing object, typically becoming visible during the compression stroke (second circle in Figure 5.2). Finally, a propagating flame is initiated from the glowing object leading to mega-knock combustion due to the undesired early heat release (third circle in Figure 5.2). The observed ignition locations inside the combustion chamber followed no clear spatial distribution pattern. The cycle after the mega-knock event shows a large number of glowing objects after the combustion initiation by the spark plug, indicating a massive detachment of objects due to the pronounced pressure oscillations during the mega-knock combustion.

After the initial LSPI event, a sequence of non-repetitive conventional combustion and follow-up LSPI events can be observed. However, the number of observable glowing objects is reduced after every gas exchange. Consequently, the combustion pattern returns to a prior pre-ignition state, ending the aforementioned sequence.

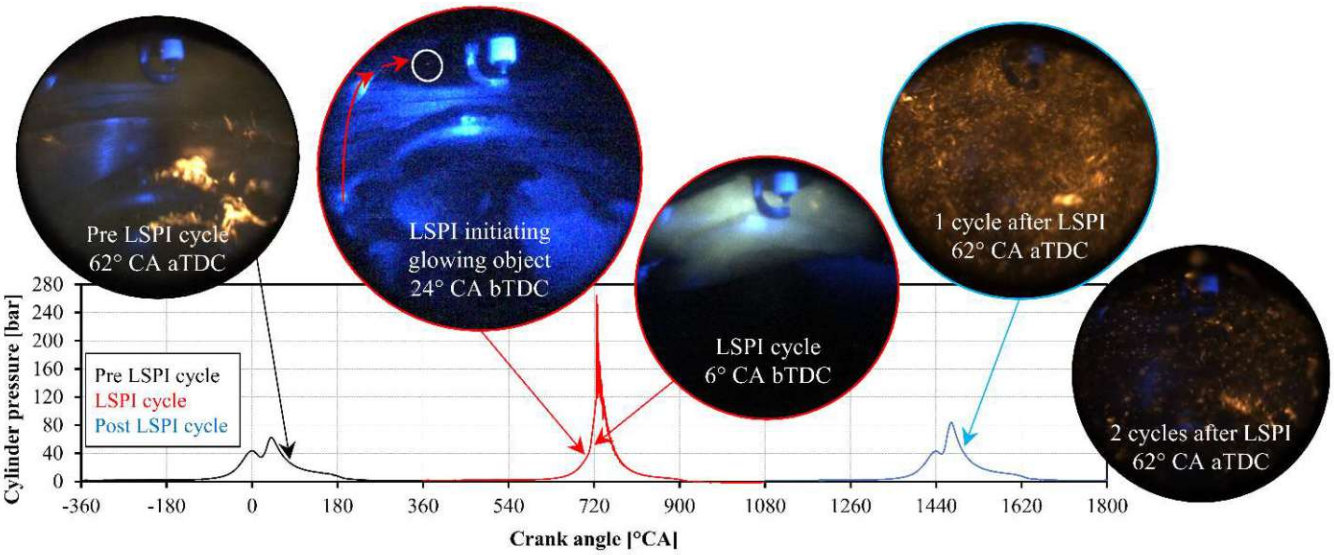

Figure 5.2: Observed phenomenology of "object driven" LSPIs [88].

In the case of the "deposit-driven" LSPI mechanism, the regular combustion cycles transition into "mild" premature ignition combustion cycles, shown in Figure 5.3. These "mild" cycles are continuously initiated by a glowing spot on a specific location on the piston crown near the crevice. The visual inspection of the engine revealed that at this particular location, a significant deposit build-up could be observed. Furthermore, an accumulation of deposit structures on the nearby cylinder liner area could be observed. A further experimental investigation of the fuel spray / wall interaction using a fuel-doped dye (LIF) confirmed the fuel impingement and possible accumulation in these areas, shown in Figure 5.4. Nevertheless, such initiated "mild" LSPI cycles lead to a very late initiation of a propagating flame front, thus showing an insignificant effect on the pressure signal considering the statistical variation of conventional engine cycles (< ±4 sigma deviation). Therefore, such "mild" events could not be detected via in-cylinder pressure signal-triggered monitoring. The continuous sequence of "mild" cycles ends with the occurrence of mega-knock combustion. Typically, the mega-knock combustion is triggered by an additional ignition source inside the combustion chamber. The initial mega-knock event triggers the characteristic sequence of follow-up LSPIs and finally removes the build-up deposits on the piston crown.

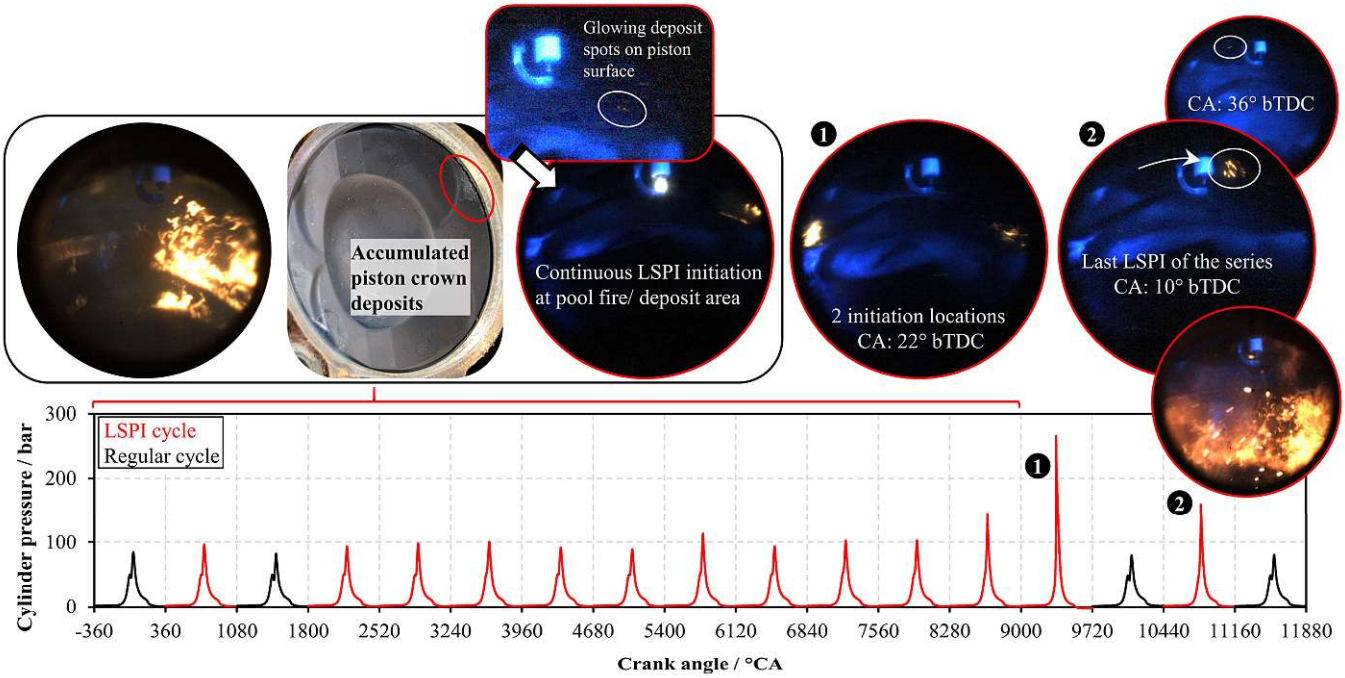

Figure 5.3: Observed phenomenology of "deposit-driven" LSPIs [89].

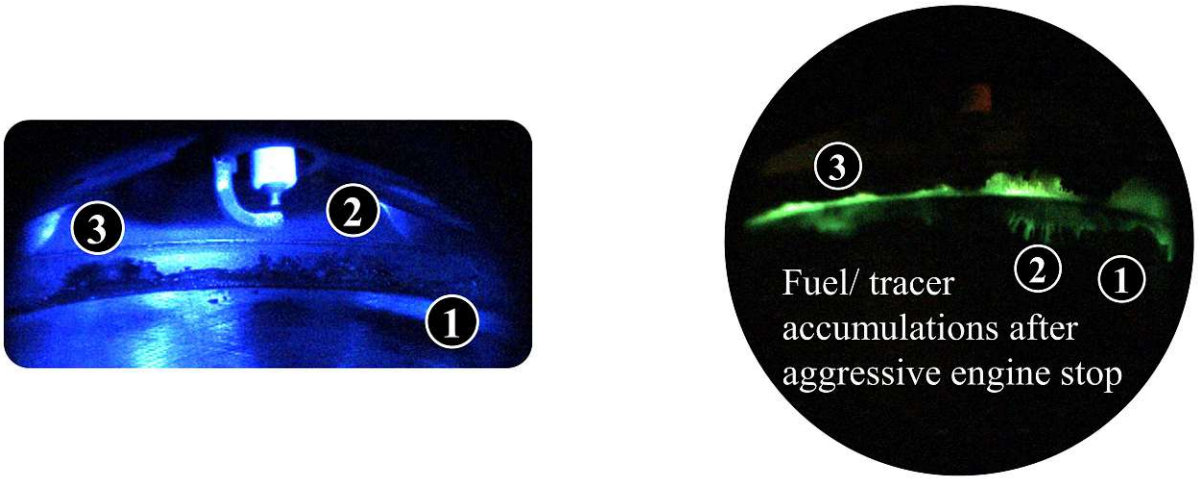

Figure 5.4: Correlation of fuel spray liner wetting and deposit build-up [89].

There was no LSPI event detectable or optically observable that was not initiated by a history of light-emitting objects or deposits. This highlights the substantial importance of a second phase inducing LSPI events. Therefore, the observed objects were further investigated and characterized.

5.3. Characterization of LSPI initiating objects

In order to identify whether the observed objects are burning liquid oil droplets or hot solid particles, experiments are performed using fluorescence dye-doped lubrication oil. The wavelength-filtered observations revealed that no liquid oil droplets or fluorescence histories could be recorded prior to an initial LSPI event. However, a mist of detached oil droplets could be detected on rare occasions after very strong knocking accompanied by severe in-cylinder pressures and pressure oscillations caused by an "object-driven" LSPI. This possibility was also hypothesized in [17, 25] and thus, confirmed by these experiments.

Considering the LIF system limitations with respect to excitation light intensity and image resolution, very small detached oil droplets smaller than 100 µm in diameter may not be detectable. Consequently, it cannot be excluded that very small flying oil droplets are present inside the combustion chamber prior to the initial LSPI event. Nevertheless, the initiation of LSPI events due to not detectable oil droplets would imply pre-ignition events without observable object history. However, all detected and recorded LSPI events showed a glowing object or deposit history, indicating that oil droplet-induced LSPI events are very improbable for this engine configuration and load point. Further analysis of non-filtered experimental results showed the occasion of glowing objects bouncing off the inlet valve or the spark plug electrode while following the tumble flow motion before initiating an "object driven" LSPI event, shown in Figure 5.5. Thereby, no fluid-related decomposition (i.e., breakup, thermal breakup, wall film formation, splash, etc.) of the object was observed wherefrom a solid character can be assumed.

Additionally, Figure 5.5 shows that the LSPI initiating particle starts to glow during the compression stroke. The color and spectral response curve of the used Phantom camera is similar to the human eye allowing for a conservative temperature estimation using the Draper point. [91] The Draper point represents the temperature threshold at which a hot object becomes visible to the human eye in a dark environment (dark red). Assuming that the observed particle is a black body radiator, it becomes visible at a temperature above 798 K. Considering an isentropic compression under the boundary conditions of the used engine geometry and load point, the gas phase temperature falls below 800 K at TDC. Consequently, a particle cannot be heated above the Draper-point during the compression stroke solely by heat transfer. This indicates an exothermal reactivity of the particle substrate.

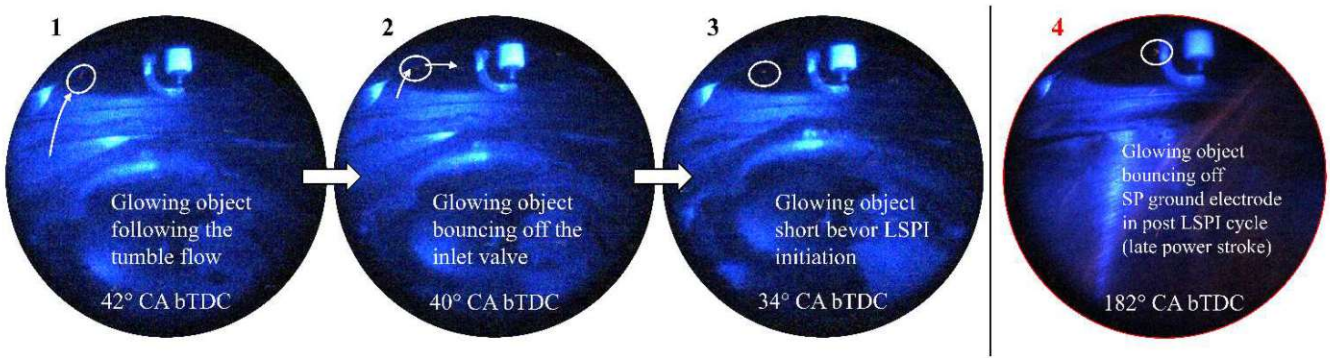

Figure 5.5: The solid character of glowing objects [88].

The origin of the detachment of LSPI-initiating objects could not be determined in most cases due to the limited field of view inside the combustion chamber. In some instances, the ignition initiating objects

fly out of the piston crevice area near TDC, indicating an object release, shown in Figure 5.6. However, particle history revealed that already existing flying objects dive into the crevice beforehand in rare cases. Furthermore, light-emitting objects are observed during the intake stroke as well as in the early compression stroke, indicating a multi-cycle mechanism. This assumption matches the fact that no clear spatial distribution of ignition locations can be determined. Since the turbulent in-cylinder flow field aims to generate a homogeneous air-fuel mixture, it would have the same effect on "object-driven" ignition distribution.

Concerning the size of critical objects, a rough estimation can be made by comparing the object size with the known thickness of the spark plug ground electrode. In general, all visible objects are similar in size ranging in the magnitude of tenths of a millimeter. It can be observed that all LSPI-inducing glowing objects are bigger than ~0.2 mm in diameter. Glowing objects smaller than this threshold did not initiate a propagating flame front during the entire compression stroke, indicating a crucial minimum object diameter.

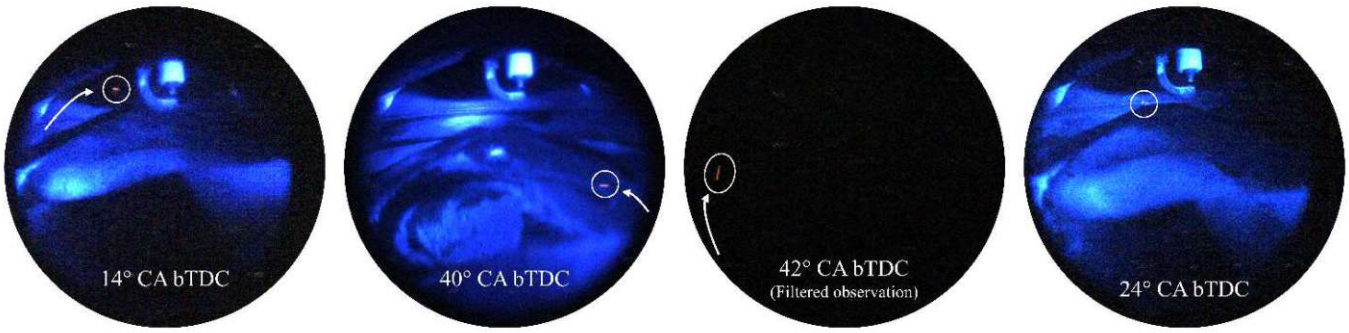

Figure 5.6: LSPI initiation by flying glowing objects [88].

6. Determination of charge inhomogeneities and wall wetting using CFD

In highly boosted SI-engines, the mixture preparation process under full load conditions is a challenging task. High specific engine loads demand for high cylinder charge densities resulting in an elevated fuel mass demand to maintain close to stoichiometric operations. As a result, long fuel injection durations are necessary, reducing the available time for evaporation and mixing. Furthermore, geometric limitations may lead to fuel spray / wall impingement and wetting enhancing mixture inhomogeneities. Gradients in air-fuel ratio and especially gas temperature influence the local chemical kinetic speed and thus the sensitivity to auto-ignitions. [92] In order to determine the spatial distribution of cylinder charge properties, a 3D-CFD engine model is established. The model focuses especially on the detailed description of the mixture formation process and the identification of liquid film-prone areas promoting the generation of carbon-based deposits.

6.1. Description of the in-cylinder flow field

The numerical grid representing one cylinder of the investigated engine setup was generated using the trimmed meshing approach of the commercial CFD code SIEMENS StarCD/es-ice version 4.30.029. The simulation domain includes the combustion chamber, the spark plug, the piston crevice volume, and the intake- and exhaust ports up to the position of the pressure sensors in the testbed configuration. The changes in the shape of the combustion chamber contour due to manufactured optical accesses were insignificant and thus neglected in the CFD model. In order to enhance numerical stability, the piston crevice volume was designed as a structured ring-shaped grid avoiding excessive deformation of possibly fuel-wetted walls during mesh motion. This static mesh segment was designed in AVL FIRE version 2017d and exported to the StarCD/es-ice engine model, where it was coupled to the moving piston and liner via an interpolation interface.

The mesh base size is set to 0.5 mm, ensuring an accurate prediction of droplet trajectories and evaporation. Within a radial distance of 5 mm of the injector tip, the mesh is additionally refined to 0.25 mm to account for high velocity gradients during the injection process. The same approach is made concerning the spark plug. In order to capture the turbulent and thermal boundary layer, a 0.15 mm prism layer was introduced along the in-cylinder walls. The spatial discretization is selected based on the spray and evaporation investigations shown in the upcoming sections. The high resolution of the engine domain led to an overall model size of ~5×10^6 hexahedral cells at BDC. Figure 6.1 shows a detailed view of the cell spacing inside the combustion chamber and the piston crevice volume.

The turbulent flow field is calculated using a RANS approach combined with a k-ε RNG turbulence model to capture the conditions of a mean engine cycle.

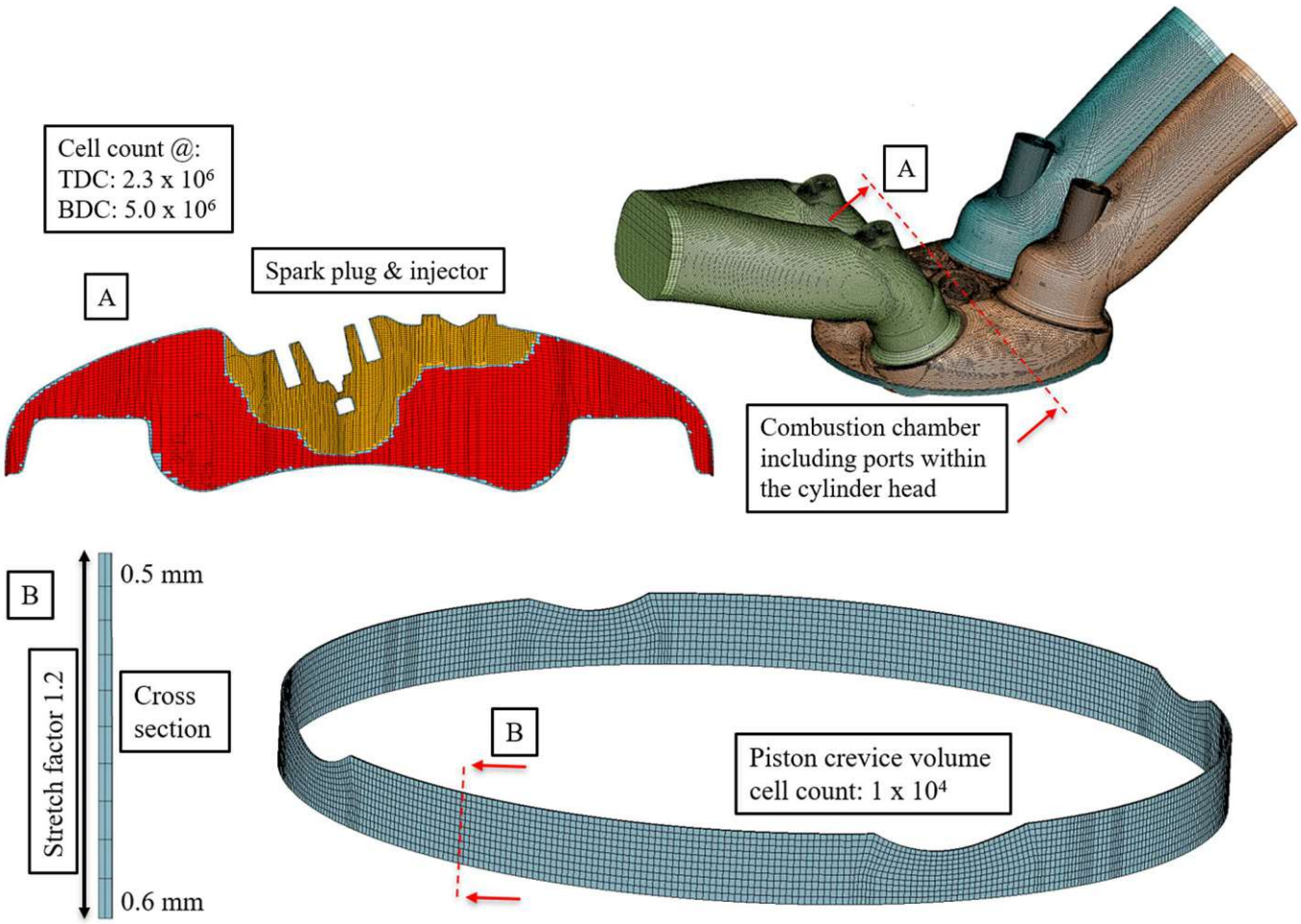

Figure 6.1: Overview of the spatial cell distribution used in the CFD engine model.

6.2. Modeling of the liquid phase

The liquid phase in engine CFD simulations is expected to occur as small droplets introduced by the high-pressure fuel injection or as thin liquid films resulting from droplet impingement. Therefore, the use of simplified modeling approaches is acceptable. [93] The finely dispersed injected droplets are represented using the well-known DDM (Discrete Droplet Model) statistical approach utilizing Lagrangian parcels. The prediction of wall film formation due to droplet impingements is implemented according to the regimes distinguished by Bai and Gosman [94, 95]. The liquid phase is modeled without actual volume representation in the simulation domain, significantly reducing the grid resolution requirements. Consequently, the particles and films interact with their environment only by model-based source terms (energy-, mass-, momentum balance). The thermodynamic properties of the liquid phase are represented by mean values (0D-approach). This assumption is valid if the occurring biot-numbers are comparatively small.

The governing equations are summarized in Table 6.1.

Table 6.1: Governing equations for droplet and film models.

	Droplet (Lagrange particle)	Film	Equation ref.
Mass	$\frac{dm_{d,i}}{dt} = -\varepsilon_i * \frac{M_i}{\sum_{j=1}^{N} \varepsilon_j M_j} * A_{s,d} * K_{g,i} * p_g * ln\left(\frac{\varepsilon_i * p_g - p_{vap,i,\infty}}{\varepsilon_i * p_g - x_{i,l} * p_{vap,i}^s}\right)$	$\frac{\partial \rho_{LF}}{\partial t} + \nabla * (\rho_{LF} \vec{u}_{LF}) = \frac{\dot{m}_{src}}{THK_{LF}}$	(6.1)
Energy	$m_d * c_{p,d} * \frac{dT_d}{dt} = \frac{dQ_s}{dt} + \Delta h_v * \frac{dm_d}{dt}$	$\frac{\partial}{\partial t}(\rho_{LF} h_{LF}) + \nabla * (\rho_{LF} \vec{u}_{LF} h_{LF}) = \nabla * (k_{LF} \nabla T_{LF}) + \frac{\dot{Q}_{LF}}{THK_{LF}}$	(6.2)
Momentum	$m_d \frac{d\vec{u}_d}{dt} = m_d \vec{g} + \frac{1}{2} c_w \rho_g A_{cross,d} \lvert \vec{u}_g - \vec{u}_d \rvert (\vec{u}_g - \vec{u}_d) - V_d \nabla p_g - \frac{1}{2} \rho_g V_d \frac{d(\vec{u}_d - \vec{u}_g)}{dt}$	$\frac{\partial}{\partial t}(\rho_{LF} \vec{u}_{LF}) + \nabla * (\rho_{LF} \vec{u}_{LF} \vec{u}_{LF}) = -\nabla p_{LF} \vec{g} + \nabla * \tau_{LF} + \vec{S}_{src} \delta(\xi - THK_{LF})$	(6.3)

6.2.1. *Validation of the evaporation model*

The used evaporation model is validated against experiments performed by Chauveau [96] and Nomura [97]. Both studies investigated the evaporation rate of a single wire-supported n-heptane droplet under defined ambient conditions. Figure 6.2 shows the droplet supporting wire system used in the experiments.

(**a**) (**b**)

Figure 6.2: Droplet suspending techniques (reprinted form [96]). (**a**) Nomura [97], (**b**) Chauveau [96].

The classical single-fiber setup of Nomura [97] used a wire diameter of 150 µm to support the n-heptane droplet safely. In contrast, the cross-fiber arrangement allows for even thinner fibers of 14 µm, minimizing the influence of heat transfer from the droplet suspending system.

In order to compare the measurement data with the numerical simulation, a single n-heptane droplet is initialized as a Lagrangian particle in the middle of a box-shaped grid. The thermodynamic properties of n-heptane are implemented according to VDI Heat Atlas [98]. The influence of the heat transfer through heat conductivity of the suspending wires is neglected in the simulations. The hexahedral box base size is set to 32 mm to minimize the influence of the static pressure environment boundary conditions. In order to estimate the impact of the mesh resolution, the box is discretized using 0.5 mm,

0.8 mm, 1.0 mm, or 2.0 mm cells. The temporal discretization in all simulations is set to 10 µs. The ambient gas-phase conditions are initialized according to the measurement setup.

The ambient conditions used in the simulations are 1 bar pressure (atmospheric) and a gas temperature ranging from 473 K to 748 K. Additionally, these boundary conditions are used to perform a grid sensitivity study. Figure 6.3 shows the achieved results at 623 K.

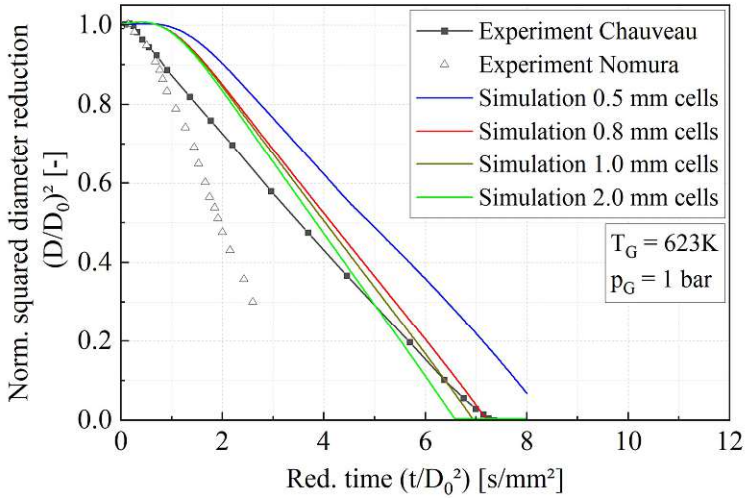

Figure 6.3: Temporal evolution of a 500 µm n-heptane droplet at 1 bar and 623 K on varying grid resolutions.

Overall, this simulation approach can achieve a good agreement with measurement data. However, coarser grid resolutions show to enhance the predicted evaporation rate after the initial heat-up process (gradient deviation). With increasing cell size, the mass fraction gradient of n-heptane in the vicinity of the droplet is underestimated. This lowers the partial pressure of gaseous n-heptane and thus increases the evaporation mass flux by increasing the pressure difference between the saturation pressure and the apparent vapor pressure of n-heptane in equation 6.1. On the other hand, the smallest investigated cell size leads to numerical artifacts by violating the DDM model assumptions. Consequently, the highest numerical accuracy can be achieved by choosing a grid resolution near the lower limit of the DDM model stability. In [93], the lower limit for stability is defined by a theoretical volume fraction (VF) threshold of 0.4. VF represents the relation of the modeled droplet volume to the volume of the numerical cell. This validation study can confirm this threshold. Consequently, a 0.5 mm cell base size discretization is adequate for simulations expecting droplets smaller than 500 µm.

Besides the influence of the cell size on the evaporation rate, an overpredicted diameter increase during the initial heat-up process can be observed. This deviation may result from the assumption of a droplet with an average thermodynamic state (infinite conductivity). In order to clarify this assumption, the evaporation model is extracted to a 0D simulation environment (MathWorks Matlab R2018a). The former averaged droplet is now discretized in thermodynamically coupled shells of equal radial thickness. This results in a continuous drop of shell mass from the droplet surface to its center, enhancing numerical stability in the gas-phase adjacent shell. In order to maintain the relative shell mass distribution, the shell thickness is evenly reduced during the gasification process. Figure 6.4 shows the droplet discretization method along with the additionally solved differential equations in the surface shell.

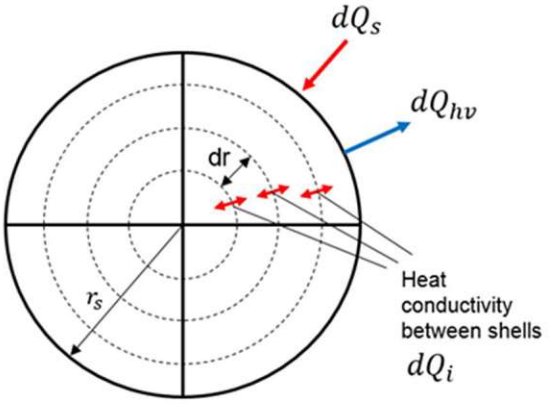

$$m_d * c_{p,d} * \frac{dT_d}{dt} = \frac{dQ_s}{dt} + \frac{dQ_{hv}}{dt} - \frac{dQ_{cond}}{dt}$$

$$\frac{dQ_{cond}}{dt} = k * A_{interface} * \left(\frac{T_{outer\ shell} - T_{inner\ shel}}{dr}\right)$$

Figure 6.4: Droplet discretization method.

The surface shell is the only one that interacts with the gas environment. The inner shells are coupled through heat conductivity. Consequently, the heat and mass transfer between the gas phase and the droplet is defined by the thermodynamic state of the surface shell.

In order to visualize the influence of the droplet discretization, the simulation is performed using the infinite conductivity approach (1 shell) as well as the droplet discretization method. Figure 6.5, shows the results achieved using 15 shells.

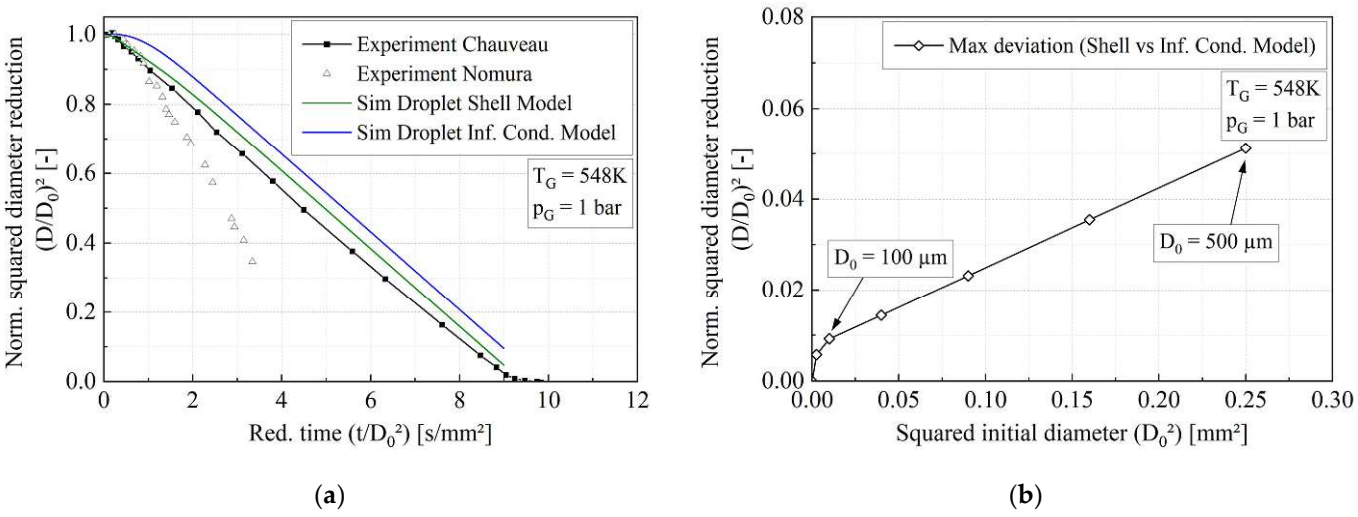

Figure 6.5: Infinite conductivity model vs. Shell model. (**a**) Results at 548 K and 1 bar using 15 droplet divisions, (**b**) Diameter dependency of the maximum error.

The implementation of the droplet discretization reduces the deviation between measurement data and simulation significantly. However, there is no further improvement in accuracy observable even using higher resolved droplet models after the initial heat-up phase. Since the origin of deviation is the missing heat conductivity model, the error scales linearly with the square of the initial droplet diameter. In the upcoming CFD simulations, the expected droplet sizes are well below 500 µm considering high-pressure fuel injection and potential oil droplet detachments [33, 34]. Therefore, CFD investigations will

be performed with the infinite conductivity approach. The reduction in prediction accuracy is acceptable in contrast to the significantly increased numerical effort.

6.2.2. *Fuel injection model and validation of the spray setup*

In order to properly fit numerical models, spray measurements were conducted and supplied by the manufacturer. The characterization of the spray droplet spectrum at a 50 mm distance from the nozzle tip was performed using a phase doppler anemometry (PDA) analysis. The nozzle tip distance ensures a fully evolved spray after primary and secondary droplet breakup. Furthermore, the temporal evolution of the axial spray penetration was captured using high-speed imaging. The orientation of every spray coil and its corresponding spray angle was determined using the footprint method. All measurements were carried out at 100 bar and 150 bar rail pressure using n-heptane, minimizing uncertainties with respect to fluid properties and experiment repeatability. However, at 150 bar rail pressure, only a limited set of parameters (SMD, DV_{90}, mass flow) were supplied. Table 6.2 shows the available spray data.

Table 6.2: Spray measurement data

Rail pressure	**100 bar**	**150 bar**
Ambient pressure	1 bar	1 bar
Number of Injector holes	6	6
Injector mass flow	25.70 kg/h	32.45 kg/h
Penetration length	High-speed imaging	Not available
PDA (SMD/DV_{90})	13.2 µm / 23.2 µm	10.7 µm / 16.1 µm
Spray coil orientation	Footprint measurement	Footprint measurement
Spray cone angle (outer/inner)	11° / 0°	11° / 0°

The experiment environment is replicated in numerical simulations using a box-shaped grid. The cell resolution is set accordingly to the determined requirement of section 6.2.1 and is further used in the CFD engine model. Therefore, a cell base size of 0.5 mm and an additional refinement to 0.25 mm in the near field of the nozzle tip (5 mm radius) is used. Furthermore, a time step size of 2.6 µs (= 0.025 °CA @ 1600 rpm) is applied to capture the highly transient injection process.

The injected droplets of the fuel spray are modeled as a dispersed phase within a Lagrangian framework (DDM approach), whereas the turbulent gas phase is treated as a continuous Eulerian phase. The secondary breakup of the droplets forced by aerodynamic-induced perturbations is considered using the Reitz-Diwakar model [99]. The selection of the used breakup model is based on a review of gasoline spray modeling by Duronio [100] and investigations performed by Paredi [101]. The latter compared a variety of breakup models on an Engine Combustion Network (ECN) Spray G Injector. The multi-hole injector was operated at 200 bar and thus resulted in similar boundary conditions to the injector at hand. The review stated that the liquid and vapor penetration lengths are best predicted using the Reitz-Diwakar as a secondary break-up model.

In order to maintain the validity of the DDM approach (low liquid volume fraction, discretely distributed parcels), the numerical droplet initialization is performed after the primary breakup has occurred. Consequently, the primary breakup of the liquid core into a dispersed droplet spectrum is not modeled explicitly. Instead, the initial droplet spectrum is described using a Rosin-Rammler distribution introducing 8 x 10^6 parcels per second and injector hole. The cumulative distribution function is determined by equation 6.4.

$$CDF = 1 - e^{\left[-\left(\frac{D_d}{X}\right)^q\right]} \tag{6.4}$$

X and q represent empirical parameters to calibrate the distribution function. The initial droplet velocity is estimated using equation 6.5.

$$\dot{m}_{spray} = \rho_l * u_{init} * A_{eff} \tag{6.5}$$

A_{eff} represents the effective nozzle hole cross-section area. The mass flow rate $\dot{m}_{spray}$ appears to be almost linear during the measured injection events. Only at very short injection pulses, a non-linear behavior could be observed. Since the investigation at hand does not include short-pulsed injection strategies, the mass flow rate is set constant for simulation purposes.

As a result, the described spray modeling approach offers three calibration parameters (X, q, A_{eff}) to iteratively optimize towards measurement data. Figure 6.6 shows the results achieved for a parameter set of X = 2.7 x 10^{-5}, q = 1.7, and an effective nozzle hole diameter of 125 µm.

Parameter set		
X	2.7 x 10^{-5}	
q	1.7	
A_{eff}	125 µm	
Droplet spectrum		
[µm]	100 bar Exp. | Sim.	150 bar Exp. | Sim.
SMD	13.2 | 13.1	10.7 | 10.0
DV_{10}	9.8 | 7.8	--
DV_{50}	16.4 | 16.5	--
DV_{90}	23.2 | 24.8	16.1 | 18.5

(a)

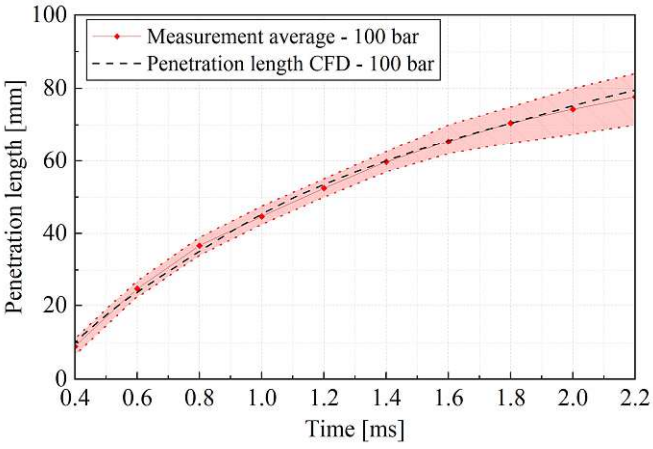

(b)

Figure 6.6: Comparison of the measured and simulated results. (**a**): Droplet spectrum, (**b**): Penetration length.

As mentioned above, the spray experiments are performed using n-heptane under atmospheric conditions. In order to transfer the numerical spray setting to the full engine CFD model, the differences in liquid densities (n-heptane vs. fuel) and ambient pressures must be considered. Assuming that the nozzle discharge coefficient remains constant in both operating conditions, the mass flow rate can be estimated according to equation 6.6. Performing this calculation by assuming an average combustion

chamber pressure of 2.5 bar (abs) during the injection process, the mass flow rate increases slightly to 26.65 kg/h at 100 bar and 33.73 kg/h at 150 bar rail pressure.

$$\dot{m}_{eff} = \dot{m}_{th} * c_d$$

$$c_d = c_A * c_v \rightarrow c_A = \frac{A_{eff}}{A_{geo}} ; c_v = \frac{u_{eff}}{u_{Bern}}$$

$$u_{Bern} = \sqrt{\frac{2 * (p_{Rail} - p_{Ambient})}{\rho_l}}$$

$$\dot{m}_{eff,fuel} = \rho_{Fuel} * \sqrt{\frac{2 * (p_{Rail} - p_{Cyl})}{\rho_{Fuel}}} * \frac{A_{eff}}{A_{geo}} * \frac{\left(\frac{\dot{m}_{eff,C7H16}}{\rho_{C7H16} * A_{eff}}\right)}{\sqrt{\frac{2 * (p_{Rail} - p_{Box})}{\rho_{C7H16}}}} \quad (6.6)$$

6.2.3. *Droplet / wall interaction*

The droplet / wall interaction is modeled according to the adjusted multi-regime Bai-Gosman impingement map of Heiß and Fischer [15, 94, 102]. The modifications to the impingement map are shown in Figure 6.7. This phenomenological model categorizes the dynamic physical processes of impinging droplets based on the wall temperature and the incoming Weber number. The droplet Weber number defines the kinetic impact and, as a result, the degree of disintegration of the incoming droplet. Ranging from a non-destructive rebound of the surface to stick, spread and splash regimes resulting in secondary rejected droplets and deposits. Regarding the thermal condition of the wall, two regime limits (T_S^*, T_L^*) are distinguished. Below the deposition limit T_S^*, the impinging droplets are able to form a liquid film on the surface. Above this threshold, the droplets are entirely rejected, and no wall films can be generated. Additionally, breakup regimes occur concerning the droplet Weber number. The second temperature-based regime limit is the Leidenfrost limit T_L^*. If the wall temperature surpasses this limit, the model suppresses the droplet / wall heat transfer completely. Although the formed vapor cushion isolates the droplet from the wall, there is still a heat transferred. Wruck [103] argued that the complete isolation assumption is an unphysical representation of the Leidenfrost effect. Therefore, the deposition limit T_S^* is set to the actual Leidenfrost temperature of the gasoline (= 1.47 x T_{sat} [15, 104, 105]), and T_L^* is modified to an arbitrarily high value to eliminate those regimes from the simulation model. Since the deposition limit is modeled dependent on the incoming fluid saturation temperature, the model is able to account for changes in fluid compositions due to evaporation. In the case of gasoline, the deposition limit may vary from ~475 K to 710 K (=483 K x 1.47), representing the standardized end of distillation according to DIN EN 228 [90].

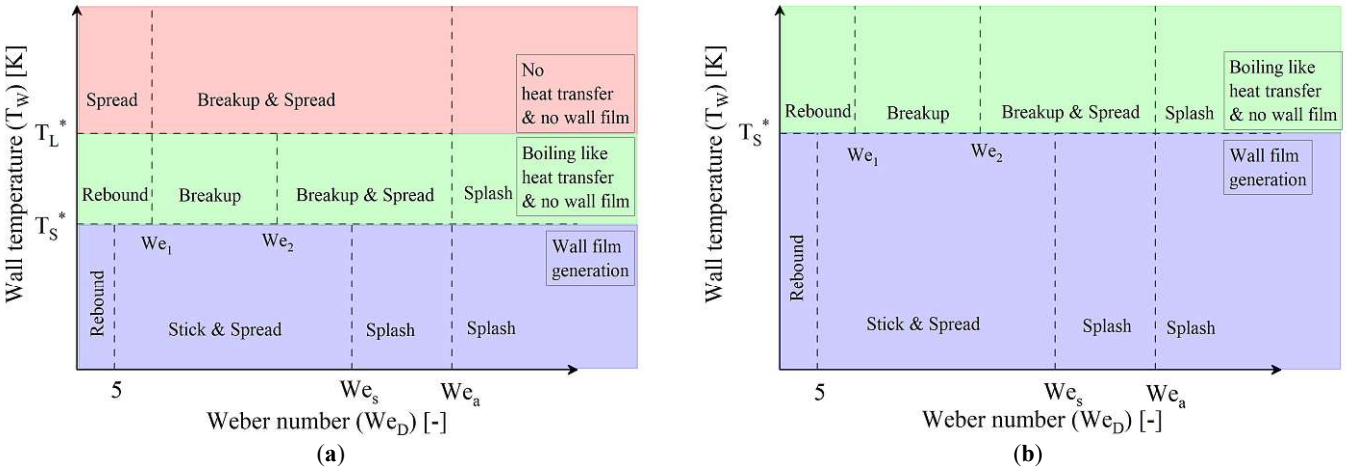

Figure 6.7: Implemented impingement map. (**a**) Original Bai-Gosman, (**b**) Modifications according to Heiß [15] and Fischer [102].

6.2.4. *Implementation of a multi-component fuel surrogate*

In order to model the mixture preparation process and wall film formation accurately within the engine domain, the evaporation characteristic of the given fuel needs to be taken into account. Previous numerical and optical investigations already showed that the simplification of using a single representative species like n-heptane lead to a significantly reduced prediction quality especially considering liquid film formation. [15, 106, 107, 108, 109, 110] During the fuel injection, the multi-component evaporation results in a de-mixing of species along the spray axis. High volatile components mainly evaporate close to the nozzle tip, whereas low-volatiles accumulate inside the droplets dominating the spray penetration length and possibly resulting in droplet impingement.

The evaporation characteristic of a given liquid can be deduced from the standardized distillation process according to ASTM D86 [111] and DIN EN ISO 3405 [112]. A 100 ml of liquid fuel is continuously heated up in a distillation flask during the test procedure, shown in Figure 6.8 (**a**). The liquid fuel evaporates and is guided through a vertical tube where the gas temperature is measured. The fuel vapor condenses afterwards on the walls of the chiller. From there, the liquid condensate is collected and the volume is measured. The heating power supply is adjusted to have a nearly constant evaporation volume flow rate of 4 to 5 ml per minute [112].

Fuels consist of numerous hydrocarbons leading to a smooth increase of the boiling temperature during the evaporation process. Therefore, a numerically describable multi-component surrogate fluid needs to be established that replicates the evaporation behavior of the real fuel. The selection of adequate species demands a detailed model describing the distillation measurement process. Therefore, a 0D model is created, dividing the distillation procedure into three sub-stages, shown in Figure 6.8 (**b**). The sub-stages represent the liquid-vapor interaction in the distillation flask (Boiler-stage), the mixing and heat up process in the gas phase (CSTR-stage), and the cooling and condensation of the vapor (Chiller).

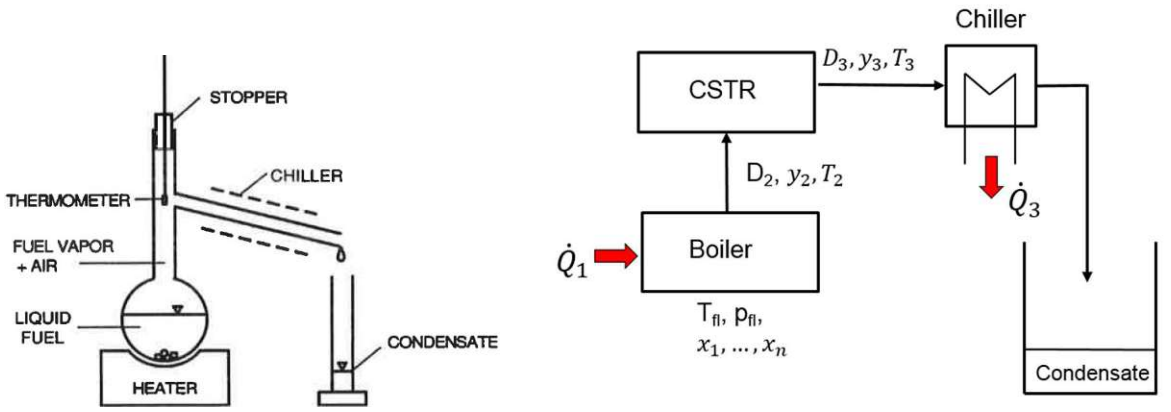

(**a**) (**b**)

Figure 6.8: (**a**) Overview of the standardized distillation apparatus [111], (**b**) Derived numerical model architecture.

The boiler stage is initialized with 100 ml of liquid fuel heating up to its boiling temperature. The main objective in this stage is to determine the vapor-liquid equilibrium (VLE). In order to account for mixture effects in the liquid phase, activity coefficients are calculated for every species using the UNIFAC method [93, 113, 114]. The VLE can be solved at the boiling point according to equation 6.7 [115].

$$y_i * p_g = \gamma_i * x_i * p_i^s(T_B) \tag{6.7}$$

During the initial heat-up process, the liquid is not boiling, and thus, the equation shown above is not valid. DIN EN ISO 3405 and ASTM D86 define a time range of 60 to 100 seconds until 5 %-v/v has to be evaporated. This ensures a relatively short first heat-up period. During this time, the VLE and the resulting evaporated mass flux would have to be calculated using the film theory equations (shown in section 6.2.), leading to time-consuming calculations and additional fairly unknown parameters within the 0D model approach (i.e., Diffusion coefficients, effective liquid surface area). In order to avoid the modeling of the vague defined heat-up process and maintain a fast-running model, the Boiler stage assumes that the liquid inside the distillation flask reaches its boiling point instantaneously, acknowledging the fact of limited solution quality. However, this calculation method enables temporal discretization by using the evaporated mass flux instead of the elapsed time. This “timeless” approach is in accordance with the volume flow rate requirement of the distillation standards.

The calculated evaporated mass from the Boiler stage is transported to the Constant Steering Reactor (CSTR) stage. This stage accounts for the inherent inertia of the system. The logged temperature readings of the distillation process represent the gas temperature of the mixture inside the volume above the distillation flask. It consists of residual gas and is continuously partially displaced by new evaporated vapor sourced from the Boiler stage. At the beginning of the simulation, the system is filled up with air. In order to simplify the mixing process, it is assumed that the incoming vapor is perfectly mixed with the gas held in the CSTR volume. The constant modeled volume is set to 150 cm^3 representing the approximate volume of the distillation flask.

Additionally, the CSTR stage considers the cooling effect of the glass walls of the apparatus. The heat transfer cannot be determined accurately since important parameters are unknown (i.e., vapor-glass

and glass-ambient heat transfer coefficients). Therefore, the heat flux problem is simplified by the assumption that the walls are represented by a thermal heat capacity. The heat capacity C_{Wall} is fitted to 8.4 J/K representing ~10% of the real wall heat capacity of the entire distillation apparatus [116]. As a result, the temperature at the thermocouple can be iteratively solved using an energy balance considering the assumption made above, shown in equation 6.8.

$$T_3^t = \frac{\sum_{i=1}^{n}\left(D_{2,i} * c_{p,vap,i}(T_2)\right) * T_2 + \left(\sum_{i=1}^{n}\left(m_{CSTR,vap,i}^{t-1} * c_{p,vap,i}(T_3^{t-1})\right) + C_{Wall}\right) * T_3^{t-1}}{\sum_{i=1}^{n}\left(D_3 * c_{p,vap}(T_3^t)\right) + C_{Wall}} \tag{6.8}$$

The vapor mass flow that is pushed out of the CSTR stage enters the Chiller stage, where the species are condensed and collected.

The presented 0D distillation model is based on the already published model of Greenfield [116]. This very detailed model had to be simplified to meet the capabilities of CFD software.

Vapor-liquid equilibrium of miscible mixtures

An inherent problem of multi-component evaporation is the accurate calculation of the saturation pressure of the fluid mixture. The simplest and fastest calculation method is the application of Raoult's law which basically exclude all interactions between different species in the mixture. The vapor-liquid equilibrium of the ideal mixture is then a linear combination of the saturation pressures of the pure substances, shown in equation 6.9.

$$y_i * p_g = x_i * p_i^s(T_B) \tag{6.9}$$

Due to interactions of different species in the fluid, the linear combination can lead to high errors compared to measurement results. The most accurate way to consider this phenomenon is using a cubic form of the equation of state (EOS). A commonly used form is the expression of Soave-Redlich-Kwong and Peng-Robinson [98]. The major drawback of the modified EOS approach is that it needs measurement data to fit the binary correction factors, which are usually expressed as $k_{i,j}$.

In order to overcome this problem, the UNIQUAC method was introduced by Abrams, Maurer, and Prausnitz [113, 117, 118] and was later modified and renamed by Fredenslund (UNIFAC) [114]. The basic idea of this approach is that a molecule is considered as an aggregate of functional groups. These groups contribute to the mixture effects by a combinatoric interaction considering the molecular size and form and a molecular interaction (residual term) between each group. Both effects are finally expressed via the UNIFAC activity coefficient, shown in equations 6.10 to 6.12. This coefficient corrects the contribution of the saturation pressure in the mixture. [93]

$$ln(\gamma_i) = ln(\gamma_i^C) + ln(\gamma_i^R) \tag{6.10}$$

Combinatoric effect:

$$ln(\gamma_i^C) = ln\left(\frac{\phi_i}{x_i}\right) + \frac{z}{2} q_i ln\left(\frac{\theta_i}{\phi_i}\right) + l_i - \frac{\phi_i}{x_i}\sum_{j}^{nc}(x_j * l_j) \tag{6.11}$$

$$r_i = \sum_{k=1}^{ng(i)} \left(v_k^i * R_k\right) \qquad q_i = \sum_{k=1}^{ng(i)} \left(v_k^i * Q_k\right) \qquad \phi_i = \frac{r_i * x_i}{\sum_{j=1}^{nc}(r_j * x_j)}$$

$$\theta_i = \frac{q_i * x_i}{\sum_{j=1}^{nc}(q_j * x_j)} \qquad l_i = \frac{z}{2} * (r_i - q_i) - (r_i - 1)$$

Molecular effect:

$$ln(\gamma_i^R) = \sum_{k=1}^{ng(i)} v_k^i \left[ln(\Gamma_k) - ln\left(\Gamma_k^i\right)\right] \tag{6.12}$$

$$ln(\Gamma_k) = Q_k \left\{1 - ln\left[\sum_{m=1}^{ng}(\theta_m \psi_{mk})\right] - \sum_{m=1}^{ng}\left[\frac{\theta_m \psi_{km}}{\sum_{n=1}^{ng}(\theta_n * \psi_{nm})}\right]\right\}$$

$$\theta_m = \frac{Q_m * X_m}{\sum_{n=1}^{ng}(Q_n * X_n)} \qquad \psi_{mn} = e^{\left(-\frac{a_{mn}}{T}\right)} \qquad X_m = \frac{\sum_{j=1}^{nc}\left(x_j * v_m^j\right)}{\sum_{j=1}^{nc} x_j \sum_{k=1}^{ng} v_k^j}$$

γ_i^C	*UNIFAC activity coefficient contribution due to combinatoric interactions*
γ_i^R	*UNIFAC activity coefficient contribution due to molecular interactions*
v_k^i	*group k number in component i*
nc	*total number of components in the mixture*
$ng(i)$	*total number of groups in component i*
R_k, Q_k	*group k volume and area parameter*
a_{mn}	*group interaction parameter between groups*

R_k, Q_k and a_{nm} are model parameters that are tabulated for an extensive number of functional groups. In the investigation at hand, the provided data from Siemens StarCD CFD-code Version 4.30.029 is used.

Validation of the 0D distillation model

For validation purposes, already defined surrogate formulations by Batteh [119] and Greenfield [116] are used. The sample fluids incorporate species of all basic chemical configurations relevant for fuel modeling (n-alkanes, iso-paraffins, olefins, aromatics, naphthenes, oxygenates). Table 6.3 shows the species composition of an excerpt of all used surrogate fluids. All results achieved during the validation process are documented in Appendix section A-1.2. The thermodynamic properties of the fluids are implemented temperature-dependent according to the PPDS equation listed in VDI Heat Atlas [98] except for iso-octane. The NIST thermophysical database [120] is used for this species because it is not listed in the previously mentioned literature.

Table 6.3: An excerpt of the surrogate formulations published by Batteh [119] and Greenfield [116].

Species	Chemical group	Indolene [%-m/m]	Synfuel + 10.5 % Ethanol [%-m/m]
n-butane	Paraffin	4.00	-
Iso-pentane	Iso-paraffin	16.00	-
n-pentane	Paraffin	-	15.25
cyclopentane	Naphthenic	-	-
1-hexene	Olefin	-	-
n-hexane	Paraffin	2.50	-
Ethanol	Oxygenate (Alcohol)	-	10.48
Cyclohexane	Naphthenic	-	21.69
Iso-octane	Iso-paraffin	32.00	-
Toluene	Aromatic	25.50	15.53
n-octane	Paraffin	-	17.11
Ethylbenzene	Aromatic	-	11.38
n-decane	Paraffin	-	7.60
1,2,3-trimethylbenzene (TMB)	Aromatic	18.00	-
Naphthalene	Aromatic	-	1.05
Tridecane	Paraffin	2.00	-

In the following Figure 6.9, a comparison of the measured and modeled distillation curve is shown for two sample fluids. These fluids cover a wide variety of species used for validation and significantly differ in the alcoholic content. Additionally, the simulation results are shown using the ideal fluid mixture assumption ($\gamma = 1$) or the use of activity coefficients calculated by the UNIFAC method.

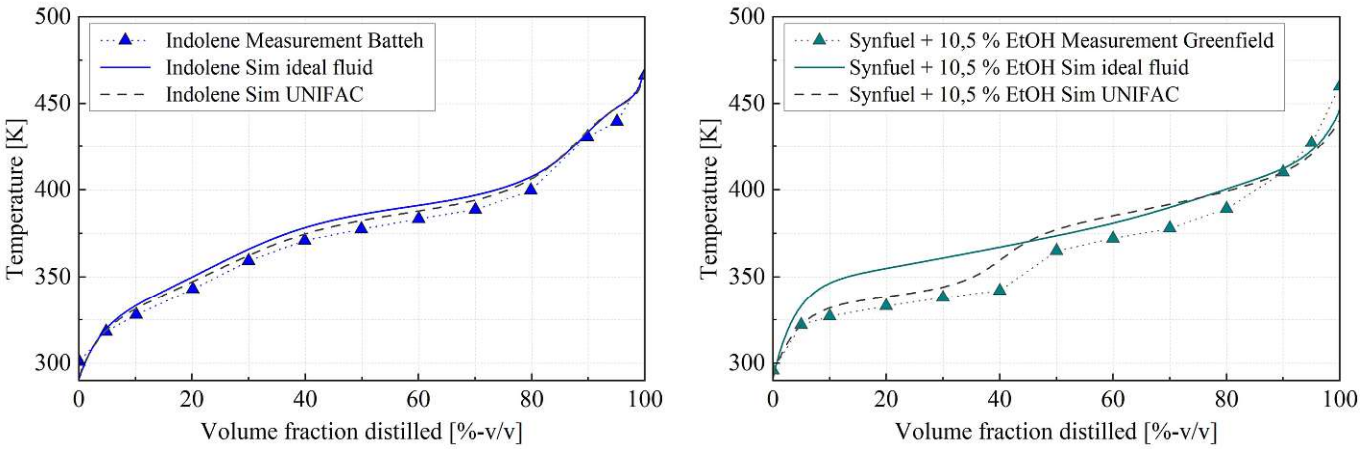

(**a**) (**b**)

Figure 6.9: Comparison of the measured and modeled distillation curve. (**a**) "Indolene", (**b**) "Synfuel + 10.5 % Ethanol".

The distillation model shows a good agreement with all measurement results. However, a slight shift towards higher temperatures can be observed in some sample fluid cases. The "Synfuel + 10.5% Ethanol" case clearly shows the influence of ethanol on the distillation temperature behavior. The polar hydroxy-group (R-OH) interacts with the other non-polar molecules in the liquid mixture resulting in a significant temperature jump at the time the ethanol is mostly evaporated. This strong interaction is expressed in high activity coefficients (γ = 4~9) shown in Figure 6.10. In such cases, the assumption of ideal fluid mixtures is not valid and further highlights the importance of mixture effects in ethanol-blended gasoline fuels.

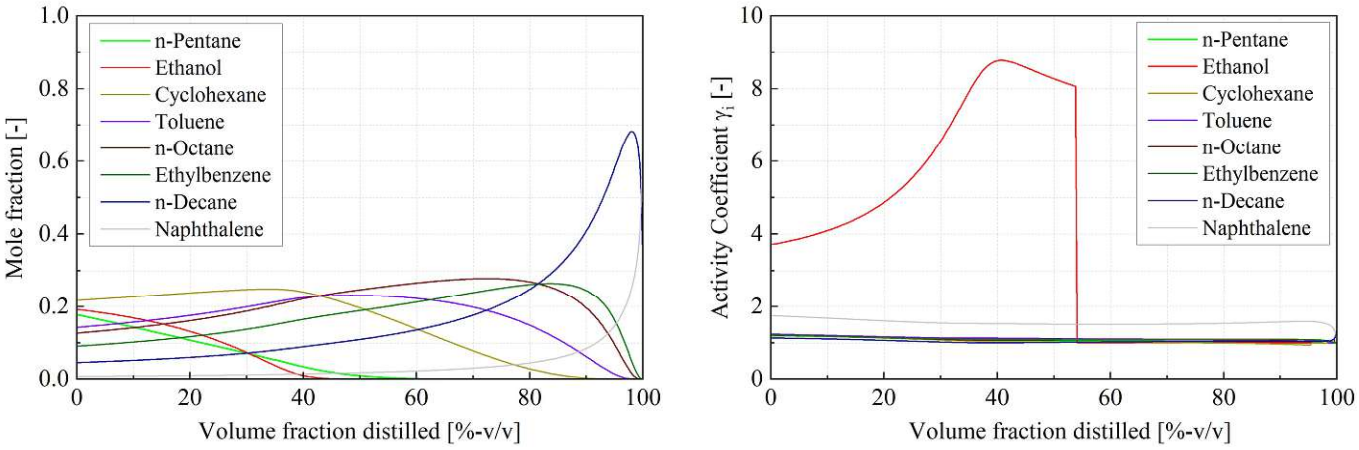

Figure 6.10: Temporal evolution of the mole fractions (**a**) and the corresponding calculated UNIFAC activity coefficients (**b**) in the "Synfuel + 10.5% Ethanol" case.

Fuel component selection

The requirements for the surrogate fuel are to reproduce the evaporation behavior of the real fuel by replicating the measured distillation curve. Additionally, the basic chemical compositions by means of paraffins, olefins, naphthenes, aromatics, and oxygenates content should be met to incorporate mixture effects in the liquid phase. Simultaneously, the number of species within the mixture should be as low as possible to reduce the numerical efforts.

In order to use only validated species data, the selection is limited to the presented components in Table 6.3 of the previous section. After several iterations, an 11-component mixture could be found that suits all aforementioned requirements. Figure 6.11 shows the comparison between measured data and the final modeling result. Furthermore, the temporal evolution of the species mole fraction and the calculated activity coefficients are shown.

Chemical Subgroup	Unit	Measurement	Surrogate
Paraffins	[%-*v*/*v*]	15.3	16.0
Iso-Paraffins	[%-*v*/*v*]	29.7	30.3
Olefins	[%-*v*/*v*]	9.7	9.9
Naphthenes	[%-*v*/*v*]	6.9	7.0
Aromatics	[%-*v*/*v*]	28.8	28.3
Ethanol	[%-*v*/*v*]	8.3	8.5
Unknowns	[%-*v*/*v*]	1.4	0.0

Surrogate Species	Chemical Formula	BP @ 1 bar [K]	Mass fraction [-]
Iso-Pentane	C_5H_{12}	301.15	0.1
n-Pentane	C_5H_{12}	308.85	0.11
Cyclopentane	C_5H_{10}	321.95	0.07
1-Hexene	C_6H_{12}	336.25	0.09
Ethanol	C_2H_5OH	351.47	0.09
Iso-Octane	C_8H_{18}	372.15	0.17
Toluene	C_7H_8	384.15	0.02
Ethylbenzene	C_8H_{10}	408.85	0.13
1,2,3-Trimethylbenzene	C_9H_{12}	449.15	0.14
Naphthalene	$C_{10}H_8$	490.55	0.05
n-Tridecane	$C_{13}H_{28}$	508.15	0.03

(**a**)

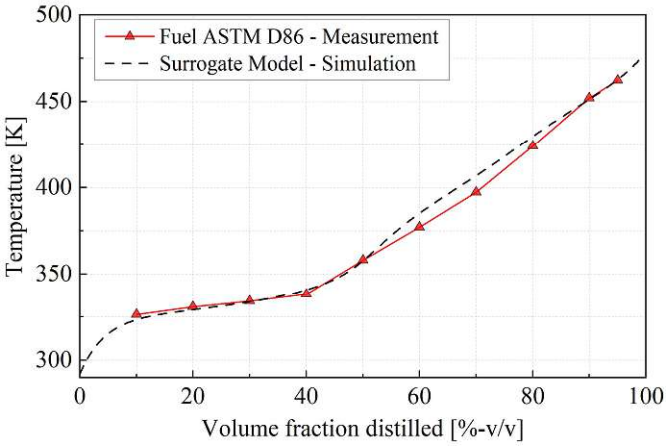

(**b**)

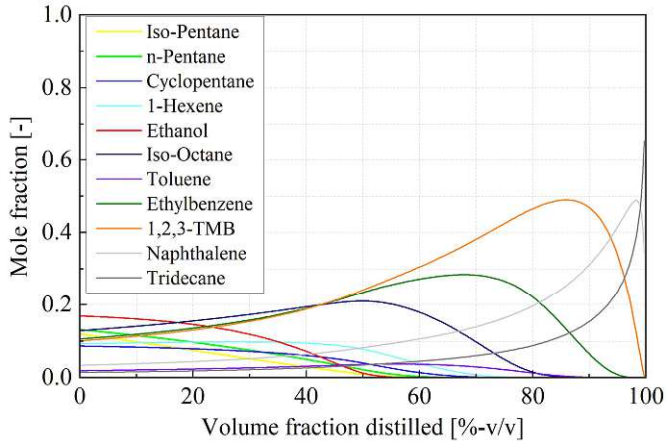

(**c**)

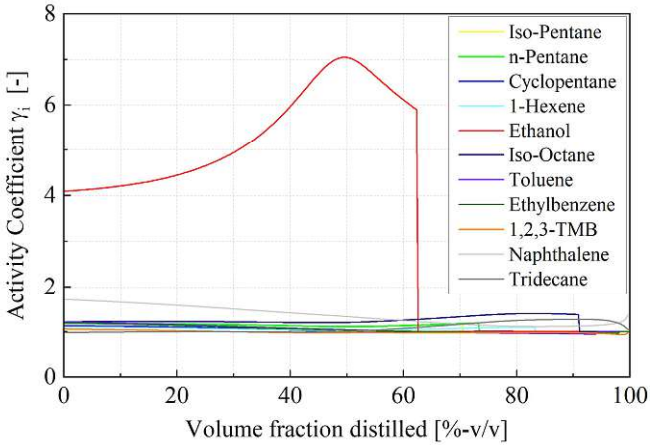

(**d**)

Figure 6.11: Overview of the results achieved using the established 11-component fuel surrogate model. (**a**) Summary of the species selection, (**b**) Measured vs. simulated distillation curve, (**c**) Evolution of the species mole fractions in the liquid phase during the distillation process, (**d**) Evolution of the calculated activity coefficients during the distillation process.

The achieved composition matches the measured distillation curve as well as the basic chemical composition exceptionally well. The deviation from the experimentally obtained distillation curve is

within 10 K. Furthermore, the model was capable of replicating the characteristic jump in temperature resulting from mixture effects induced by the ethanol share. Additionally, the deviation of the basic chemical composition of the generated fuel surrogate stays within 0.7 %-v/v of the real fuel. Nevertheless, the high modeling accuracy comes along with a fairly high number of species and thus computational effort.

6.3. Impact of fuel evaporation and liquid film formation on LSPI

In order to identify the impact of fuel evaporation and liquid film formation, the presented CFD engine model is parameterized according to measurement data achieved running the engine at three different injection strategies. Based on the load point specification given in section 5.1., the injection pressure and the start of injection (SOI) event are varied, resulting in different states of homogenization. Measurements showed that the manipulation of these parameters has a significant impact on LSPI frequency and therefore are selected to model numerically. Table 6.4 summarizes the investigated load point specifications and the corresponding measured LSPI frequencies.

Table 6.4: Overview of investigated operation points.

Parameter	Unit	OP 1	OP 2	OP 3
Speed	[rpm]	1600	1600	1600
Torque	[Nm]	200	200	200
$\lambda_{Exhaust}$	[-]	1.08	1.08	1.08
IGN	[°CA bTDCf]	-4	-4	-4
Injection strategy	[-]	Single-pulse	Single-pulse	Single-pulse
SOI	[°CA bTDCf]	250	250	280
p_{Rail}	[bar]	100	150	150
LSPI frequency	[# / 50,000 Cycles]	65*	15	4

* Extrapolated data from 20,000 cycles.

Considering the model initialization, the start of simulation is set to 270 °CA aTDCf. At this time, the exhaust valves are widely open, ensuring low temperature, pressure, and velocity gradients enhancing numerical stability. Furthermore, the remaining crank angles till TDC are used to pre-condition the engine-specific in-cylinder flow field. Potential residual gas is neglected in the model initialization process. This assumption is expected to have a minor impact on the simulation results, considering the fairly wide valve overlap of 53 °CA accompanied by a positive pressure gradient from the intake to the exhaust manifold, promoting scavenging operation. The simulation runtime is limited to one engine cycle and ends at spark timing.

Figure 6.12 shows the spatial distribution of the liquid films inside the combustion chamber at 600 °CA aTDCf. Additionally, the temporal evolution of the film mass is shown in Figure 6.13.

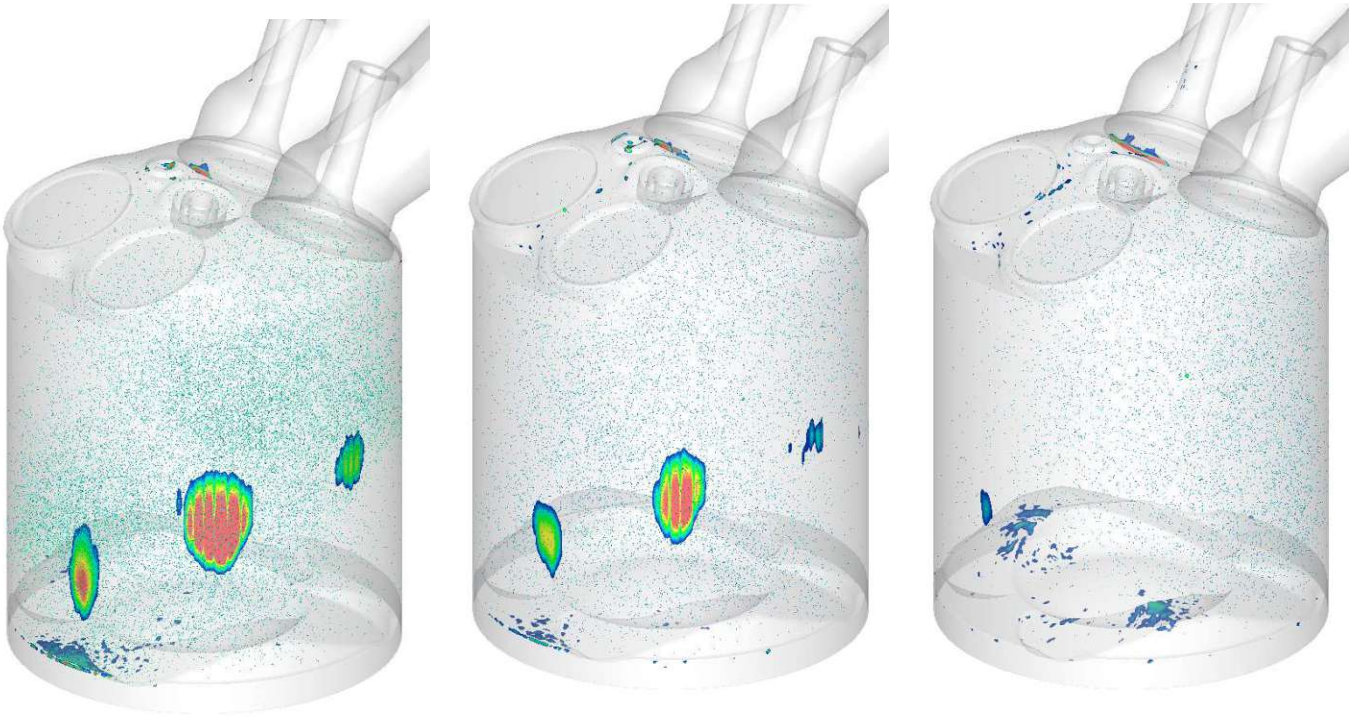

(**a**) „OP 1“ (**b**) „OP 2“ (**c**) „OP 3“

Figure 6.12: Liquid film distribution inside the combustion chamber at 600 °CA aTDCf.

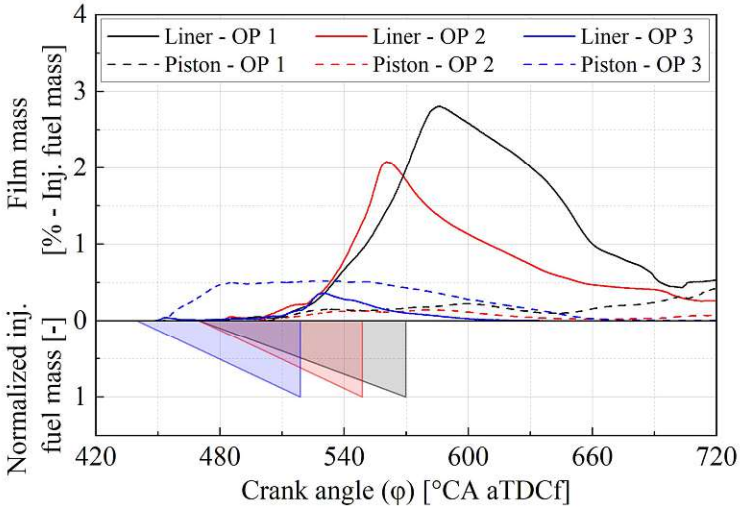

Figure 6.13: Temporal evolution of the liquid film mass.

Operation point 1 (OP 1) shows the most pronounced accumulation of liquid film mass during the injection process. The film is located in three distinct areas on the cylinder liner and additionally on the piston top land near the piston crevice. The fuel-wetted area on the piston top land correlates with the optically observed ignition location in case of “deposit-driven” LSPI events. Furthermore, it can be observed that the wetted piston area coincides vertically with a distinct fuel-wetted liner area. Due to the decreasing tumble-dominated charge motion velocity, the film mass peaks near the bottom dead center (BDC). Similar behavior can be observed for OP 2. The enhanced injection pressure and thus mass

flow rate leads to higher droplet weber numbers resulting in smaller droplet sizes. Therefore, the overall impinged mass on the cylinder surfaces is reduced. In both cases, the heat transfer from the walls to the wetted areas is too low to evaporate the film sufficiently before the piston rings wipe off accumulated fuel. However, the results with advanced SOI (OP 3) reveal a significant reduction in wall film mass. The apparent tumble flow motion is able to deflect the droplets from the liner surface. Nevertheless, the advanced injection timing results in a reduced distance between the piston and the nozzle tip. Consequently, the maximum observable film mass on the piston top land is higher compared to OP 1 & OP 2. Furthermore, the fuel-wetted areas on the piston top land differ significantly from the other investigated cases.

A correlation with the initial LSPI counts at the testbed can be found, considering the observable wall film mass on the piston and liner surface at spark timing (IGN). Figure 6.14 shows the normalized results based on OP 1. Since OP 1 appears to have a very high LSPI frequency, the LSPI count measurements are performed for 20,000 cycles compared to 50,000 cycles in the case of OP 2 & OP 3. This modified test procedure is implemented to protect the engine testbed setup from severe damage. Consequently, the readings for OP 1 have to be extrapolated to 50,000 cycles. It should be noted that the temporal distribution of LSPI events is not homogenous. Therefore, one has to acknowledge an increased uncertainty regarding the extrapolated value of OP 1.

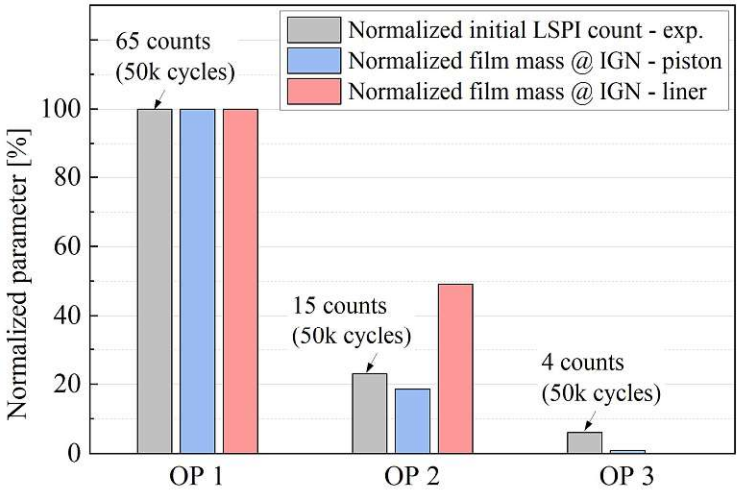

Figure 6.14: Correlation of initial LSPI counts and predicted wall film mass at IGN.

A general trend can be observed for both investigated surface regions highlighting the importance of fuel accumulations in the LSPI initiation mechanism. Especially, the remaining film mass on the piston top land area appears to agree exceptionally well with experimental data. The significance of the piston film mass on the initial LSPI frequency is contrary to reported investigations in the literature [17, 20, 121, 122]. The correlation may result from the specific spatial film mass distribution on the piston top land near the crevice area of this engine setup. The possible interaction with the wetted area on the liner indicates a superimposing effect of a local oil dilution, resulting in increased mobility of oil-fuel mixtures, and pronounced pool fires near the piston crevice area, promoting deposit formation and detachment.

Concerning the liquid film composition at spark timing, the aforementioned hypothesis is supported by a strong de-mixing effect of the fuel species. Figure 6.15 shows the species mass fractions for all

simulated cases at spark timing. Furthermore, the species are sorted according to their normal boiling point (NBP) temperatures. Additionally, the 11 components are combined into subgroups called “Light”, “Medium”, and “Heavy”. A species is considered “Light” if the NBP falls below 336 K, representing the distillation measurement's 33 %-v/v fraction distilled temperature. Species with an NBP above 384 K (67 %-v/v) are considered “Heavy”.

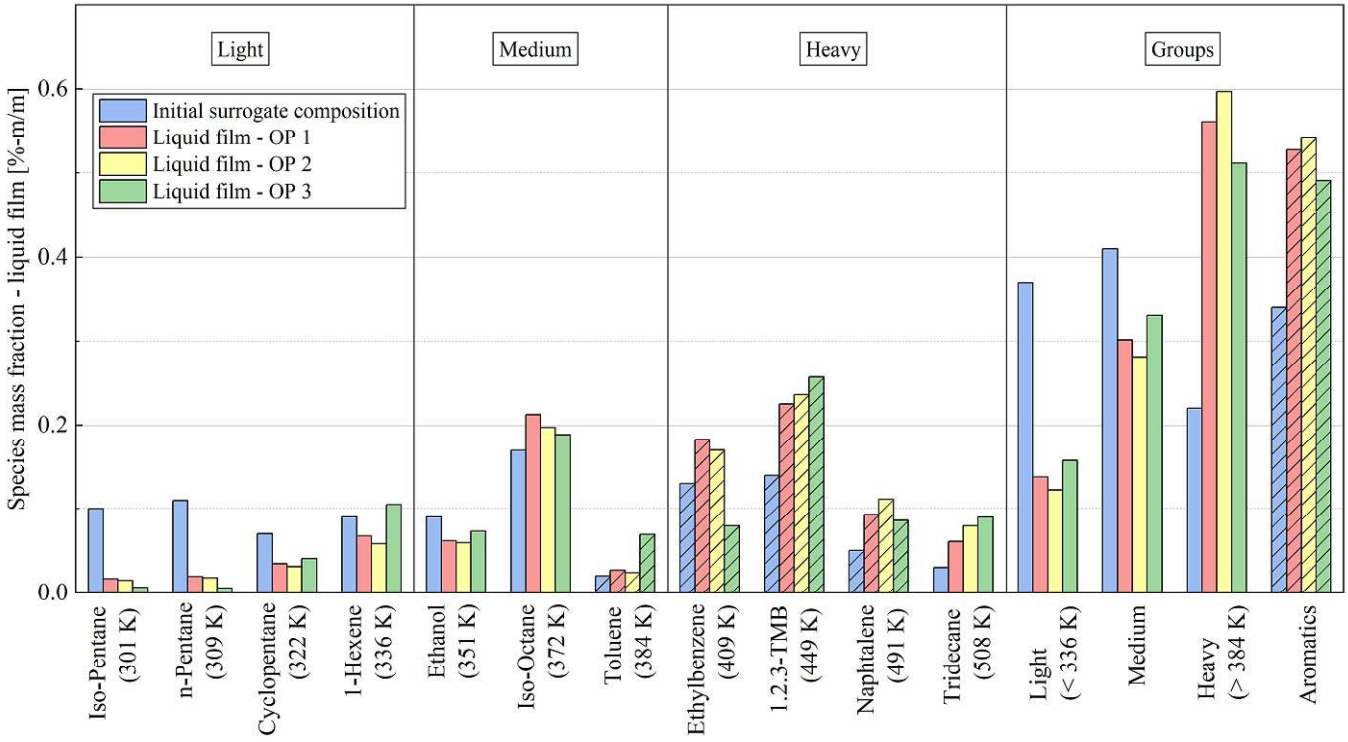

Figure 6.15: Species mass fractions of the liquid film at IGN.

As expected, high-volatile species are almost completely evaporated from the fluid mixture, whereas low-volatiles accumulate. Species with a higher normal boiling point than iso-octane appear to accumulate in the liquid film for the surrogate at hand. Due to the fuel content restriction of benzene (≤ 1 %-v/v), toluene can be considered the highest-volatile aromatic species in a fuel blend [90, 98]. Consequently, the share of aromatics increases drastically towards spark timing compared to the non-evaporated fuel composition. As a result, diffusive pool fires triggered by conventional combustions are fed by highly aromatic fuels, further promoting deposit formation. However, no significant differences in liquid film composition can be observed for the investigated engine operation points.

In order to investigate the influence of the gas phase air-fuel homogenization, the simulation results achieved inside the combustion chamber are extracted and plotted in Figure 6.16. The scatter plot’s color bar represents the volume fraction of the cylinder charge where x- and y-axis values are fulfilled. The data is clipped at a minimum threshold of 0.2 %.

The Figure displays the situation at 680 °CA, 700 °CA, and TDC, where “object-driven” and “deposit-driven” ignition events could be observed. The mean lambda values remain almost constant for all investigated injection strategies in the shown timespan. Due to convective and diffusive transport, the relatively wide lambda distribution gets narrower towards TDC. As expected from the liquid film formation results, OP 1 shows the widest lambda span at TDC, ranging from 0.5 to 1.25. It can be

observed that the fuel-rich zones remain until spark timing resulting from continuously evaporating fuel puddles. In the case of OP 3, very fuel-rich gas-phase conditions ($\lambda < 0.6$) can be avoided by effectively reducing wall wetting.

The ongoing compression leads to an increase in the mean temperature level. As a result, the temperature difference between the walls and the gas phase increases. Therefore, the gas temperature bandwidth tends to increase towards TDC slightly in all cases ranging from approx. 600 K to 710 K at TDC. Furthermore, it can be observed that the displayed parameters are not entirely independent. Fuel-rich areas appear to be colder than lean regions. This is caused by the cooling effect of evaporating fuel droplets and films.

The observable homogenization quality increases from OP 1 to OP 3, manifesting in higher cylinder volume fractions near the mean in-cylinder conditions. However, the overall observable bandwidth of data is only marginally smaller for the investigated cases.

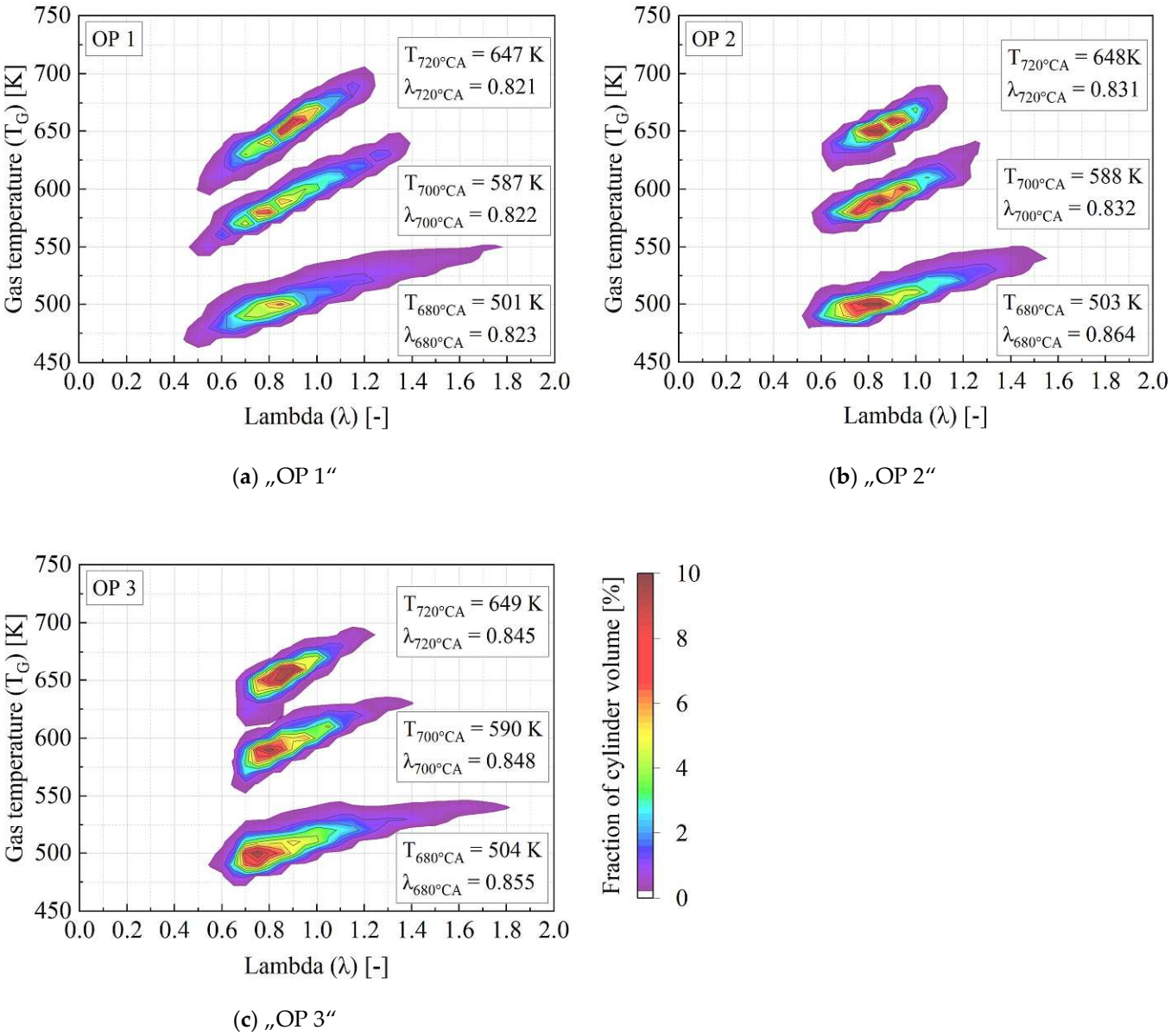

(**a**) „OP 1“

(**b**) „OP 2“

(**c**) „OP 3“

Figure 6.16: Gas temperature and air-fuel ratio distribution inside the combustion chamber.

Validity of the CFD engine model simulation results

In order to ensure CFD model prediction validity, the simulation results are compared with measurement data achieved running the engine at operation point 1 (OP 1). The experiments are performed using fluorescence dye-doped fuel, tracking the fuel droplet impingements inside the combustion chamber. Figure 6.17 shows the correlation between predicted liquid films and optically detected film-prone areas.

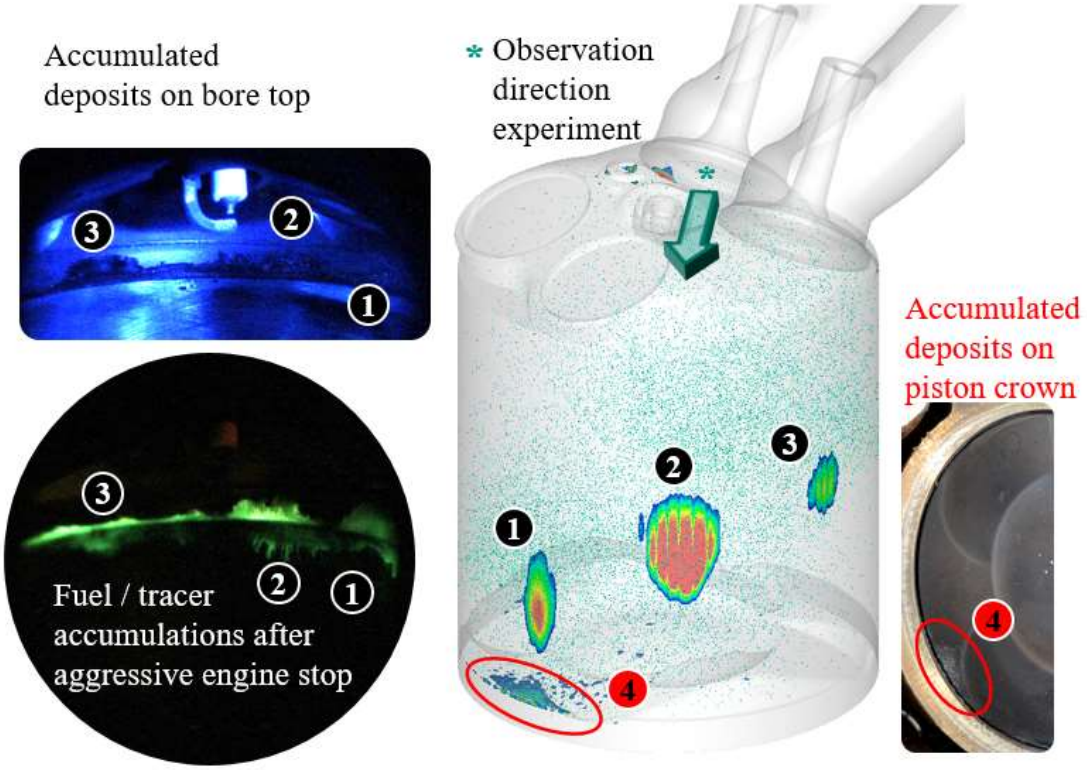

Figure 6.17: Correlation between predicted and optically detected fuel film-prone areas

The CFD model predictions and the experimental result are in excellent agreement. The film-prone areas on the cylinder liner and the piston top land are well predicted. Furthermore, the disassembling of the engine for visual inspection revealed that the predicted wall film areas coincide with pronounced deposit formation. In the case of the cylinder liner, the formed deposits are accumulated at the bore top region as a result of the vertical scraping effect of the piston rings.

In addition to the fuel spray and liquid film formation validation, the thermodynamic conditions inside the combustion chamber as well as the assumption of neglectable residual gases, are validated. Therefore, the measured in-cylinder pressure signal during the compression stroke is used as an indicator for the thermodynamic condition. The pressure trace is influenced by the pressure at IVC (trapped charge mass), the compression ratio, and the polytropic exponent. The latter is a function of the gas temperature and composition, influenced by the fuel evaporation rate. Furthermore, a passive scalar is introduced to track the remaining residual gas inside the combustion chamber after the gas exchange process. The comparison of the measured and calculated pressure trace is shown in Figure 6.18. Additionally, the uncertainty bandwidth of the measurement data displayed by min/max values is illustrated.

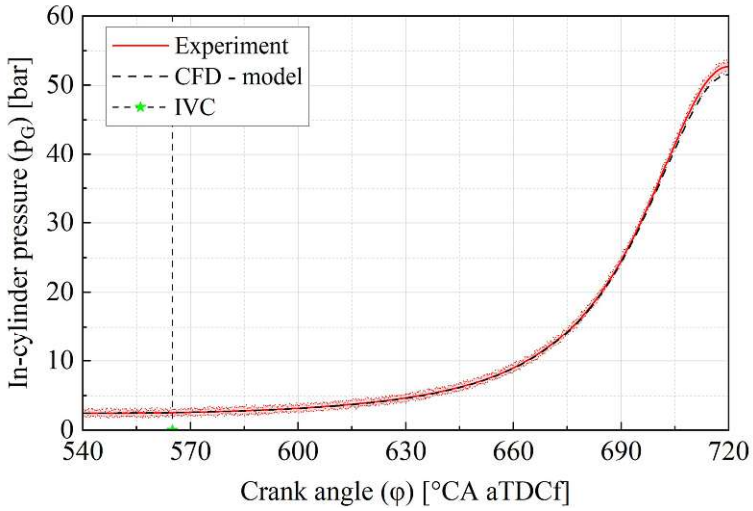

Figure 6.18: Validation of the in-cylinder pressure trace during the compression stroke.

The simulation results are in good agreement with the measurement data. Only a minor deviation from the mean experimental data can be observed near TDC. However, the numerically achieved data just falls within the lower uncertainty band of the experiments. Furthermore, the evaluation of the residual gas mass inside the combustion chamber after EVC confirmed the initially made assumption. The predicted residual mass fraction tracked by the passive scalar is well below 0.01 for all simulation cases.

7. Analysis of oil droplet-induced LSPI

7.1. Mechanism of droplet-induced ignitions

The hypothesis of droplet-induced ignitions assumes that detached oil or oil-fuel droplets inside the combustion chamber can reach a thermodynamic state where they are able to ignite the pre-mixed charge. In this case, the evaporating droplet supplies more reactive species like long-chained hydrocarbons to the auto-ignition resilient surrounding air-fuel mixture, accelerating chemical kinetics. On the other hand, the heat of vaporization cools down the ambient gas phase resulting in a conflicting spatial distribution of reactive species concentration and gas temperature, exemplarily shown in Figure 7.1. As a result, the highest reaction speeds are found at some distance to the droplet surface, typically near stoichiometric conditions.

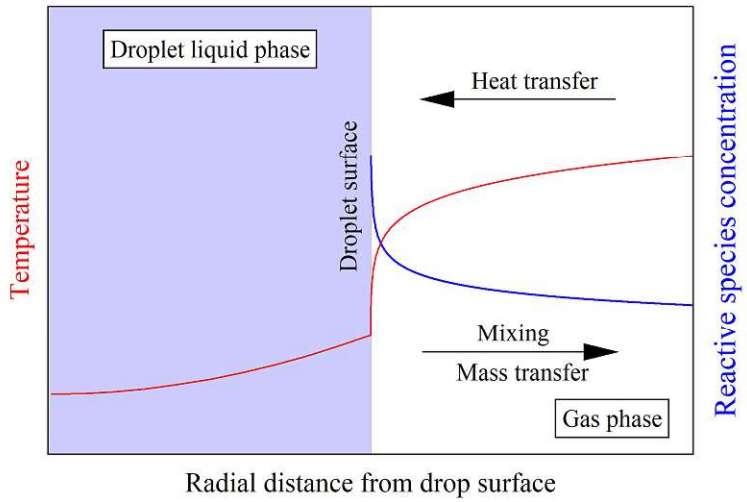

Figure 7.1: Schematic spatial distribution of reactive species concentration and gas temperature.

Since the expected droplet and gas-phase temperatures inside the combustion chamber are well below 1200 K, the low-temperature hydrocarbon oxidation pathway, characterized by the accumulation of ketohydroperoxide species resulting in the appearance of a “cool-flame”, is dominant. The occurrence of a local ignition and the associated heat release increases the heat transfer to the droplet surface, enhancing the droplet evaporation rate. The droplet surface temperature is limited by the apparent saturation temperature of the liquid phase. In addition, the concentration of the oxidizer is continuously reduced, approaching the droplet surface. This limits the distance to the established hot reaction zone. Therefore, a low-temperature dominated oxidation regime exists even after establishing an outward propagating flame front.

7.2. Determination of ignition delay potentials using chemical kinetics

In order to study the impact on the auto-ignition tendency of fuel and oil, a chemical kinetic model is introduced. Therefore, a well-validated TRF mechanism by Andrae [123] consisting of 137 species and 633 reactions is utilized to determine the reaction kinetic speeds.

In a first step, the sensitivity of varying mixture compositions and thermodynamic conditions is investigated in a homogeneous reactor model. This analysis provides further insight into pre-mixed ignition delays and can be used as a baseline for necessary conditions leading to autoignition under engine-relevant time scales. In a second step, a stochastic oil droplet release model is introduced to determine possible mixture properties in the vicinity of the oil droplet under engine-relevant conditions. The results are then feedbacked into the homogeneous reactor model to identify autoignition-prone conditions.

Chemical representation of fuel, oil, and air

In order to perform the prior mentioned analysis, surrogate fluids have to be defined to model the chemical reactivity of the very complex real fluids. In the case of the investigated fuel, the modified Linear-by-Volume (mLbV) response surface approach by Morgan [124] is utilized to model the fuel reactivity. The author did a comprehensive analysis of ignition delays using varying gasoline fuels in a rapid compression machine (RCM). It was possible to replicate the experimental autoignition delays by a toluene reference fuel (TRF) using adjusted volume fractions of n-heptane, iso-octane, and toluene calculated by equations 7.1 to 7.3. The empirically fitted coefficients a_i are summarized in Table 7.1. A TRF mixture can be iteratively determined by applying this model to the fuel at hand. The achieved TRF composition is outlined in Table 7.2.

$$p = \frac{VF_{Iso-octane}}{\left(VF_{Iso-octane} + VF_{n-Heptane}\right)} \tag{7.1}$$

$$RON = a_{p,RON} * p + a_{tol,RON} * VF_{tol} + a_{tol^2,RON} * VF_{tol}^2 + a_{tol,p,RON} * VF_{tol} * p \tag{7.2}$$

$$MON = a_{p,MON} * p + a_{tol,MON} * VF_{tol} + a_{tol^2,MON} * VF_{tol}^2 + a_{tol,p,MON} * VF_{tol} * p \tag{7.3}$$

Table 7.1: Overview of the coefficients used in the modified Linear-by-Volume surface response model [124].

Coefficient	a_p	a_{tol}	a_{tol^2}	$a_{tol,p}$
RON	100	142.79	-22.651	-111.95
MON	100	128.00	-19.207	-119.24

Table 7.2: Reaction kinetic surrogate formulation of the investigated fuel.

Fuel Specification	**Value**
RON	96.5
MON	86.0
Surrogate species	**Mass fraction [-]**
Iso-octane	0.1246
n-Heptane	0.1565
Toluene	0.7189

Lubricating oil consists of hydrocarbon species up to C54 [125, 126]. A detailed representation of the oxidation kinetics of the numerous possible configurations for such large molecules results in an unacceptable high demand for computational power [127, 128, 129]. Consequently, a simplified single species surrogate is typically chosen to mimic the high reactivity of large alkanes. Westbrook [128] showed that the chemical reactivity of n-heptane is remarkably similar to larger n-alkanes (up to C16). Therefore, the well-studied n-heptane oxidation mechanism is chosen in this investigation since it has been successfully applied in numerous studies to simulate long-chained hydrocarbon ignition phenomena under engine-like conditions [130, 131, 132, 133].

With respect to air, a binary mixture of oxygen (23.2 %-m/m) and nitrogen (76.8 %-m/m) is used in the simulations.

7.2.1. Homogeneous reactor model

In the following analysis, the resulting reaction kinetic speed and thus ignition delay times under homogeneously pre-mixed conditions are investigated. The gradient-free solution of the problem reduces the complexity allowing for a 0D solving approach. Therefore, only the Arrhenius-based differential equations of the reaction kinetic mechanism need to be solved, speeding up simulation times significantly. In order to efficiently run numerous systematic variations, the set of differential equations is solved in MathWorks Matlab R2019b utilizing the toolbox “Cantera”. An adaptive time step size ranging from 0.1 µs to 1 ns is implemented to account for the high temporal gradients resulting from high reaction kinetic speed at elevated temperature levels. This user-coded feature controls the time step size within the given thresholds by checking the relative temperature increase after each time step. Limiting the maximum temperature increase to 0.03 % ensures an accurate representation of the temperature and reaction speed gradients.

In order to validate the accuracy of the used mechanism, the numeric results are compared with measurement data using stoichiometric iso-octane/air and n-heptane/air mixtures in RCM and shock tube experiments. Therefore, a broad database (over 600 data points) from several publications summarized by Goldsborough [134] and Gauthier [135] is used as a reference. The ignition delay time is defined as the time span from the beginning of the simulation to the appearance of the maximal temperature gradient in the simulation. This definition is in accordance with the usually used pressure gradient-based ignition detection in testbed investigations due to the thermodynamic coupling of pressure and temperature (equation of state). Since the reaction mechanism is already validated by the author (Andrae [123]) itself, the validation is limited to binary mixtures of iso-octane/air and n-heptane/air ensuring proper implementation. Figure 7.2 shows the achieved simulation results under constant pressure boundaries compared to experimental data. The red shaded area in Figure 7.2 (**a**) represents the scatter band of all experimental data.

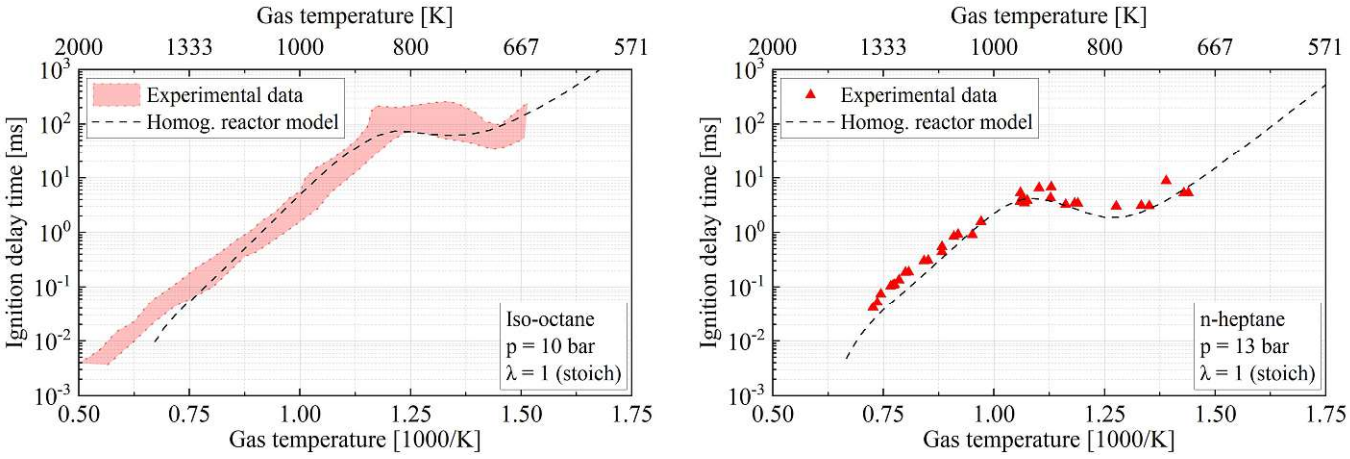

(**a**) Iso-octane / air (**b**) n-heptane / air

Figure 7.2: Ignition delay of stoichiometric iso-octane/air and n-heptane/air mixtures – gas temperature sweep.

Overall, a good correlation with measurement data over a wide range of gas temperatures can be accomplished. Only in very hot conditions do the predicted results deviate towards underestimated ignition delay times. Nevertheless, the maximum absolute deviation is in the magnitude of 10 µs representing ~0.1 °CA at 1600 rpm and is therefore acceptable.

The influence of increasing oil mass fractions on the ignition delay time can be investigated using the homogeneous reactor model. In order to evaluate the "worst-case" potential, the constant pressure level is set to 50 bar representing near TDC conditions. Figure 7.3 shows the ignition delay time plotted over the gas temperature and the air-fuel ratio of continuously increased oil mass fractions. The ignition delay time is converted to degree crank angle (°CA) at the investigated engine speed of 1600 rpm. The oil dosing is performed by replacing the air-fuel mixture with the highlighted amount of pure n-heptane. The displayed lambda values consider only the TRF fuel-air ratio and do not include all combustible substances resulting from oil dosing. Besides the colored illustration, iso-lines display conditions of equal ignition delay times. Each iso-line represents an increase of 6 °CA in ignition delay. Ignition delays longer than 90 °CA are shown in grey.

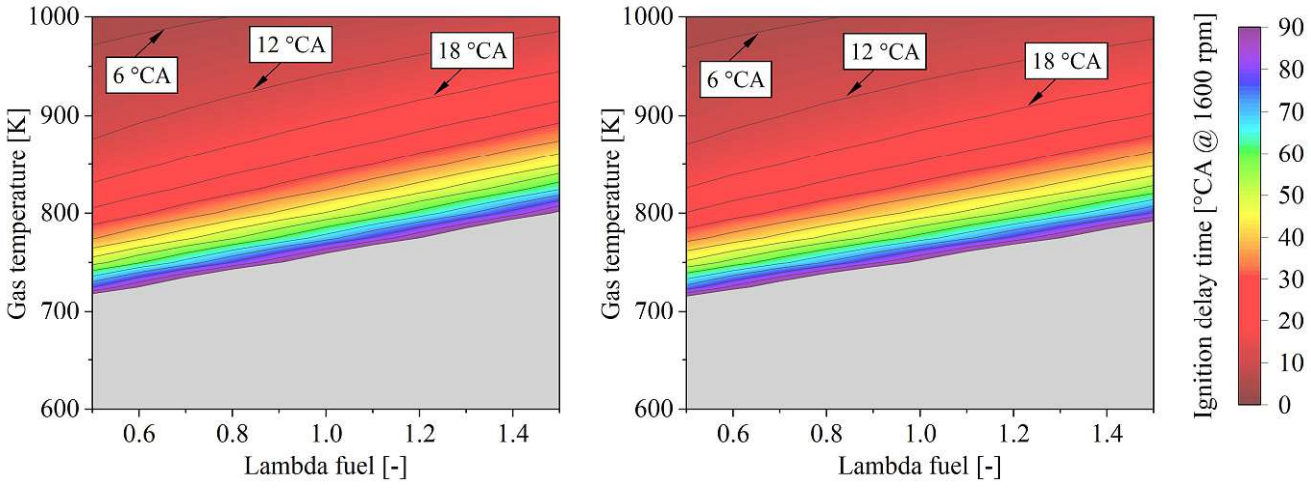

(**a**) No oil dosing (**b**) + 0.1 %-m/m oil

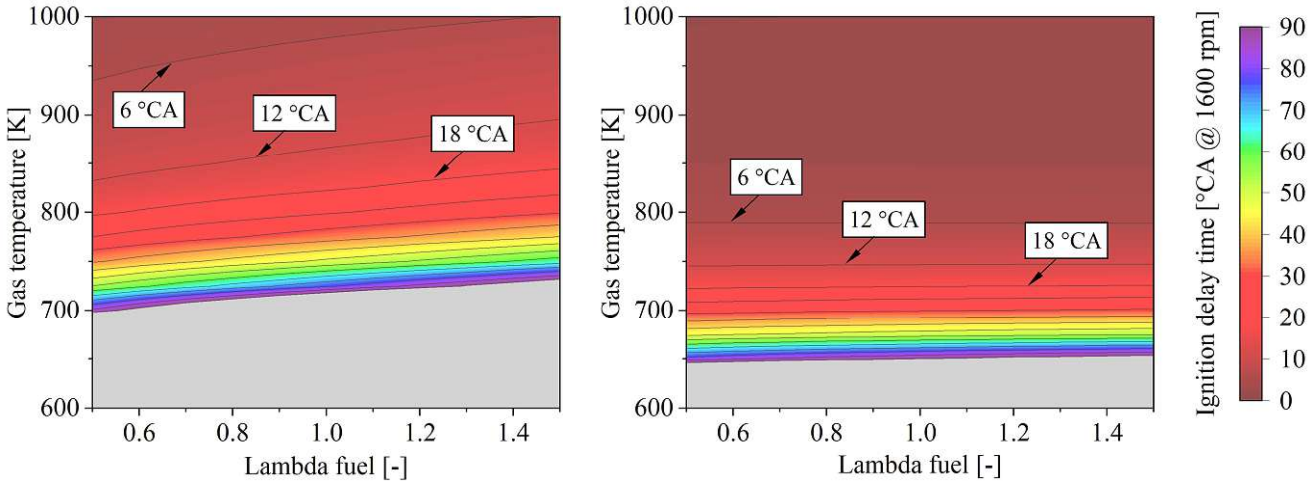

(**c**) +1 %-m/m oil (**d**) +10 %-m/m oil

Figure 7.3: Influence of oil dosing on the ignition delay time.

The simulations reveal that minor doses of n-heptane up to 0.1 % mass fraction have an insignificant impact on the overall ignition delay of the gas mixture. In order to achieve autoignition within 90 °CA, a minimum constant temperature of 715 K at an ambient fuel-based lambda of 0.5 is required. This temperature level represents the peak gas temperature found at TDC and is prevailing for a brief time span. With increasing oil dosing, the ignition delay times are further reduced, and additionally, the sensitivity to the ambient air-fuel ratio is reduced. This effect results from the dosing strategy, replacing parts of the ambient gas phase with n-heptane. As a result, the overall lambda value becomes insensitive to the ambient conditions. It can be observed that an almost constant minimum gas temperature threshold of 650 K has to be surpassed to ignite the mixture within 90 °CA. Considering the observed gas temperature and lambda ranges in section 6.3. (Figure 6.16), such conditions are limited to crank position of 700 °CA aTDCf onwards. Concerning the remaining time span of 20 °CA, even very high n-heptane shares up to 10 % are unlikely to induce an autoignition phenomenon.

7.2.2. Determination of oil droplet-induced mixture properties

The droplet evaporation and species transport generate various mixture compositions along the radial distance. The local reaction speeds are determined by the species concentrations and gas temperatures. Consequently, predicting the mixing process of evaporating detached oil droplets is crucial concerning droplet-induced ignitions.

Therefore, the described CFD engine model of section 6 is extended by a stochastic oil droplet release model accompanied by an oil surrogate fluid. Possible oil vapor concentrations and gas temperatures are determined by postprocessing the droplet vicinity during the compression stroke. The achieved results are used to assess the possibility of autoignitions using the homogeneous reactor model.

Physical representation of the oil droplets

The determination of the evaporation behavior via the standardized distillation method (described in section 6.2.4.) is not suitable for lubricating oils. Base stock oils consist of higher alkanes (> C16), resulting in normal boiling points above 700 K. Measurement readings would be interfered by the occurrence of thermal decomposition, exposing large hydrocarbon molecules such high temperature levels. Therefore, the data of a gas chromatography (GC) analysis is used according to the measurement procedure of DIN 51435 [136]. Since the methodology of a GC analysis is based on the physical separation of species by their molecule size, it avoids the issue of thermal decomposition. The identification of the species size and its corresponding normal boiling temperature is performed by comparing the signals with reference samples (n-alkanes). Unfortunately, the accurate separation of every species within the fluid mixture is hardly possible in the case of lubricating oil. Big molecules allow for various chemical configurations (i.e., isomers, cyclo-alkanes, n-alkanes) within a given carbon chain length. As a result, the individual signal peaks are not separated clearly and tend to form a continuous and broad signal peak. Nevertheless, the signal intensity can be correlated to the mass fraction within the fluid mixture. [137, 138]

The measurements are carried out by FUCHS Schmierstoffe GmbH using a 5W-20 base stock oil. Literature data suggest that the ignitability of long-chained hydrocarbons is mainly determined by the evaporation rate [44, 128, 129, 139]. Therefore, the data of the slightly more volatile 5W-20 lubricating oil may result in an overpredicted ignitability compared to the used 0W-30 specification.

For modeling purposes, a multi-component surrogate approach is chosen to be consistent with the fuel modeling strategy. The selection of the species is limited to n-alkanes due to the fact that fluid properties of long-chained isomers and other chemical configurations were not available. In the case of n-alkanes, a complete set of thermodynamic properties are available up to a molecule size of C19. Therefore, an extrapolation methodology is established to predict missing information of larger molecules. The methodology is discussed in the Appendix section A-1.3.

Based on the measurement results, a 4-component oil surrogate model is established. According to the Noack volatility test, species having an NBP above 773 K do not show any evaporation losses under motored engine conditions [63]. Although such species may have neglectable evaporation rates, they contribute to the overall heat capacity of the fluid mixture. Therefore, the lowest volatile component in the numeric surrogate is modeled as Tetracontane ($C_{40}H_{82}$) with a theoretical NBP of 795 K. Species below the Noack volatility temperature limit are discretized by surrogate species considering the GC signal. The most volatile components are discretized in more detail to account for their contribution in the early evaporation phase. Figure 7.4 shows the final surrogate composition in the context of the measured GC data.

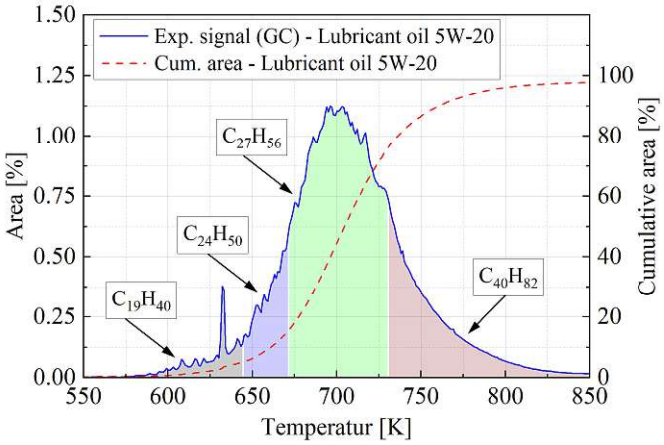

(**a**)

Species	Chemical formula	Mass fraction	NBP
Nonadecane	$C_{19}H_{40}$	0.05	603 K
Tetracosane	$C_{24}H_{50}$	0.1	664 K
Heptacosane	$C_{27}H_{56}$	0.6	694 K
Tetracontane	$C_{40}H_{82}$	0.25	796 K

(**b**)

Figure 7.4: Oil surrogate discretization. (**a**) GC measurement data, (**b**) surrogate mass fraction summary.

Oil droplet modeling approach

Predicting a statistically sufficient amount of droplet trajectories within the full engine CFD model requires a simplified droplet model approach. Therefore, the oil droplets are modeled as Lagrangian particles as outlined in section 6. This simulation approach limits the possible resolution of the establishing gradients by the present relation of the droplet and cell volume (VF threshold = 0.4) and the computationally feasible model size. In the case of the CFD engine model, the size is determined to be 0.5 mm by following the evaporation analysis in section 6.2.1.

In order to guarantee an appropriate model accuracy with respect to gradient capturing, the established CFD model using 0.5 mm cells in the framework of a DDM droplet model approach is validated against a detailed 1D single droplet ignition model published by Stauch [140, 141]. This model ensures high numerical resolution by timestep-wise reconfiguring the grid resolution depending on thermodynamic gradients. This feature realizes orders of magnitude higher grid resolutions near the droplet surface. Both models include the same chemical kinetic database and are parameterized by the same boundary conditions. Unfortunately, the results for the detailed model were limited to single-species surrogate representations. Therefore, the ambient is modeled as a stoichiometric iso-octane / air mixture, and the thermodynamic properties of the oil droplet are represented by neat n-heptane.

Figure 7.5 (**a**) shows the maximal observed gas temperature inside the simulation domain using two different sets of thermodynamic boundary conditions as well as droplet diameters. In Case 1, the parameters represent the average in-cylinder conditions of OP 1 at TDC. A droplet diameter of 250 µm ensures continuous droplet evaporation until autoignition occurs. In contrast, Case 2 uses a droplet diameter of 100 µm allowing the droplet to evaporate entirely prior to the autoignition event. Furthermore, the thermodynamic properties are varied to investigate the influence of lower ambient reaction kinetic speed and thus enhanced mixture preparation. Figure 7.5 (**b**) shows the comparison of the predicted ignition location with respect to the radial distance from the droplet surface.

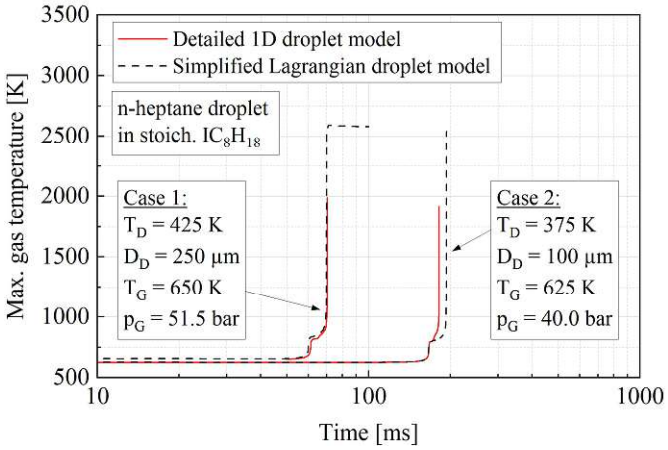

(**a**)

	Ignition location – Radial distance [mm]	
	Detailed model	Simplified model
Case 1	0.46	0.00
Case 2	0.54	1.00

(**b**)

Figure 7.5: (**a**) Temporal evolution of the maximal observed gas temperature in the simulation domain, (**b**) Derived ignition locations.

Overall, only minor deviations can be observed between the detailed and simplified droplet modeling approaches. The almost identical predicted ignition delay times indicate sufficient gradient capturing by the simplified model approach. The enhanced mixture preparation time of Case 2 did not show a significant impact on the predicted ignition location under engine-relevant ambient conditions. However, a slight trend towards increasing radial distances can be observed with both modeling approaches. Furthermore, the deviations between the predicted locations are within the discretization base size of the used grid (< 0.5 mm).

The expected evaporation rates fall short of the cases shown above using n-heptane, considering the lower saturation pressure of long-chained hydrocarbons used to model the physical properties of the lubricating oil. As a result, the cooling effect of the ambient gas phase due to the heat of evaporation is reduced. Consequently, lower gradients with respect to gas temperature and oil mass fractions can be expected in the vicinity of the droplet surface. In order to determine the influence on the predicted radial ignition location, the simplified model is re-parameterized to the previously discussed physical and chemical representations of fuel and oil. Figure 7.6 shows the achieved results using the boundary conditions of Case 1 representing TDC in-cylinder conditions.

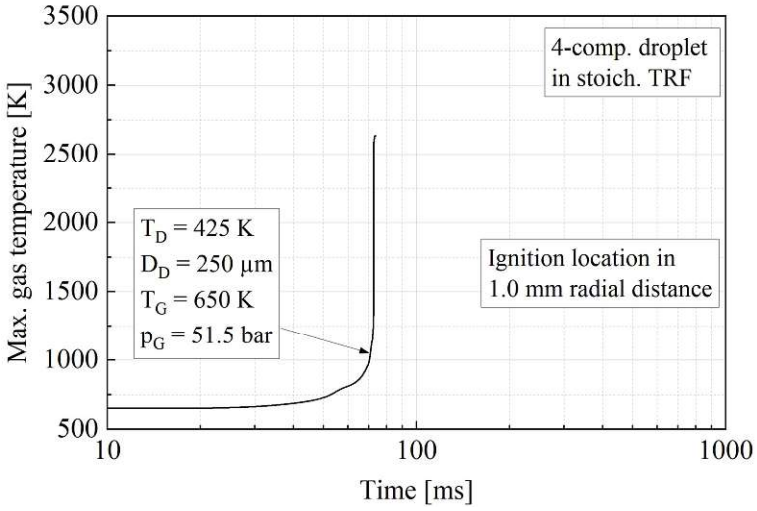

Figure 7.6: Temporal evolution of the maximal observed gas temperature for a stoichiometric TRF gas phase and a 4-component oil surrogate model.

Overall, a quite similar ignition delay can be observed for the detailed fluid models compared to the single-species surrogates (Case 1). Although the cooling effect due to evaporation is significantly reduced, the lack of reactive species leads to a low n-heptane gradient shifting the location of the highest reaction speed towards hotter ambient conditions.

It can be observed that the critical mixture conditions are achieved within a 1 mm radial distance from the surface under engine-relevant thermodynamic conditions, considering the simulated droplet-induced ignition cases.

Stochastic oil droplet release model

Regarding the droplet detachment, performed optical investigations did not show any evidence of statistically distributed droplet releases prior to LSPI events. Nevertheless, the possibility of droplet detachments out of the piston crevice area has been reported several times in the literature [26, 33, 34, 35, 36]. Unfortunately, the temporally distributed droplet release over several 10k cycles is not feasible due to enormous computational efforts. In order to cope with the computational performance limitations, a stochastic droplet injection approach is implemented in the model at hand. This suggested simulation approach is the logical continuation of the used ensemble-averaged flow computation (RANS) and the statistical representation of the fuel spray injection.

In order to get a good statistical representation of possible oil droplet trajectories and conditions, the modeling approach defines an injection of 360 oil droplets from 72 injection locations evenly distributed around the circumference of the piston. The injection strategy uses a spray cone angle of 90 °. The injection velocity is defined according to experimental and numerical observations made by Tanaka [33, 34], Doppler [36], and Moriyoshi [35]. The authors reported a scattering speed of ~1 m/s near TDC. Therefore, the initial oil droplet velocity is set to be 1 m/s higher than the current piston speed to avoid immediate re-impingement on the piston surface. Furthermore, the droplet size of 250 µm is defined according to the previously mentioned research, reporting droplet diameters ranging from 100 µm to 300 µm in the case of a low viscosity oil (0W-20). The initial droplet temperature is set to 425 K representing the oil temperature used to determine the High-Temperature High-Shear (HTHS) viscosity

of lubricating oils according to the CEC L-036-90 standard [142]. The test procedure refers this specific temperature level to the situation of piston-liner contact under heavy loads.

Due to missing experimental information on droplet detachment timings, the simulation results achieved in OP 1 (section 6) are used to define the most probable release timings. Two possible events can be identified considering the wall film formation and the predicted film dynamics. One possible event timing is at 630 °CA aTDCf. At this time, the piston wipes off the remaining fuel from the cylinder liner. The shear forces may induce perturbations leading to droplet detachment. Additionally, the fuel mass mixed with the lubricating oil reduces the fluid viscosity and further promotes the likelihood of droplet separation. The second possible event timing is at 710 °CA aTDCf. At this time, the liquid film model predicts an upwards creeping motion of the fluid inside the piston crevice resulting from inertia forces. This phenomenon is also reported by optical observations of non-fired engines and detailed simulations of the piston crevice volume [33, 34, 35, 36]. Figure 7.7 (**a**) shows the droplet release strategy for both simulation cases.

After the initialization of the oil droplets, the thermodynamic history is recorded in the vicinity of the droplet during the compression stroke. The vicinity of the droplet is defined as the volume inside a 1 mm radius around the droplet location. Inside this volume, the discrete data of all selected cells and vertices are saved. The previously discussed droplet modeling approach showed that ignitions are located within a 1 mm radial distance from the droplet surface in a quiescent ambient. Turbulent mixing and convective transport enhance the homogenization process in the droplet surrounding and may shift critical conditions towards the drop surface. Therefore, the maximum oil mass fraction and gas temperature are extracted from the saved data representing the statistical “worst-case” scenario.

Figure 7.7 (b-d) shows the results achieved using the boundary conditions of OP 1. This operation point showed the highest LSPI frequency and is therefore taken as a reference case for this investigation.

Release timing: 630 °CA aTDCf

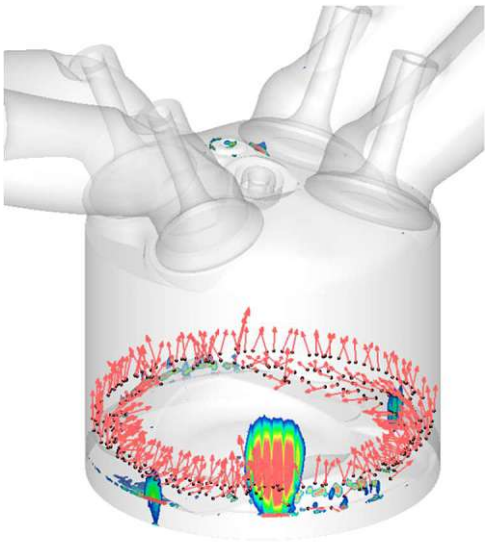

Release timing: 710 °CA aTDCf

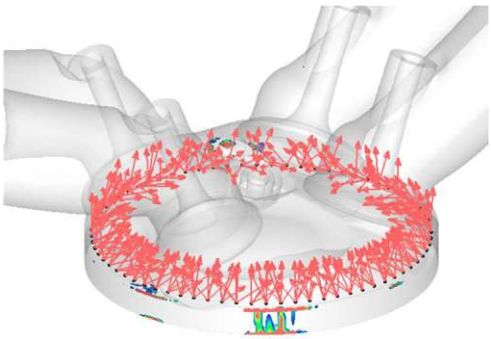

(**a**) Oil droplet release strategy

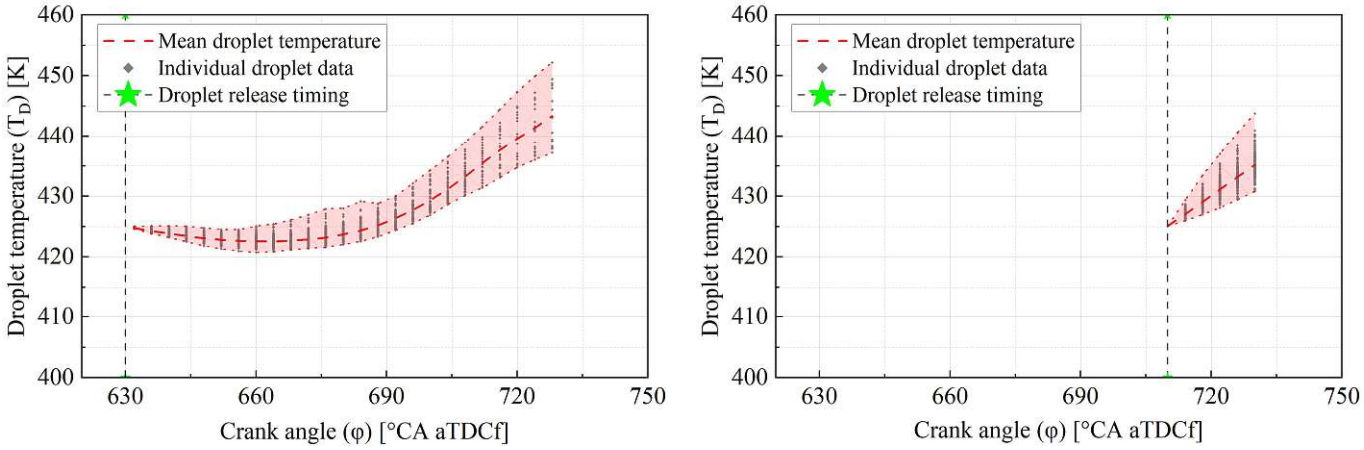

(**b**) Temporal evolution of the oil droplet temperature

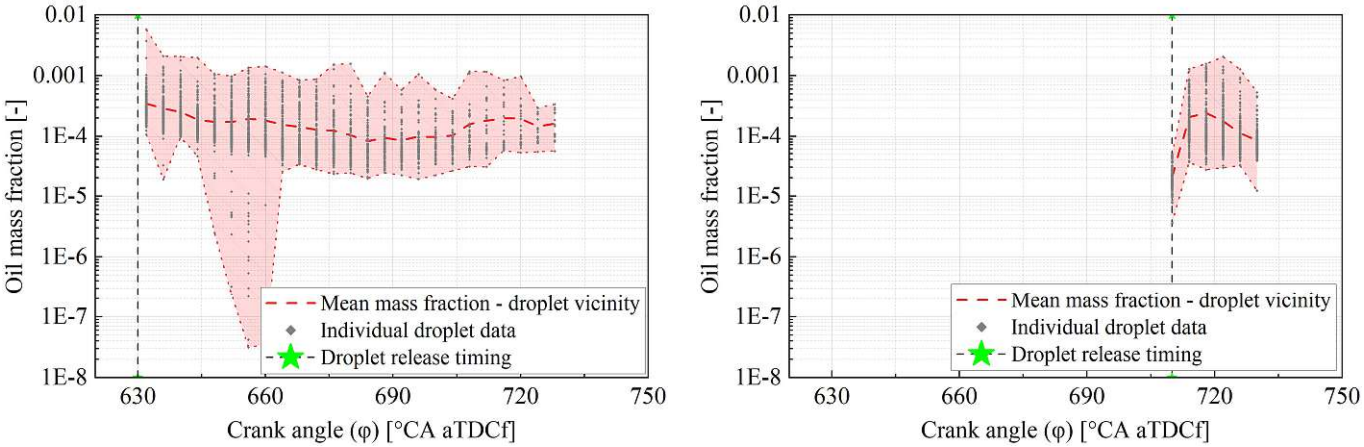

(**c**) Oil droplet vicinity – oil mass fraction

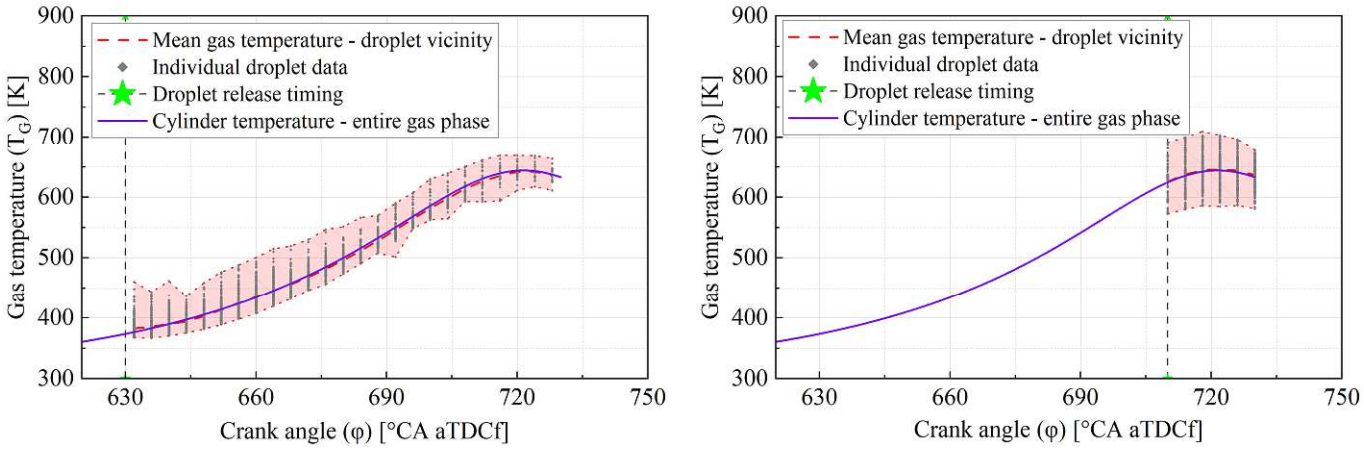

(**d**) Oil droplet vicinity – gas temperature

Figure 7.7: Oil droplet release and the temporal evolution of the thermodynamic conditions.

In the case of the early release timing (630 °CA aTDCf), the temporal evolution of the mean droplet temperature level remained almost constant during the initial 60 °CA. This effect is the result of the relatively cold ambient compared to the initial drop temperature. Due to the continuous compression,

the charge temperature surpasses 425 K at ~660 °CA aTDCf. After that timing, the oil droplets' temperature slowly starts to increase, resulting in 440 K at TDC, representing a mean net increase of 15 K compared to the initial temperature. With respect to the late release case (710 °CA aTDCf), the mean oil droplet temperature immediately starts to rise since the ambient gas phase is already hotter than the droplets. Due to the short time span to TDC, the average oil droplet temperature of 431 K falls below the early release case. The low saturation pressure of long-chained hydrocarbons leads to very low evaporation mass flow rates and thus only a minor droplet cooling effect compared with the apparent convective heat transfer. This result indicates that the most critical release timing is a trade-off between the initial oil droplet temperature and the gas phase temperature. By neglecting the heat of evaporation, the timing is located at ~660 °CA aTDCf where the initial oil droplet temperature matches the ambient gas phase. Nevertheless, only minor increases in droplet temperature can be observed during the compression stroke compared with the statistical scatter band of the individual droplets. Consequently, the evaporation rate is mainly determined by the lubricating oil temperature level of the specific engine configuration and the state of homogenization and thus the presence of hot spots.

At the droplet temperature level at hand, a maximum oil mass fraction of ~0.2 % can be observed during the compression stroke for both simulated droplet release cases. Furthermore, it can be observed that the average mass fraction level remains almost constant in the early release case. Due to the relative droplet velocity, the convective species transport prevents accumulations in the droplet vicinity. This effect is continuously reduced towards TDC, resulting from the dissipating momentum in the gas phase.

The observable gas temperature bandwidth of ~100 K at TDC matches the overall gas phase condition shown in Figure 6.16 (**a**) of section 6.3. Furthermore, the overall mean in-cylinder gas-phase temperature matches the mean gas temperature in the droplet vicinity highlighting the insignificant cooling effect due to droplet evaporation as well as the sufficient statistical droplet sample size. However, it has to be mentioned that the initial sample size drops during the simulation due to droplet / wall interactions, especially in the early droplet release timing simulation case. Therefore, a slightly reduced statistical representation quality can be expected in this case.

Based on the achieved results, the boundary conditions in the vicinity of the oil droplet are insufficient to trigger LSPI under the investigated boundary conditions. With respect to the results of the homogeneous reactor, a gas temperature level of ~820 K has to be surpassed to trigger autoignition within ~20 °CA at the observed oil mass fractions. The low volatility of lubricating oil inhibits high oil mass fractions resulting in insufficient ignition delay times.

7.3. Robustness of results concerning oil composition and reaction kinetic speed

A possible source of uncertainty in the shown calculations stems from the assumption that the detached oil droplet is chemically treated as n-heptane. Repetitive heat cycles of the liquid oil inside the combustion chamber may enable accumulations of semi-stable intermediate species enhancing the overall reactivity. Experiments investigating the accumulation of intermediate species in the gas phase due to repetitive compressions and expansions are performed by Blin-Simiand [49]. The author used a CFR engine operating close to autoignition but without combustion. A significantly enhanced autoignition tendency could be observed when this pre-oxidized fuel-air mixture is used as a fuel additive. Magar [143] and Heiß [31] confirmed this observation by detailed chemical kinetic simulations. The analysis revealed an increased content of ketohydroperoxide species. This specific group of semi-

stable species is reported to be highly reactive, even in low quantities. They are formed through the low-temperature oxidation pathway and act as a "bottleneck" for further oxidation. Consequently, the accumulation of this semi-stable species reduces the induction time up to the "cool flame" event initiated by their decomposition.

In order to investigate the influence of pre-oxidized species, n-heptane resulting from evaporated oil is replaced by C7-ketohydroperoxide ($C_7H_{14}O_3$) representing a highly reactive intermediate. Figure 7.8 shows the achieved ignition delays using 50 bar constant ambient pressure and an oil mass fraction of 0.2 %, representing the maximum observed oil mass fraction during the droplet release simulation. Additionally, an elevated mass fraction of 1 % is shown to cover uncertainties concerning determined oil mass fractions.

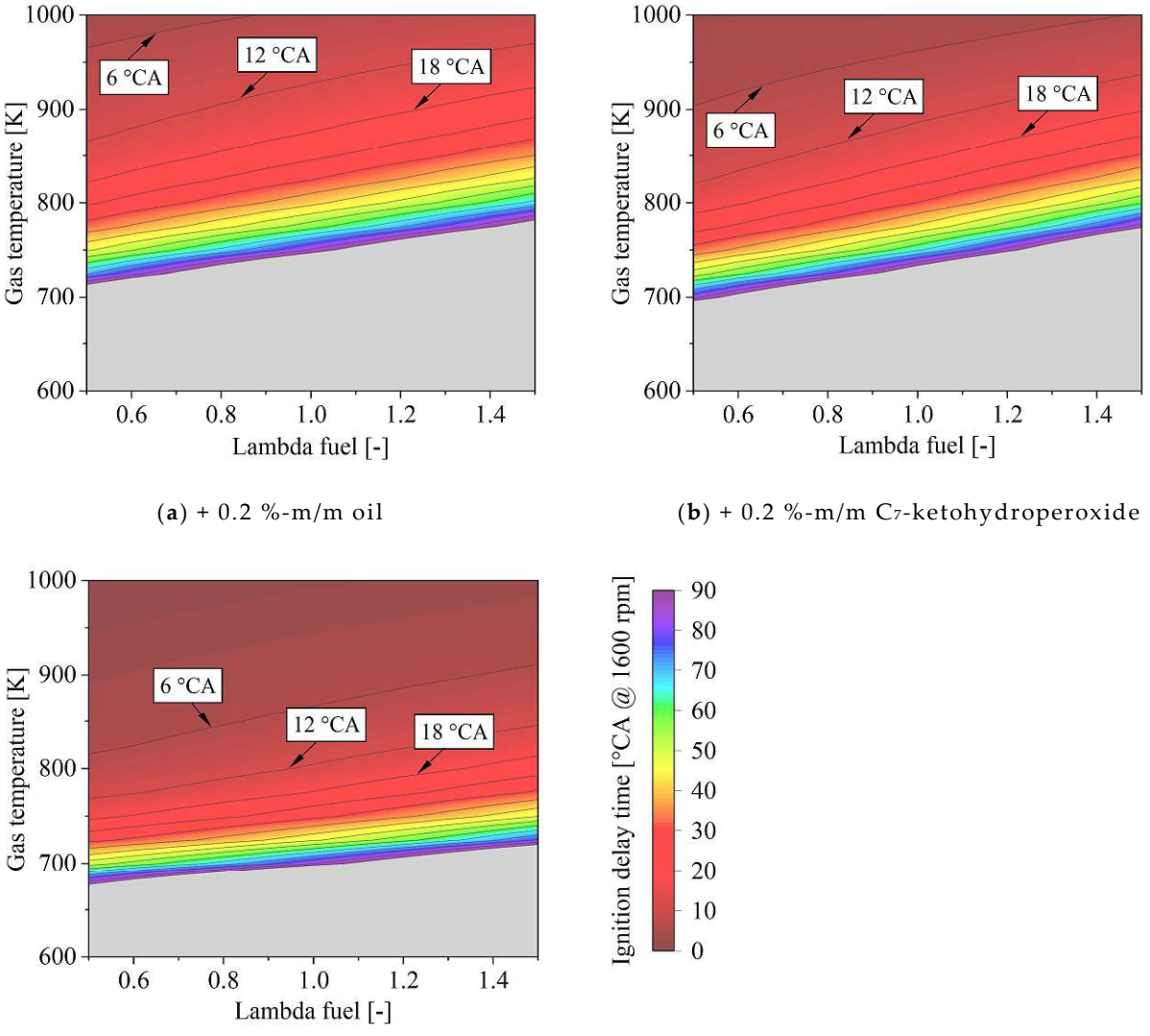

(**a**) + 0.2 %-m/m oil

(**b**) + 0.2 %-m/m C7-ketohydroperoxide

(**c**) + 1.0 %-m/m C7-ketohydroperoxide

Figure 7.8: Influence of semi-stable intermediates (C7-ketohydroperoxide) on the ignition delay time.

The investigation reveals a significant reduction in the calculated ignition delay time, especially for temperatures below 750 K. However, even when the acceleration by the presence of pre-oxidized

species is considered, ignition delay times are too long to explain LSPI in the investigated engine configuration and load point. The maximal observed gas temperatures of 710 K at TDC result in a predicted ignition delay of 70 ~ 350 °CA @ 1600 rpm, dependent on the ambient air-fuel ratio. Furthermore, the consideration of elevated mass fractions up to 1 % would not lead to an LSPI event. At such concentrations, the observed ignition delays are reduced to 45 ~ 130 °CA @ 1600 rpm, though insufficient.

Therefore, a neat hydrocarbon-based droplet-induced LSPI initiation cannot be supported by the performed numerical studies at the investigated load point in the used engine configuration. Nevertheless, the results cannot exclude droplet-induced LSPIs for all engine configurations and load points. However, it has to be mentioned that the results suggest fairly high gas temperature levels above 750 ~ 800 K to initiate a premature ignition successfully. Therefore, this phenomenon can be considered very improbable, especially in series application engine configurations.

8. Analysis of hot particle-induced ignitions

8.1. Mechanism of hot particle-induced LSPI and modeling overview

Besides oil-fuel droplets, detached particles are assumed to be a potential root cause of LSPIs. Particles inside the combustion chamber are typically the result of sub-stoichiometric combustions of fuel and oil. Therefore, the creation of such deposits is promoted by fuel puddles inside the combustion chamber shown in section 6. Whereas oil droplets accelerate ignition processes by evaporating reactive species, particles induce an ignition by heat transfer. If a particle reaches a sufficient surface temperature, the accelerated chemical kinetics of the ambient lead to an ignition very close to the hot surface.

In order to determine the gas-phase ignition potential caused by a hot particle inside the combustion chamber, the accurate prediction of the introduced steep temperature gradient extending outwards from the hot surface into the reactive ambient is crucial. Therefore, a highly resolved CFD sub-model is established to capture this effect. The analysis on a microscale level enables the generation of an ignition delay map by varying thermodynamic conditions. Furthermore, the investigation provides further insight into the sensitivity of each parameter with respect to the ignition delay. In the next step, the established map is then combined with an ignition integral approach to transfer the static simulation results to transient boundary conditions.

8.2. Generation of an ignition delay map

Regardless of the unknown history of detached particles inside the combustion chamber as well as their potential exothermal reactivity, hot objects induce an ignition by heat transfer. Therefore, the solid particles are simplified as a spherical hot surface in the simulation model. A minimum cell size of 1 µm accompanied by a radial stretching factor of 1.01 ensures a sufficiently high resolution of the thermal boundary layer. [144, 145] The instantaneous wall heat flux can be defined according to equation (8.1)

$$\dot{Q}_{wall} = -k_G * \left(\frac{dT_G}{dy}\right)_{wall} \tag{8.1}$$

In this equation, y represents the wall-normal direction, T_G is the gas mixture temperature, and k_G is the thermal conductivity of the gaseous phase.

For the sake of reducing the overall computational effort, the simulation task is solved on a structured cylindrical 2D 90° sector mesh. The simulation domain is enlarged to 25 times the particle radius to minimize the influence of boundary conditions. The chemical kinetics are implemented according to the established models in section 7.2. to ensure identic numerical settings.

In order to determine the ignition delay time, a consistent ignition criterion is needed. If an established propagating flame front reached a critical radius of 0.5 mm, the flame was assumed to be self-sustaining. Numerically, this criterion is checked by observing the maximum gas temperature trace in all cells at a radius of 0.5 mm. The simulation time at the highest observed gradient is defined as ignition delay time ($t_{ign} = t(\frac{dT_{G,max}}{dt})_{max}$). The critical radius was set according to Kalghatgi [146], who published the critical radius for n-heptane / air mixtures under similar conditions.

To determine the hot particle-induced ignitability under in-cylinder relevant conditions, a set of pre-calculated cases are used to set up a 4D ignition delay look-up table. The thermodynamic conditions of the ambient fuel-air mixture (T_G, λ, and p_G) are varied based on the results achieved in the mixture preparation and liquid film formation analysis performed in section 6. In contrast to the expectable range of parameters considering the ambient gas phase, the particle temperatures are fairly unknown. Optical investigations suggest a particle temperature well above 800 K. Therefore, seven fixed particle temperatures ranging from 1000 K to 2000 K are used to create an extensive data base. In order to reduce the number of necessary simulations, the particle diameter is set to 250 µm in line with the droplet-induced ignition analysis. The geometrical influence of the diameter on the ignition delay is considered via a correction function discussed in the next section. The same concept is used to account for convective transport due to relative particle velocity.

Nevertheless, more than 360 CFD simulations are conducted and post-processed to investigate the influence of mixture properties on the ignition delay time. Table 8.1 summarizes the investigated parameters of the DoE simulation setup. Additionally, Figure 8.1 shows a particle and gas temperature sweep at 10 bar and 50 bar gas pressure at a lambda value of 0.8. All simulation results are listed in the Appendix section A-1.4.

Table 8.1: DoE parameter setup.

Parameter	# Variations	Used values
Gas temperature (T_G)	4	500 K, 575 K, 650 K, 725 K
Gas pressure (p_G)	3	10 bar, 30 bar, 50 bar
Lambda—TRF (λ_{TRF})	4	0.5, 0.8, 1.0, 1.2
Particle Temperature (T_P)	7	1000 K, 1200 K, 1300 K, 1400 K, 1500 K, 1600 K, 2000 K

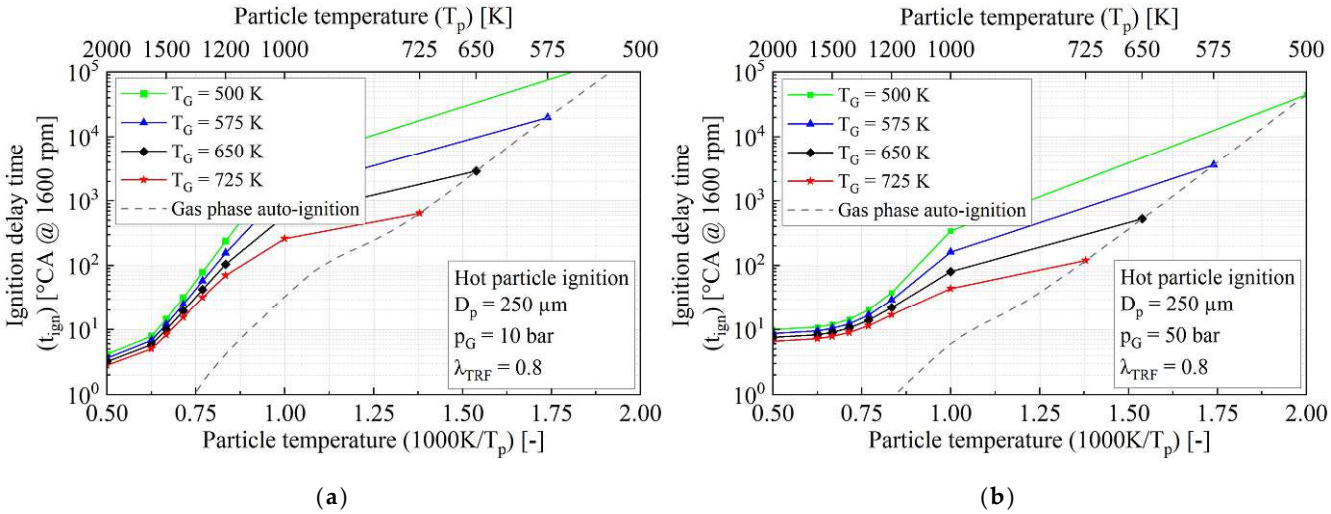

Figure 8.1: Particle and gas temperature sweep at a lambda value of 0.8: (**a**) 10 bar gas pressure, (**b**) 50 bar gas pressure.

It can be observed that the ignition delay time converges towards 3~10 °CA for particles hotter than 1500 K. At this temperature, the used chemical reaction mechanism predicts an immediate ignition in

the numerical cell next to the particle surface. Therefore, the results achieved are primarily reflecting the influence of the thermodynamic conditions on flame propagation.

In the case of particle temperatures below that threshold, the particle heats up the ambient gas phase, and as a result, increases the chemical reaction speed over time. Although the build-up of a radical pool close to the particle surface is decelerated due to diffusive transport compared to a homogeneous reactor case, the influence of the particle temperature on the ignition delay time can be described by an exponential law ($R^2 > 0.95$; Figure 8.2 (**a**)). The slight deviation in regression reflects the minor influence of the diffusive transport on the ignition delay.

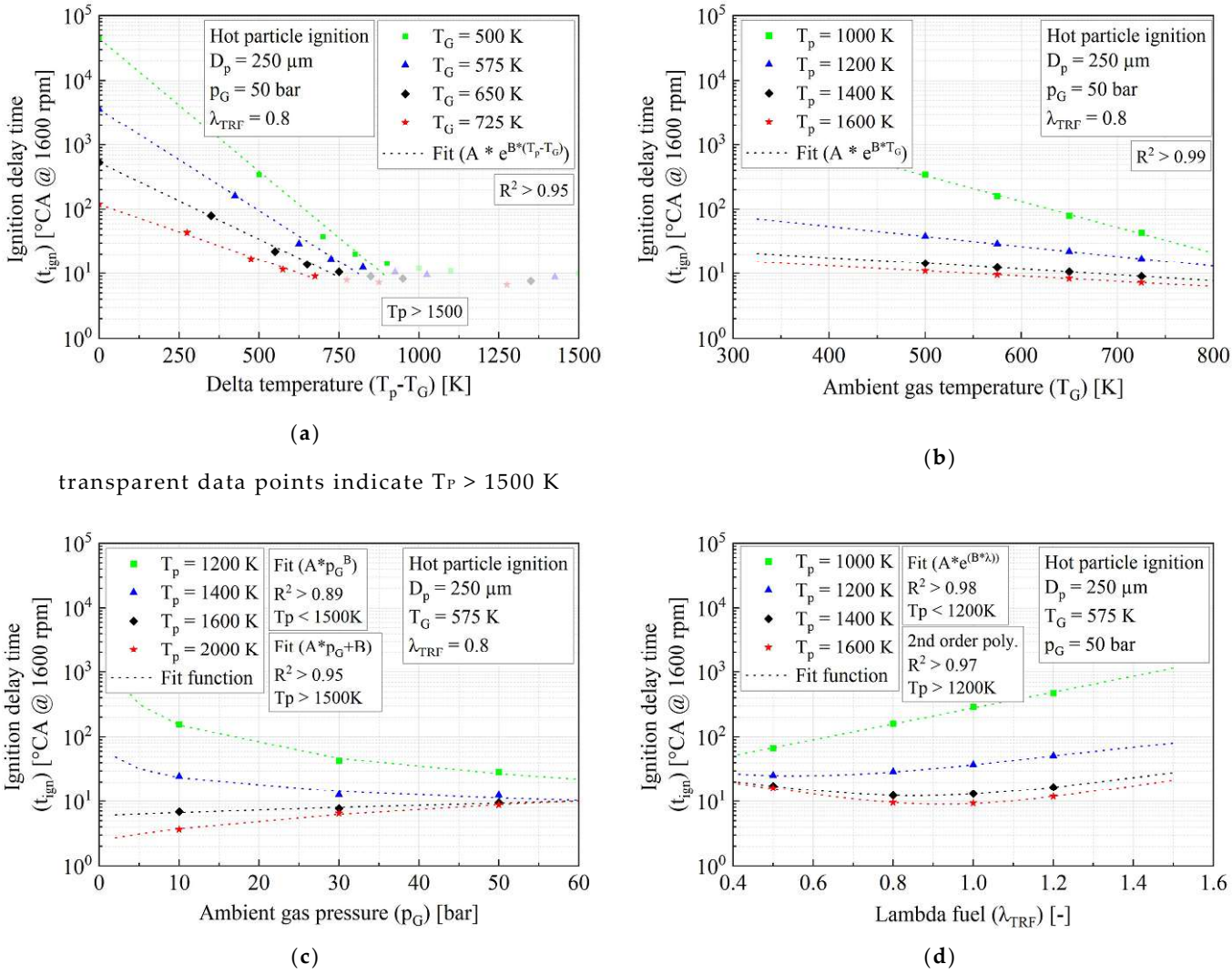

Figure 8.2: Characteristic dependencies for (**a**) particle temperature, (**b**) gas temperature, (**c**) gas pressure, (**d**) air-fuel ratio.

The initial gas temperature dictates the overall reaction/autoignition speed of the ambient far-field. Considering the extended Arrhenius approach used to calculate the kinetic speeds of each chemical reaction, it is not surprising that the effect of the initial gas temperature on the ignition delay time follows an exponential law ($R^2 > 0.99$; Figure 8.2 (**b**)). Furthermore, high gas temperature levels reduce

the temperature gradient to the particle surface, and as a result, decelerates the diffusive "loss" of radicals in the hot zone.

High gas pressure levels increase the concentration of reactants per unit volume, thus enhancing the reaction speed. Typically, the pressure influence in simplified knock/autoignition models is considered by a power-law (p_G^{-B}). The exponent B is reported to be 1.685 for commercial gasoline fuel by Douaud [147] and Rifkin [148]. A power-law characteristic can still be found in the investigated cases with reasonable accuracy ($R^2 > 0.91$; Figure 8.2 (**c**)). However, the reported B is measured under homogeneous conditions and is only valid for the setup mentioned in the literature. In this study, exponent B is continuously dropping with increasing temperature levels. Especially, high ΔT-cases ($=T_P - T_G$) showed a significant reduction of the power-law characteristic (B = ~0.4) and finally inverses in cases using particle temperatures above the discussed critical threshold of 1500 K. The change in the found characteristic expresses the transition towards a flame propagation problem. In contrast to the gas-phase ignition delay time, the flame propagation speed decreases with increased pressure levels.

A similar trend can be found when considering the air-fuel ratio. Lowering the lambda value leads to an increase of reactants while simultaneously reducing inert species (N_2) and thus the diluting effects. As a result, an exponential decrease in the calculated ignition delay time can be observed ($R^2 > 0.98$; Figure 8.2 (**d**)). The exponential character changes to a second-order polynomial character at high particle temperature levels within the investigated range of air-fuel ratios, emphasizing the transition to a flame propagation-dominated problem. Consequently, the minimum ignition delay times are predicted at λ ~0.9, where the flame speed reaches its maximum.

Effect of particle diameter

The discussed 4D ignition delay map is generated using a particle diameter of 250 µm. In order to account for varying particle diameters, the simulations are performed using seven discrete diameters ranging from 50 µm to 500 µm at mean TDC conditions (T_G = 650 K, p_G = 50 bar, λ = 0.8). The particle diameter influences the effective area of heat transfer and thus the heating power. The results of the performed diameter sweep are shown in Figure 8.3. The y-axis displays the normalized ignition delay with respect to the baseline diameter of 250 µm.

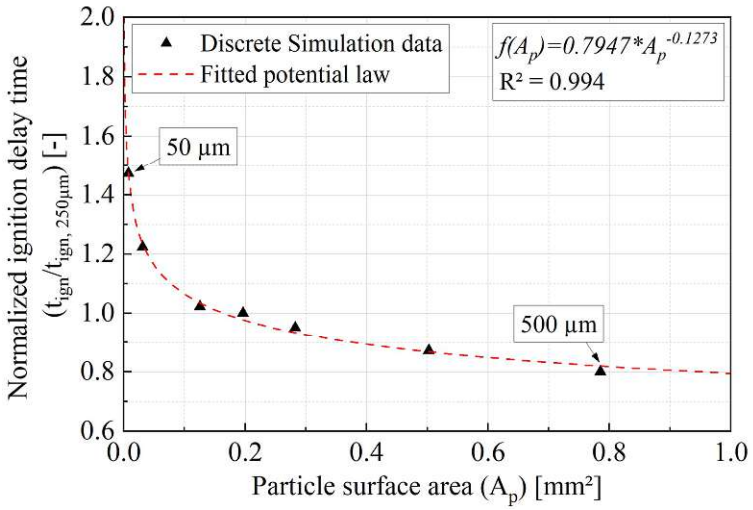

Figure 8.3: Sensitivity of the particle diameter on the ignition delay.

The achieved results show a power-law character following the radius-dependent surface gain. As a result, small particles are suffering from very long ignition delay times, whereas large particles increase the ignition probability.

Despite the change in the gas-phase conductivity, an insignificant influence of the ambient conditions on the achieved normalized results are expected. Therefore, the fitted power-law function is used to correct the predicted ignition delay of the look-up table using the fitted function shown in Figure 8.3.

Effect of convective transport

The flow past a sphere is a well-studied problem in the literature. Depending on the present Reynolds number, different flow structures can be observed especially in the wake of the particle. A schematic illustration of the flow field past a sphere is shown in Figure 8.4.

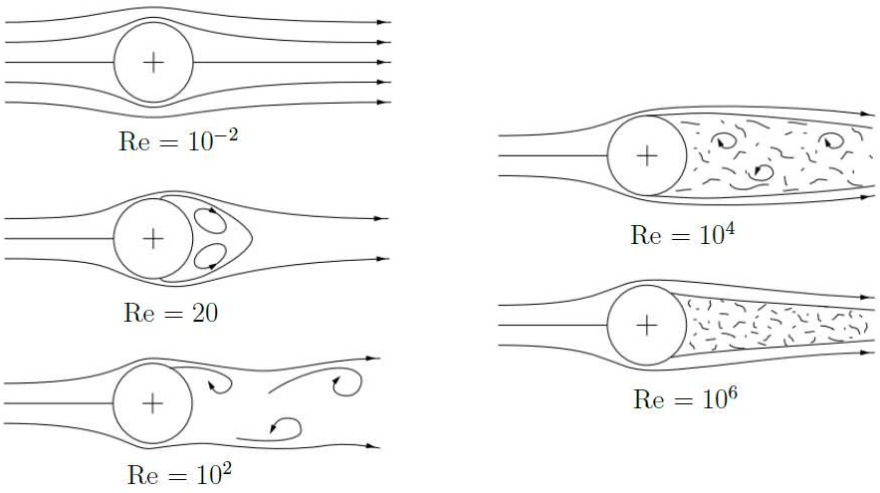

Figure 8.4: Characteristic wake flow field depending on the Reynolds number [75].

At very low relative velocities and thus Reynolds numbers, the flow remains laminar and follows the contour of the particle curvature. A characteristic low-pressure zone establishes with increasing velocity, reversing the flow direction behind the spherical object. Additionally, high velocity gradients induced by the viscous wall boundary layer result in the generation of two count-turning vortices leading to the characteristic low-speed wake. At Reynolds numbers ranging from 10^2 to 10^3, the momentum dissipating count-turning vortices become unstable and start to separate from the particle surface. The unstable flow conditions lead to a periodic build-up and detachment of vortices generating the "Karman vortex street". The unsteady flow separation can be characterized by the Strouhal number determined by the frequency of vortex detachment, typically ranging from 0.1 to 0.3 under atmospheric conditions. [149, 150, 151, 152]

Up to this point, the flow field is still considered laminar since all observable flow field structures are periodically unsteady and not chaotic in nature. When the relative velocity is further increased, 3D chaotic, turbulent structures occur. Such chaotic structures are unstable and collapse into smaller vortices where the flow is once more viscous dominated. At such length scales, also known as "Kolmogorov scales", the momentum of the vortex is dissipated. According to Tennekes [153] and Pope [154], the length scale can be approximated via equation 8.2.

$$L_{Kolmogorov} = \frac{D_p}{Re^{3/4}} \tag{8.2}$$

In order to determine the influence of convective species transport on the resulting ignition delay, the numerical grid used to generate the 4D ignition delay map is adapted to enable the simulation of relative particle velocity. Therefore, the 90° sector is extended to an entire rectangular plane of 6.25 mm (50 x R_P) x 13.25 mm (106 x R_P). The relative velocity is simulated via a velocity inlet boundary condition in front of the solid geometry enabling the use of a static numeric grid. The flow field in the simulation domain is initialized homogeneously to the desired relative velocity. All other environmental boundary conditions are implemented as static pressure inlet/outlet, ensuring a constant pressure level inside the domain. In terms of thermodynamic and mixture properties of the gas phase, the investigation is confined to mean TDC conditions (p_G = 50 bar, T_G = 650 K, λ_{TRF} = 0.8). The grid resolution is further refined to account for high velocity gradients near the particle surface and small-scale vortex structures in the wake. Therefore, the cell size on the particle surface is set to 0.3 µm and increases outwards using a stretching factor of 1.01.

In order to reduce the overall cell count, the simulation model is limited to non-turbulent cases. Since no turbulence models are used, the mesh resolution would need to match the Kolomogorov length scale requirement on the entire simulation domain. Nevertheless, the selected cell size fulfills the requirement in the vicinity of the particle up to a Reynolds number of 1500, resulting in ~8 m/s considering the gas phase properties at mean TDC conditions and a particle diameter of 250 µm. The mesh resolution is chosen based on the achieved data during the oil droplet release simulations of section 7, showing that the expected Reynolds numbers fall below 1500 during the compression stroke. Figure 8.5 gives an overview of the simulation domain and the mesh discretization.

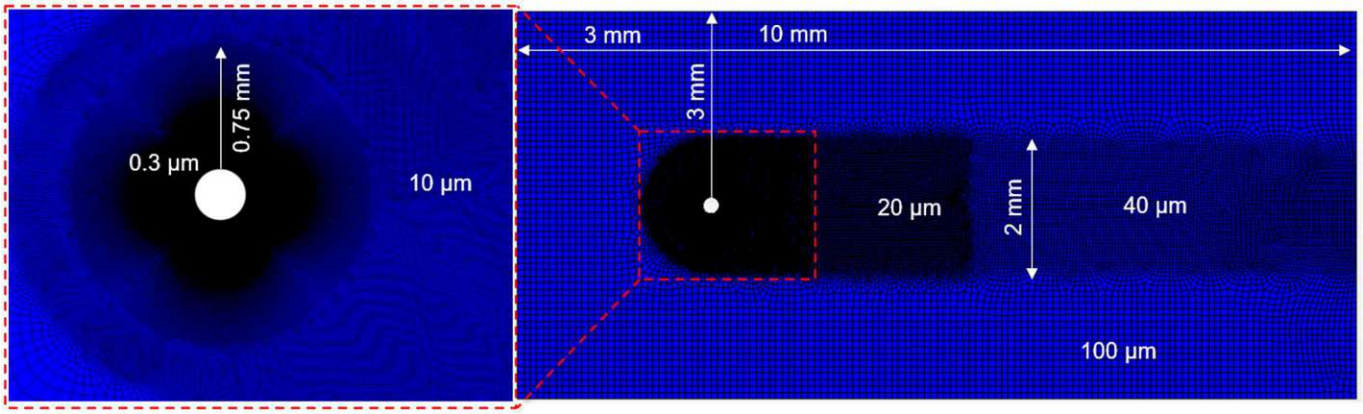

Figure 8.5: Simulation domain and grid resolution.

In order to investigate the influence of convective transport on the accumulation of reactive species, a relative velocity sweep is performed. Therefore, the gas-phase velocity is increased stepwise until the ignition is effectively suppressed. Furthermore, the influence of the particle temperature and thus the induced reaction kinetic speed in the vicinity of the hot surface is investigated using particle temperatures ranging from 1100 K to 1400 K. Figure 8.6 (**a**) shows the predicted ignition delay results normalized by the equivalent quiescent simulation case. Figure 8.6 (**b**) summarizes the observed ignition thresholds concerning the relative particle velocity.

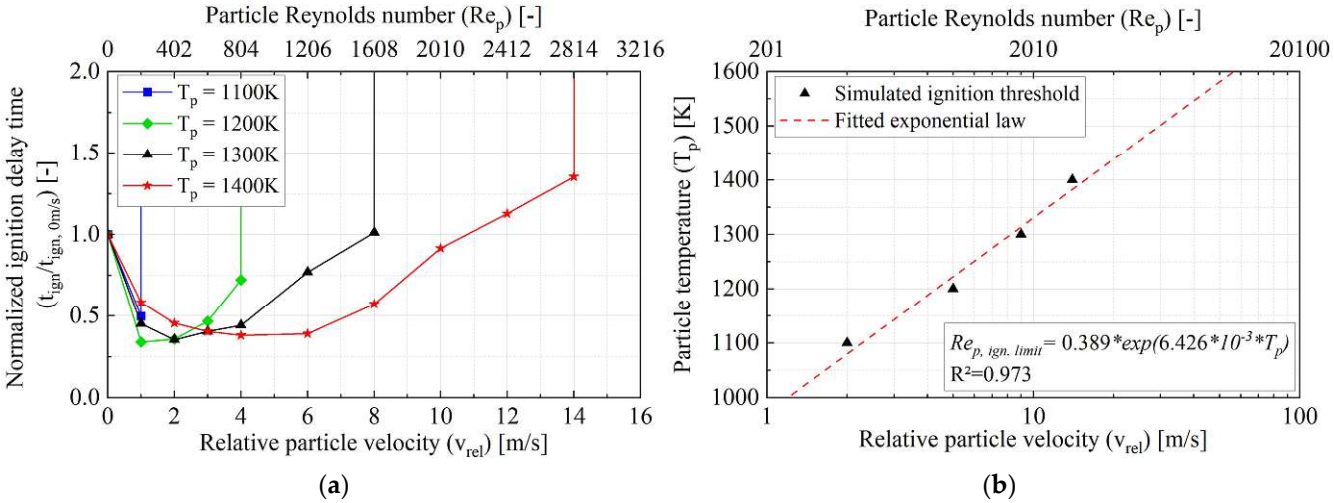

Figure 8.6: Influence of Reynolds number and particle temperature on predicted ignition delays. (**a**) Simulation results of a particle temperature and relative velocity sweep, (**b**) derived ignition limit function.

The results reveal a significant drop in ignition delay time for low Reynolds numbers. Independently of the particle temperature, the time to ignition is reduced up to ~65 % compared to a quiescent ambient. At such conditions, the growth rate of the two count-turning vortices is slow compared to the reaction kinetic speed. The characteristic flow field around the particle transports heated ambient gas towards the flow separation point on the particle surface, illustrated in Figure 8.7. This concentrates the hot air-fuel mixture in an almost triangular cross-section. The reduced surface-to-volume ratio accompanied by a low gas velocity effectively reduces heat loss. Consequently, the ignition is located at the flow separation area close to the hot surface.

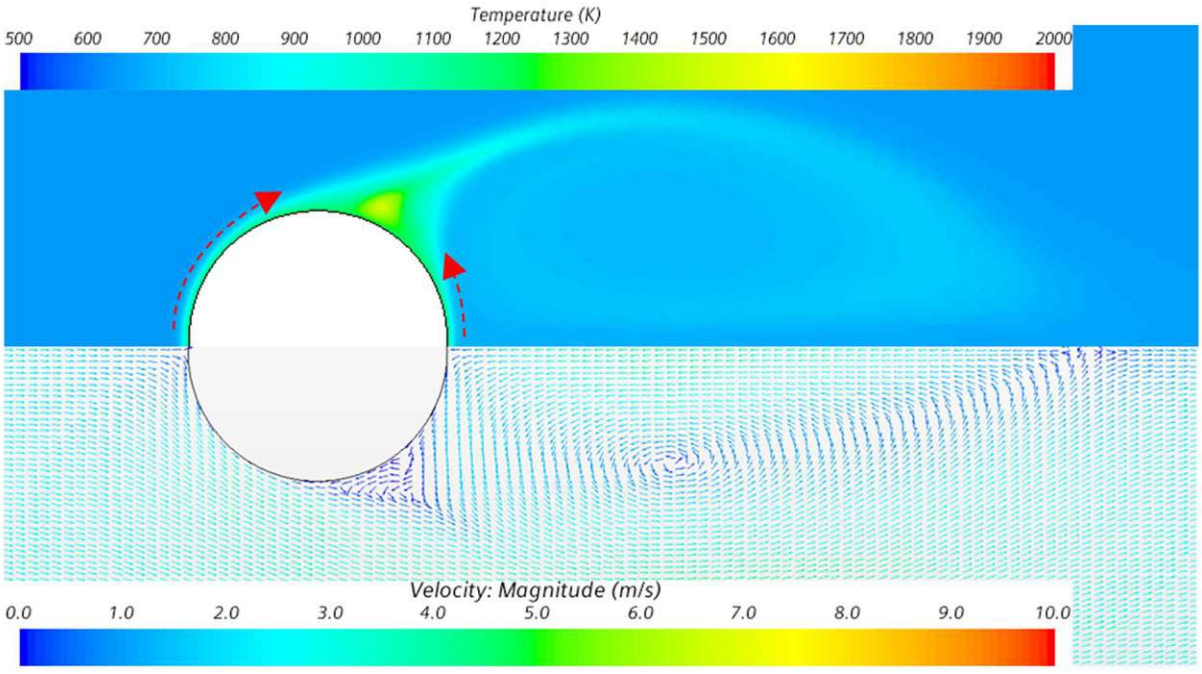

Figure 8.7: Ignition accelerating effect of low a Reynolds flow pattern. Illustrated simulation case: T_P = 1200, gas velocity = 3 m/s (Re_P = 603).

It can be observed that the sweet spot of minimal predicted ignition delay times is dependent on the particle temperature. Hot particle temperatures shift this point to higher Reynolds numbers. This phenomenon expresses the trade-off between transporting hot gases towards the separation point and the increased heat loss. The shorter overall time span to ignition requires a faster convective transport of the heated near surface gases to build up the triangular zone, finally accelerating chemical kinetics.

By further increasing the ambient gas velocity, the enhanced heat and species transfer reduce the accelerating effect. Additionally, the accelerated growth rate of the count-turning vortices leads to a faster transition into a periodic vortex detachment pattern. At that point, the created radical pool inside the hot reaction zone is periodically diluted by cold ambient gases. This effect is further supported by the creation of two smaller vortices near the surface, enhancing gas mixing. The location of these small-scale structures is determined by the more prominent detaching vortices resulting in a periodic shift along the circumference of the sphere. However, the relative angular location to each other remains almost constant, as shown in Figure 8.8.

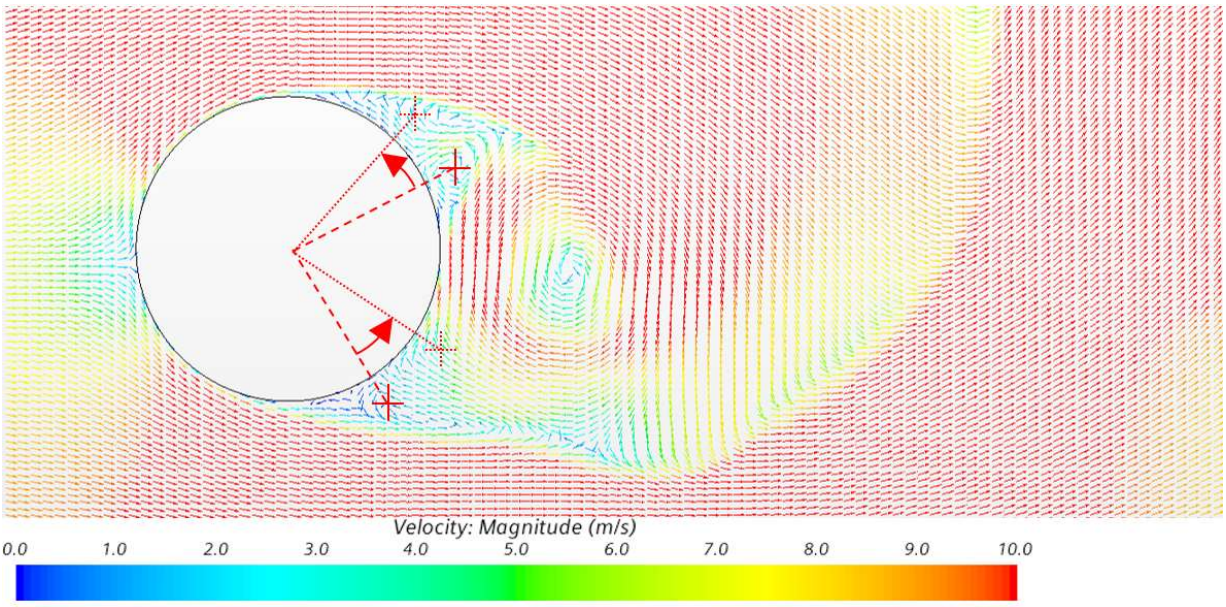

Figure 8.8: Periodic shifting of near particle vortices. Illustrated simulation case: T_P = 1300, gas velocity = 10 m/s (Re_P = 2010).

No ignitions are predicted after establishing this flow regime. The pronounced cooling and diluting effect of the described flow pattern effectively suppresses accumulations near the hot surface. The minor heating effect of the gas downstream is insufficient to trigger an ignition within the simulation domain. This coincides with the performed optical investigations observing ignitions and flame propagations only at glowing objects.

The assumption of a constant flow direction may not represent in-cylinder conditions. Although a superordinate tumble structure can be found, the turbulent flow field may lead to a continuously changing flow direction in the vicinity of the particle. Therefore, the observed low-Reynolds accelerating effect of concentrated hot zones may be distorted. Consequently, this effect is not considered in the 4D ignition delay map. However, the suppression of ignition at increased velocities remains valid. Chaotic structures may enhance this effect by turbulent mixing. Therefore, the observed "blow-out" conditions are implemented, representing worst-case conditions. The threshold velocities

are inter- and extrapolated using a fitted exponential law, shown in Figure 8.6 (**b**). The good correlation of the data points highlights the link to chemical speed determined by the Arrhenius equation. The ignition delays of quiescent ambient conditions are used up to this velocity threshold.

8.3. Application to transient boundary conditions

In order to use the generated 4D ignition delay map under transient boundary conditions, an ignition integral approach is introduced in analogy to the proposed method of Livengood and Wu [155]. The integral calculates the consumption of ignition delay time under the current thermodynamic conditions, including the present flow field and particle diameter, shown in equation 8.3.

$$\tau_{ign} = \sum_{i=1}^{N} \left(\frac{\Delta t_{TS,i}}{\tau_{ign,i}\,(T_p, T_G, p_G, \lambda, D_p, v_{rel})} \right) \tag{8.3}$$

The methodology is applied in a first step to mean in-cylinder conditions achieved in OP 1 of section 6 to determine the ignitability potential of hot particles. The exported data of the CFD model is summarized in Figure 8.9 (**a**). The calculation of the ignition integral starts at IVC (565 °CA aTDCf) and ends at spark timing (724 °CA aTDCf). The analysis is performed assuming that the relative velocity is lower than the "blow-out" threshold throughout the entire compression stroke. This approach allows for an isolated analysis of the influencing thermodynamic parameters. Considering the in-cylinder data obtained from the CFD model, it can be assumed that the thermodynamic condition during the gas exchange is not prone to premature ignitions. Furthermore, no LSPI event could be detected in the experiments during the gas exchange process highlighting the validity of this assumption. Therefore, this time period is neglected in the simulations. Figure 8.9 (**b**) shows the temporal evolution of the results achieved using constant particle temperatures ranging from 800 K to 1400 K.

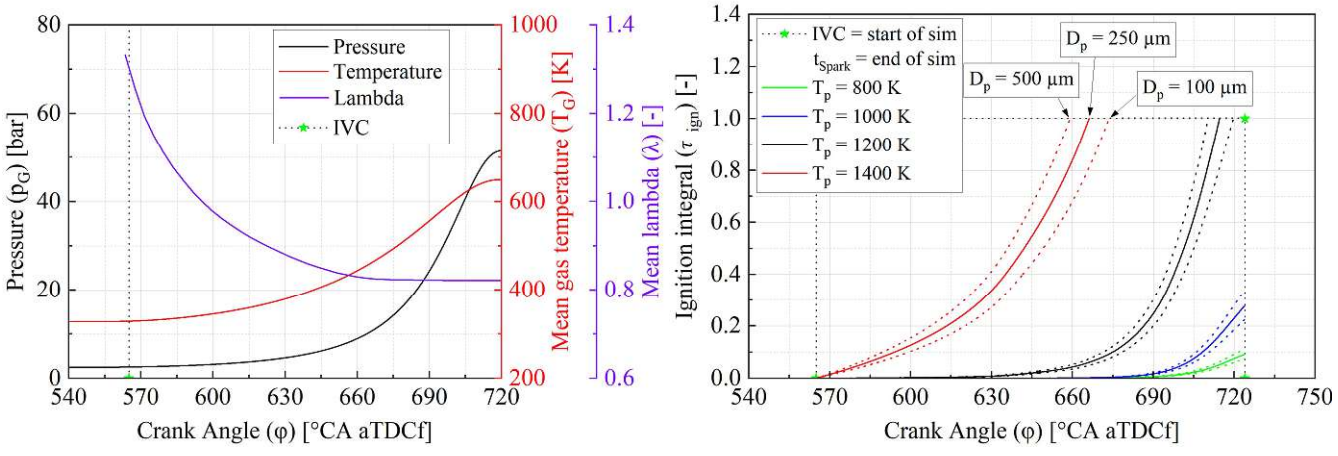

(**a**) (**b**)

Figure 8.9: (**a**) Mean thermodynamic conditions inside the combustion chamber, (**b**) Temporal evolution of the ignition integral for particle temperature ranging from 800 K to 1400 K and diameters ranging from 100 µm to 500 µm.

It can be observed that the ignition integral barely increases before 660 °CA. Prior to this crank angle, the reactivity of the gas phase is low due to the low pressure (< 10 bar) and gas temperature (< 450 K) levels. Only very hot particles ($T_P \geq 1400$ K) can consume a significant amount of the ignition delay in the early compression phase. This reflects the decreasing sensitivity of the thermodynamic boundary conditions of very hot particles. The influence of the particle diameter is small compared to the particle temperature. With respect to a constant particle temperature of 1200 K, the increase from 100 µm to 500 µm in diameter results in a 9.3 °CA earlier predicted ignition.

By iterating the particle temperature, a minimum critical value of 1167 K can be found for a particle diameter of 250 µm. At this temperature, the particle is predicted to induce an ignition at spark timing and therefore represents the absolute minimum temperature under the investigated conditions.

Since the history of a potential ignition-inducing particle is unknown, it may be detached at some point during the compression phase and lead to ignition in the same cycle. Furthermore, reported pre-ignitions were observed well before spark timing. Therefore, the start and end of the simulation were varied to investigate the sensitivity of the particle release and the ignition timing. The results achieved are shown in Figure 8.10.

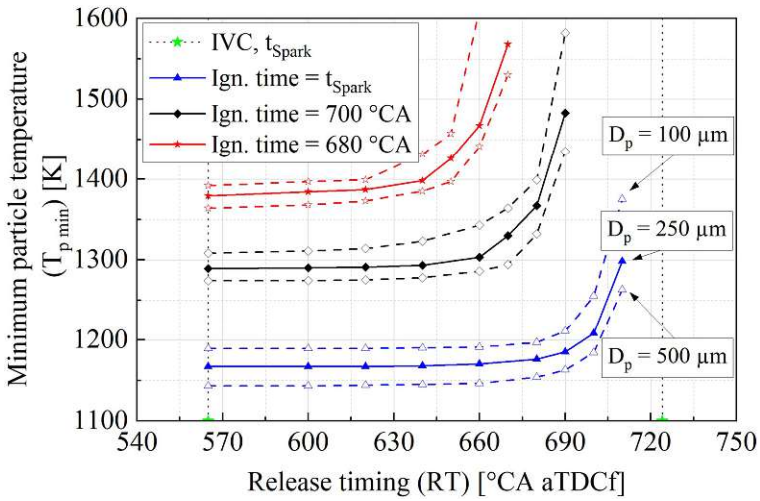

Figure 8.10: Release and ignition timing sensitivity.

The blue line displays the results achieved by delaying the particle's release time while maintaining the desired ignition time at the end of the simulation (spark timing). The corresponding colored dashed lines highlight the influence of the particle diameter on the necessary minimum particle temperature.

The investigation clearly shows the minor impact of the early compression phase. The critical particle temperature increases by only 2~3 K when the release timing shifts from IVC to 660 °CA. On the other hand, an earlier ignition requirement significantly increases the necessary particle temperature. The desired ignition timing of 700 °CA aTDCf results in a temperature demand of at least 1289 K in the case of a 250 µm particle. This matches approximately the temperature requirement of the time period from 710 °CA to 724 °CA aTDCf. Considering the highly non-linear influence of the gas pressure and temperature, the simultaneous increase of these parameters results in a sharp gradient in ambient gas reactivity towards TDC.

Sensitivity of thermodynamic parameters

Since the shown data is generated using the mean in-cylinder conditions under a specific load point, the sensitivity of the thermodynamic boundary conditions is addressed in this section. Therefore, the air-fuel ratio, the initial air temperature as well as the initial gas pressure are varied individually. In contrast, the particle temperature and diameter are set to 1200 K and 250 µm, respectively. With respect to mean engine conditions, the predicted ignition timing is close to TDC at 714.6 °CA aTDCf. In this analysis, the simulation duration is reset to IVC and spark timing. The results achieved are shown in Figures 8.11 to 8.13.

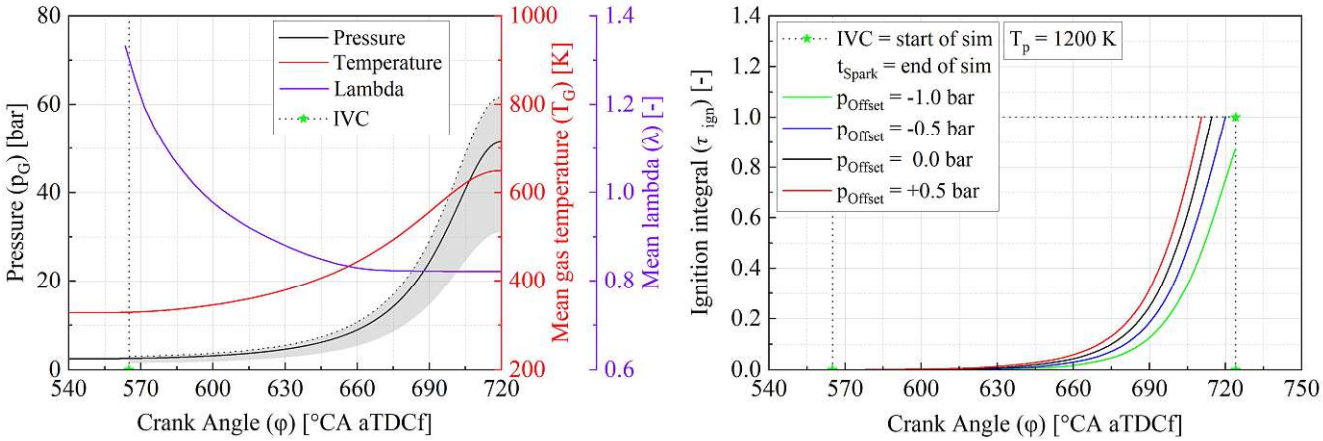

(**a**) (**b**)

Figure 8.11: (**a**) Scatter band of the gas pressure variation, (**b**) sensitivity of the initial boost pressure on the ignition integral.

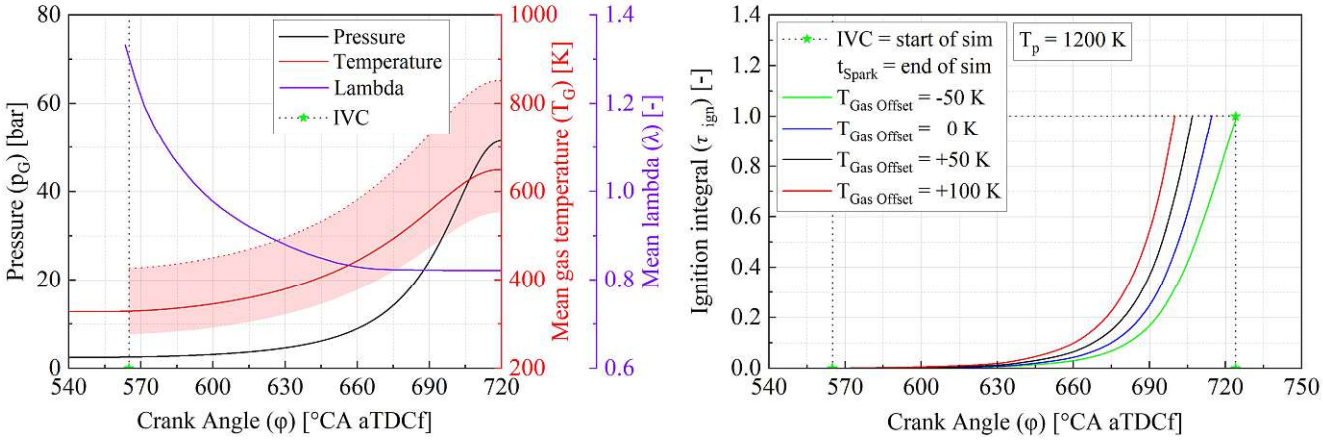

(**a**) (**b**)

Figure 8.12: (**a**) Scatter band of the gas temperature variation, (**b**) Sensitivity of the initial gas temperature on the ignition integral.

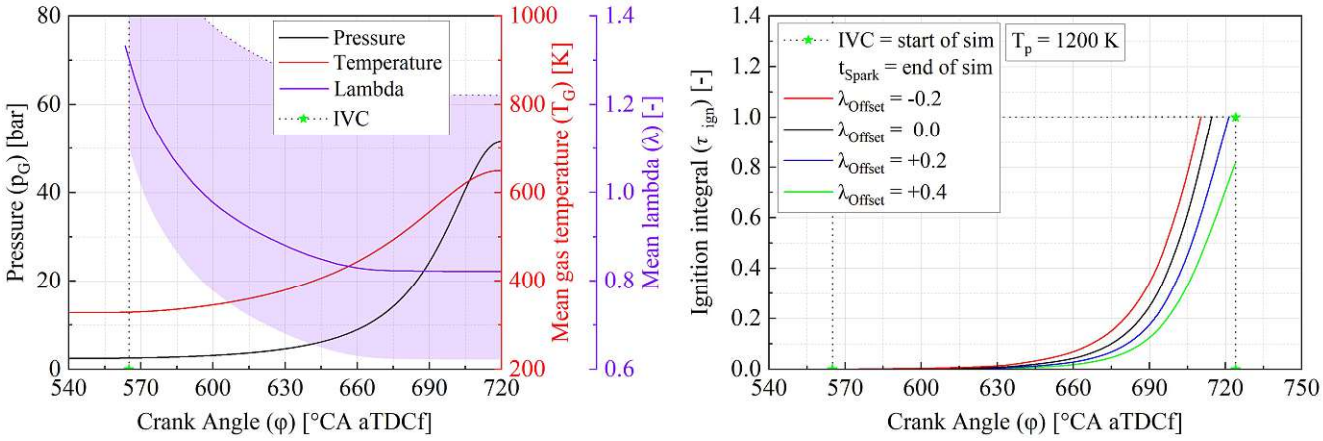

(**a**) (**b**)

Figure 8.13: (**a**) Scatter band of the lambda variation, (**b**) Sensitivity of the air-fuel ratio on the ignition integral.

The analysis aims to cover the conditions from normally aspirated engines up to highly boosted conditions, considering the variation of the initial gas pressure. Since the compression ratio in normally aspirated engines is typically higher than in boosted ones, a pressure of 30 bar at TDC is considered normally aspirated. The simulation predicts no PI in the normally aspirated case, consistent with reported data in the literature. However, the sensitivity appears to be remarkably low. A reduction of 0.5 bar in boost pressure is necessary to shift the predicted ignition timing to TDC (= 5.4 °CA). A similar low sensitivity can be observed in the case of the air-fuel ratio. Simulations were conducted within the range of λ = 1.22 to 0.62, covering both lean and very fuel-rich homogeneous operation conditions. In this analysis, over-stoichiometric conditions are required to reduce the reactivity of the ambient gas sufficiently to suppress a premature ignition.

Higher sensitivity can be found when considering the initial gas temperature (representing the effectiveness of the intercooler setup). A 50 K hotter charge temperature leads to a 7.7 °CA earlier predicted ignition. Nevertheless, a reduction of 47 K ($T_{G,IVC}$ = 278 K) is required to suppress an ignition before spark timing.

The change in the predicted ignition timing for a 10 % increase is calculated to establish comparability between the individual parameters. The reference values and the results are summarized in Table 8.2.

Table 8.2: Normalized sensitivity of the thermodynamic boundary conditions at a particle diameter of 250 µm.

Reference values	Change in ignition timing for a 10 % increase
Particle temperature (T_P) = 1200 K	-20.8 °CA
Gas temperature (T_G) = 325 K (@ IVC)	-5.2 °CA
Gas pressure (p_G) = 2.5 bar (@ IVC)	-2.1 °CA
Equivalence ratio (λ_{TRF}) = 0.82	+2.7 °CA

Overall, particle temperature appears to be by far the most sensitive and decisive parameter. High boost pressures and especially lean operation conditions are reported to increase the PI-frequency, considering experimental observations. [20, 41] Concerning the ambient gas reactivity, this effect cannot be explained. Since the particle temperature is set constant in this investigation, the contra-indicated lambda sensitivity and the low influence of the gas pressure suggest that these parameters are cross-influencing the present particle temperature. Therefore, these results suggest that the ignition-inducing particle may be reactive in nature which agrees with recent research findings by Okada [29], Gupta [74], and Wang [73].

8.4. Analysis of the thermodynamic history of a detached particle

The previous section revealed the importance of particle temperature with respect to particle-induced LSPIs. Therefore, the determination of expectable particle temperatures under in-cylinder conditions is crucial to evaluate the ignition risk of heat transferring objects. Furthermore, the analytical results suggest that the ignition initiating object may be reactive in nature.

In order to confirm that observation, the heat-up process of inert and reactive detached particles during consecutive conventional cycles in OP 1 is investigated using a stochastic particle release in analogy to the investigations of section 7. This method enables the observation of possible trajectories through the combustion chamber during the compression stroke as well as the reduction of the particle count due to the gas exchange process by inserting a sufficient number of Lagrangian parcels from deposit-prone regions. The seeding locations of the particles are defined according to the optical observations made during the experiments and numerically identified fuel film-prone areas. The thermophysical properties of the simulated particles are derived from literature data, based on the assumption that formed deposits are carbon-based structures similar to soot and coal. The used data is summarized in Table 8.3.

Table 8.3: Thermophysical properties – deposits.

Thermophysical properties	Used value	Reference
Thermal mass ($\rho * c_p$)	1000 kJ/m³K	[156]
Density ρ	1800 kg/m³	[93, 157]
Conductivity k	1.06 W/mK	[156]

In order to achieve multi-cycle simulation capability, the full engine CFD model is extended to deal with the expected partially pre-mixed combustion. Therefore, the well-known G-equation approach is applied. [158, 159, 160, 161] The calculation of the laminar flame speed is performed using the empirical correlation of Gülder. [162] Based on this correlation, the accelerating effect of the turbulent flow field on the apparent flame speed is acknowledged by equation 8.4.

$$s_T(\Phi) = s_L(\Phi) * \left[1 + A_{TKE} * \left(\frac{u'}{s_L(\Phi)}\right)^{5/6}\right] \qquad (8.4)$$

$$u' = \left(\frac{2}{3}TKE\right)^{1/2} \qquad \Phi = \frac{Z}{1-Z} * \frac{1 - Z_{stoich}}{Z_{stoich}}$$

In this equation, the laminar flame speed s_L is corrected by the turbulent kinetic energy *TKE* and a calibration coefficient A_{TKE}. Post flame, the burnt gas is assumed to be in a thermal equilibrium state and is modeled by a 7-species (Fuel, N_2, O_2, H_2, CO_2, H_2O, CO) equilibrium composition mechanism. [163] The spark ignition is modeled by a numerical local heat release, including a ramp-up function. The specified ramp-up period simplifies the flame kernel creation process initiated by the spark. After consuming the fuel in a specified radius around the electrode gap, the heat release is controlled by the levelset combustion model. Additionally, a single component surrogate replaced the previously implemented detailed 11-component fuel model to avoid excessive runtimes. Thermodynamic properties are set to the mean values of the unevaporated 11-component surrogate model to minimize the influence on the established spray model. Furthermore, the lower heating value is set according to the supplied fuel specification to 42.9 MJ/kg.

The calibration of the implemented combustion and ignition model and their tuning parameters respectively is performed in OP 1. The final result of the iterative calibration process is shown in Figure 8.14.

Parameter	Used value
A_{TKE}	3.6
Ramp-up period	4.3 °CA
Switch radius	1 mm

(**a**)

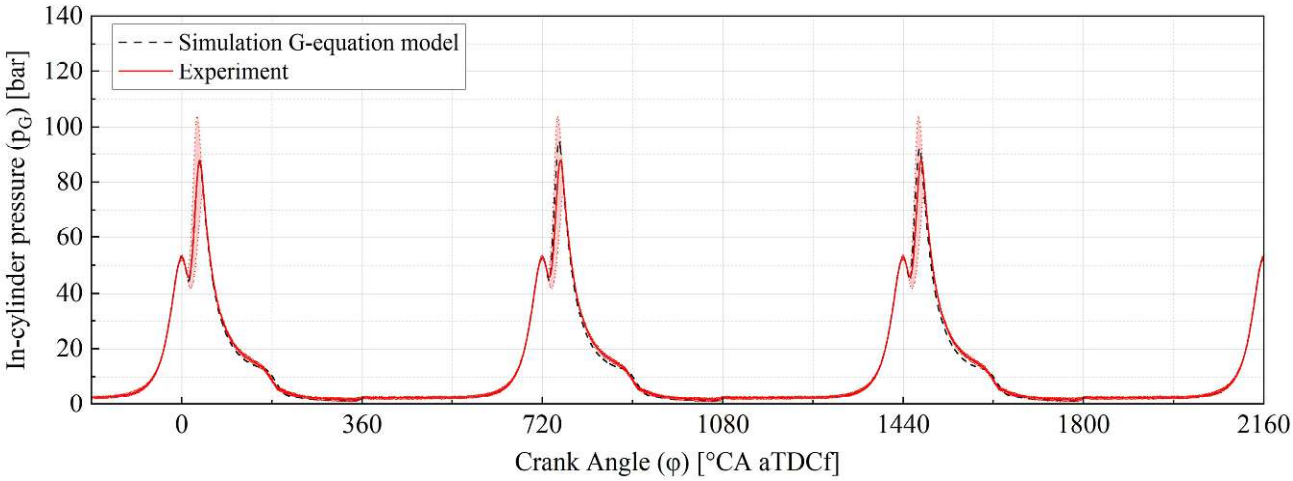

(**b**)

Figure 8.14: (**a**): Calibrated parameters of the ignition and combustion model, (**b**) Comparison of the measured and simulated in-cylinder pressure trace.

The comparison of the measured and calculated in-cylinder pressure trace shows only minor deviations. Furthermore, the cycle-to-cycle variation remains small and within the measured min/max bandwidth over three consecutive combustions. Therefore, the adaptions to the CFD model are considered adequately calibrated in order to investigate the thermal heat-up of detached particles.

Ignition risk of inert particles

In a first step, the heat-up of detached particles resulting from consecutive conventional combustions is investigated, neglecting a possible heat release from solid-phase oxidations. This method allows for an isolated analysis of the requirement of reactive particles triggering premature ignitions under experimentally evaluated prone conditions.

Therefore, 10,000 particles are released during the compression stroke to get a sufficient statistical representation of possible trajectories in three consecutive cycles. The size of detached particles is based on the estimations made using in-cylinder imaging with respect to ignition-critical diameters. Therefore, particle diameters ranging from 100 µm to 500 µm are released at fuel-wetted piston crevice locations representing a conservative spectrum in both directions. The lower end represents a particle size that could not be correlated experimentally with ignition initiation, and the upper limit corresponds to twice the piston crevice width. The release timing during the compression stroke in the initial calculated cycle is set to 680 °CA aTDCf. This timing represents the earliest observed detachment event during the experiments. The initial particle speed is defined randomly between 1 m/s and the maximum observed initial speed. The initial temperature of the particle is assumed to be controlled by the piston or liner wall temperature. Therefore, a temperature of 463 K is chosen based on literature data [8, 164, 165, 166, 167]. Table 8.4 summarizes the parameters used in the simulation.

Figure 8.15 shows the calculated particle temperature history using the calibrated combustion and ignition model setup in the stochastic release simulation during three consecutive engine cycles. Furthermore, the temporal evolution of the present particle Reynolds numbers is shown.

Table 8.4: Summary of the statistical particle release setup.

Parameter	Unit	Used value(s)	Reference
Initial Speeds	[m/s]	1.0 – 7.5	In-cylinder imaging
Release timing	[°CA aTDCf]	680	Earliest observable detachment event
Initial particle temperature	[K]	463	Assumption (avg. piston/liner)
Diameter classes	[µm]	100, 200, 300, 400, 500	Engine geometry and in-cylinder imaging
Total released particle count	[#]	10,000 (2,000 each diameter class)	

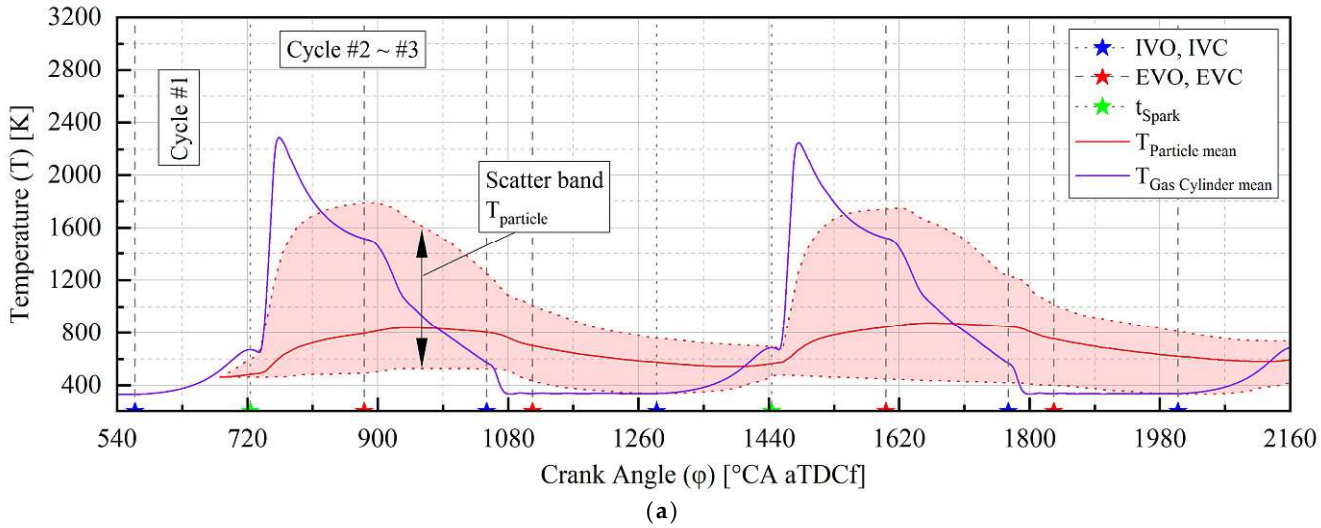

(**a**)

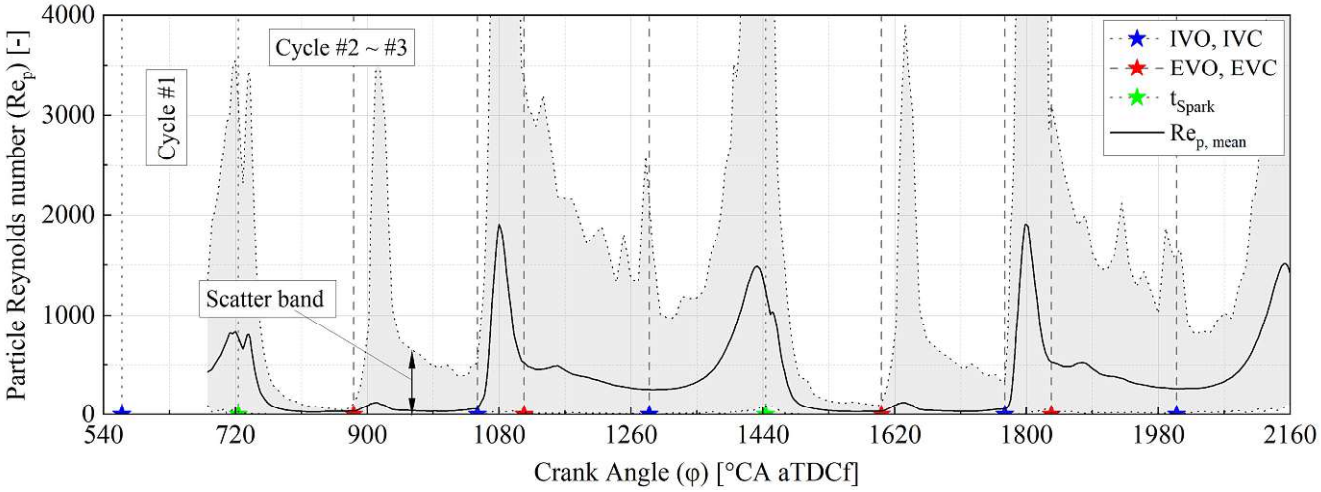

(**b**)

Figure 8.15: Temporal evolution of (**a**) inert particle temperatures and (**b**) particle Reynolds numbers.

The solid red line in Figure 8.15 (**a**) displays the mean particle temperature. Additionally, the minimum and maximum calculated values of all particle values are shown (red shaded area). After the initial release of particles fairly advanced in the compression stroke, only minor temperature increases can be observed. Just the smallest particles, due to their low thermal inertia, are able to get close to the ambient gas temperature of ~650 K at TDC. Concerning the next cycle (#2), the particles are heated up during the combustion and expansion phase. The hottest particles reach a temperature level of ~1200 K at IVO. The incoming fresh air is cooling down the particles effectively due to high relative velocities and high gas-solid temperature gradients. As a result, the mean particle temperature continuously falls towards TDC. At -40 °CA aTDCf the mean particle temperature meets the mean in-cylinder gas temperature stopping the cooling process, resulting in an average particle temperature of 575 K at spark timing. Concerning the hottest particles inside the combustion chamber, the maximum observable temperatures are below 800 K towards the end of the compression stroke. The subsequent combustion heats up the particles again. However, the predicted min/max range of the particle temperatures remains almost identical to the previous cycle showing a minor increase of 30 K. Calculating the ignition integral for each particle

in each compression stroke, the result predicts that none of the released particles are able to initiate an ignition under the investigated engine operation point due to insufficient surface temperatures.

With respect to a continuous particle heat-up over several engine cycles, the investigation analysis was extended to evaluate a minimum surface temperature that is necessary to initiate an ignition at TDC starting from IVC. Therefore, a fixed and iteratively defined particle temperature is used in this analysis.

The investigation showed that a constant minimum surface temperature of 1160 K is required to induce an ignition. Furthermore, the study showed minor deviations between the analyzed compression strokes, indicating a sufficient statistical representation of the inserted particle count. Figure 8.16 displays the gas temperature and lambda history of the top 5 most critical particles during the compression strokes of cycles #2 and #3. Additionally, the predicted min/max, as well as the mean values of the entire cylinder charge during the second engine cycle, are shown. The resulting ignition integral is plotted in Figure 8.17.

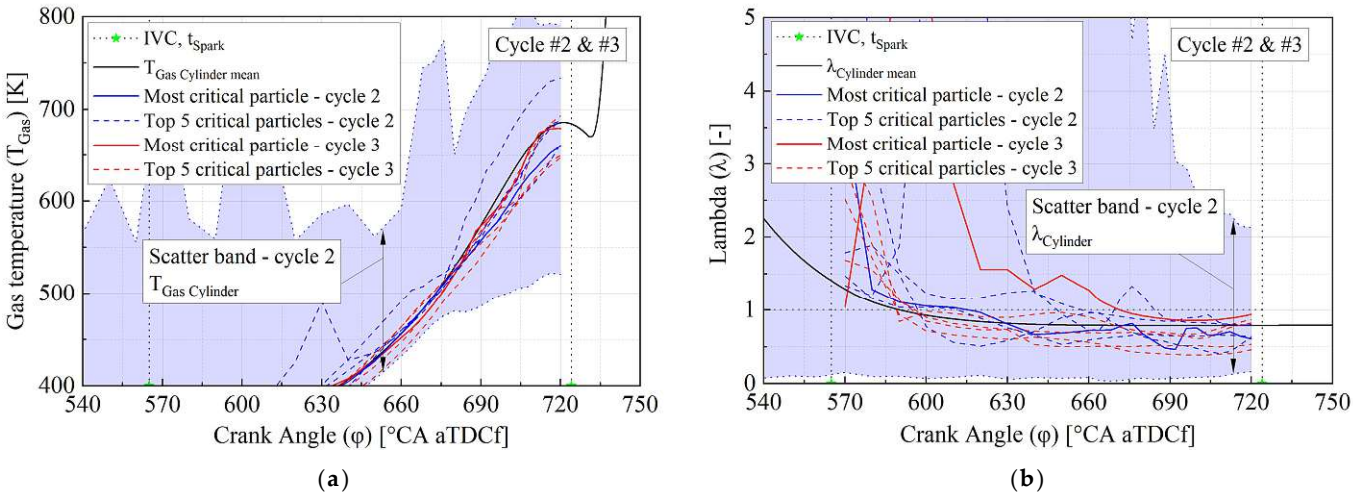

Figure 8.16: Thermodynamic history of the gas phase in the vicinity of the released particles during the second and third engine cycle. (**a**) gas temperature, (**b**) lambda.

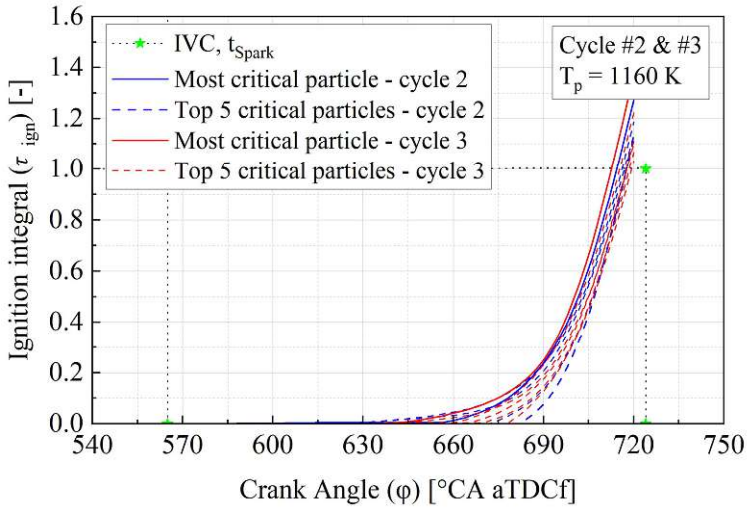

Figure 8.17: Temporal evolution of the ignition integral during the compression stroke using a constant particle temperature of 1160 K.

Looking into the thermodynamic history of these most critical particles, one can see that the particle pathways differed significantly during the early phase of the compression, whereas the deviation got smaller towards TDC. Overall, it can be observed that the most critical pathways were near the mean in-cylinder conditions and not at extreme values. Although, a slight shift towards cooler and fuel-rich regions can be noticed.

The observed pathways result in a sharp increase of the predicted ignition integral towards TDC, highlighting the influence of the ambient gas-phase conditions on the hot particle-induced ignition process. In the early phase of the compression stroke, the relative particle velocities induced by the gas exchange suppress ignition effectively. The ongoing dissipation of the gas phase momentum and turbulent energy leading to a decrease in relative velocity and thus mean particle Reynolds number and the associated scatter band. However, the kinematic viscosity of the ambient decreases with progressing compression leading to an increase in particle Reynolds numbers towards TDC. As a result, the mean Reynolds number surpasses the predicted "blow-out" threshold of Re_P = 672 at -48 °CA aTDCf. Consequently, particles below the observed average are able to initiate ignition. This observation indicates that particles with a low Stokes number and thus small diameter are predestined for ignition induction. In contrast, the small surface area reduces the heat transfer and elongates ignition delay times. The postprocessing of (in total) 44 ignitable particles of cycles #2 and #3 reveals a sweet spot at 200 µm, as shown in Figure 8.18 (**a**). Below that sweet spot, the particles are not prone to ignite the surrounding ambient compared to bigger ones. With increasing diameter, the probability of ignition reduces significantly. This observation correlates very well with optically derived size estimations of glowing objects inside the combustion chamber.

On the other hand, each gas exchange process reduces the particle count significantly, shown in Figure 8.18 (**b**). It can be observed that each diameter class is reduced by at least 50 % in each engine cycle, whereby smaller particles are flushed out more efficiently due to their low inertia counteracting the enhanced ignition probability. The significant reduction of small particles also manifests in the observed sample size of ignitable particles reducing the critical particle number from 38 to 6 in the consecutive cycle.

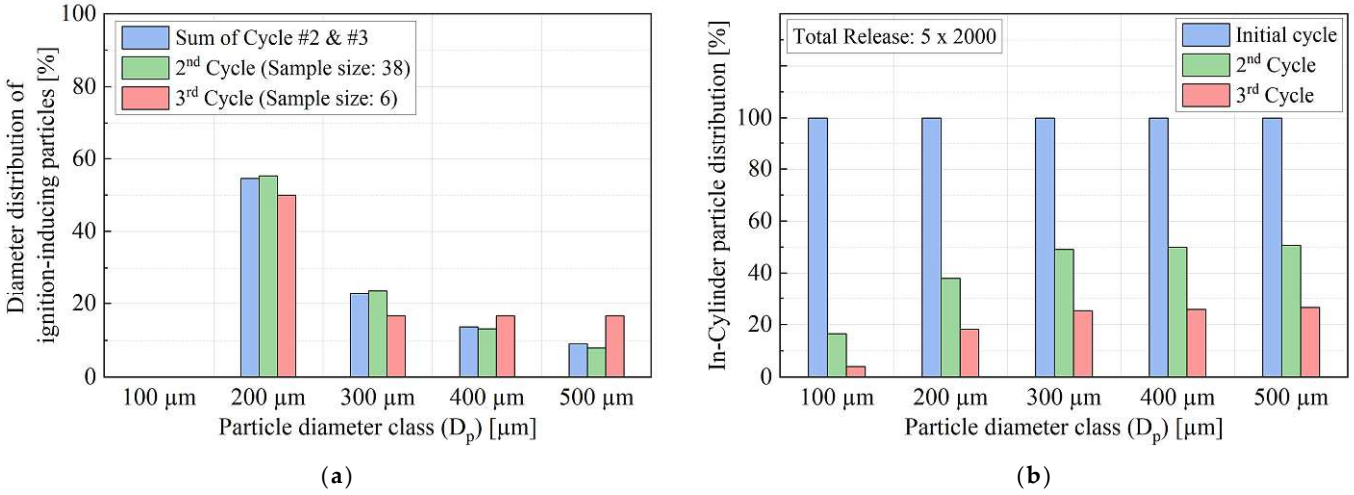

Figure 8.18: Particle diameter histograms. (**a**) Derived diameter distribution of critical ignition-inducing particles, (**b**) Diameter distribution of all particles inside the combustion chamber over three consecutive cycles.

Based on the predicted necessary constant particle temperature and the slow increase of ~30 K per cycle, it is very improbable that a non-reactive particle is able to reach a sufficiently high surface temperature to initiate an ignition in the investigated engine setup.

Influence of carbon oxidation reactions

The analysis of the previous section showed that non-reactive particles are suffering from insufficient surface temperatures near TDC. This result confirms the findings of the analytical investigation of section 8.3., suggesting a cross-influence of gas pressure and air-fuel ratio, and experimental observations using high-speed imaging showing objects starting to glow during the compression stroke. Consequently, an ignition-inducing particle requires an additional heat source via exothermal chemical reactions.

The composition and the chemical reactivity of such particles are fairly unknown due to the complex composition of the hydrocarbon sources (fuel & oil). Especially, inorganic components of additive packages of lubricating oil are assumed to catalyze oxidation reactions of the carbon-based structures. Since there are many uncertainties considering the complex interaction of inorganic substances on the chemical kinetics, this analysis uses a "reverse engineering" approach. Therefore, the analysis investigates the possibility of pure carbon-based particles to initiate LSPIs enabling a statement on the importance of catalytic substances and thus the involvement of lubricating oil.

Considering the chemical kinetics of the modeled carbon-based solid structures, the simplified model of Nagle and Strickland-Constable (NSC) [168] using the improved parameter settings by Walls [169] for temperatures ranging from 1273 to 2673 K is implemented, summarized in equation 8.5.

$$\dot{m}_{NSC}(T, p_{O2}) = A_p * \left[\left(\frac{k_A * p_{O2}}{1 + k_Z p_{O2}}\right) * x + k_B * p_{O2}(1 - x)\right] \tag{8.5}$$

$$x = \frac{1}{1 + \frac{k_T}{k_B * p_{O2}}}$$

$$k_A = 20 * e^{-30000/RT} \qquad k_B = 4.46 * 10^{-3} * e^{-15200/RT}$$

$$k_T = 1.51 * 10^5 * e^{-97000/RT} \qquad k_Z = 21.3 * e^{4100/RT}$$

In this equation, k_A, k_B, k_T, and k_Z are kinetic pre-factors, A_P and p_{O2} represent the particle surface area and the partial pressure of oxygen. The heat of formation is set to 32.8 MJ/kg according to neat carbon oxidation.

Besides the implementation of the solid-phase heat release, all other simulation parameters are equal to the previous section. However, it has to be mentioned that the simulation duration is reduced to two consecutive cycles. Figure 8.19 shows the temporal evolution of the predicted particle temperatures compared to the results achieved using non-reactive particles.

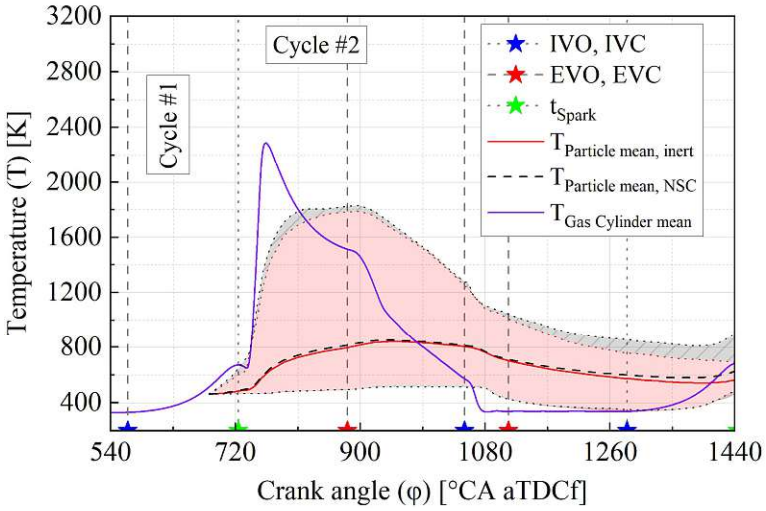

Figure 8.19: Influence of NSC-derived heat release on the predicted particle temperature.

After the initial release of the particles at 680 °CA aTDCf the calculated particle temperatures remain almost identical to the non-reactive case due to the overall low solid-phase temperature level. The subsequent combustion heats up the particles by heat transfer. As a result, the solid-phase reactions lead to a slightly faster increase in temperature during the early phase of combustion. The ongoing oxidation of the ambient gas phase consumes the available oxygen suppressing further chemical heat release of the particles. Therefore, the hot cylinder charge dominates the particle temperature at IVO, especially considering stoichiometric to fuel-rich in-cylinder operation conditions. The scavenging gas exchange process leads to a sharp increase in oxygen partial pressure enabling particle oxidation. However, the convective cooling effect of the incoming air overpowers the heat release calculated by the NSC reaction kinetics, leading to a decelerated loss of particle temperature levels. The ongoing compression results in a non-linear increase in oxygen partial pressure enhancing particle oxidation. This results in an amplified increase in solid-phase temperature towards TDC, especially for small particles. This effect leads to a net increase of 64 K in mean and 205 K in the maximum observable particle temperature at TDC compared to inert particles. As a result, some instances of particle trajectories experience a transition into an observable visual state by surpassing the Draper point (~798 K).

However, the overall temperature levels remain comparatively low to the minimum necessary constant temperature of 1160 K. Therefore, achieved temperature levels are insufficient to initiate a premature ignition within two cycles. The extension to multiple consecutive combustion events may slightly increase the mean particle level. However, the maximum achievable particle temperatures at IVO are dominated by the end-gas temperature and thus the in-cylinder air-fuel ratio in sub-stoichiometric conditions. Therefore, the continuous elevation of the mean temperature level appears to be limited considering the effectiveness of the gas exchange process with respect to particle count reduction.

Consequently, the initiation of LSPIs via neat carbon structures appears to be unlikely considering the predicted surface temperatures using the simplified NSC reaction mechanism, highlighting the importance of catalytically active substances enhancing the overall heat release. The achievable particle temperature level is the result of the energy balance considering the surface heat transfer to the ambient gas phase and the heat released via particle oxidation integrated from IVC to TDC. Assuming the same surface heat transfer and neglecting the loss in particle mass, the overall required heat release resulting from catalytically enhanced particle oxidation can be estimated by the temperature difference between

inert and reactive particle histories. In order to initiate a premature ignition, the desired heat release needs to be increased by a factor of 3.2, considering the maximum observable particle temperature history and a particle diameter of 200 µm.

Robustness of simulation results considering NSC oxidation rates

One has to acknowledge the uncertainties arising from the simplified simulation approach. The assumption of a perfectly smooth and spherical shape of the particles may underestimate the reactive surface area, especially considering internal oxidation processes. Investigations on nanometer-scale soot particles showed that the diffusion of oxygen molecules significantly influences low-temperature soot oxidation into the porous structures. [170, 171] The used NSC equations simplify this phenomenon by introducing two coupled reaction rates resulting in a predefined model generalization. Kelesidis [170] reported that the oxidation rate of nascent ethylene soot (< 100 nm) is underestimated by a factor of 3 to 5 at a temperature level of 1010 K. Whereby Camacho [172] observed that nascent ethylene soot shows an order of magnitude faster reaction kinetics than mature soot, relativizing the statement of Kelesidis [170]. However, the share of internal oxidation decreases at elevated temperature levels ($T_P > 1100$ K), resulting in a reduction of the reported deviation arising from the NSC model simplifications. As a result, a slightly underpredicted heat release at low particle temperatures may occur in the simulation model.

In order to investigate the sensitivity of the modeled reactive surface area, the study shown in the previous section is repeated using an artificial area scaling factor of 2. As a result, the released heat predicted by the NSC-equation is doubled on each simulated particle. Figure 8.20 shows the history of the calculated particle temperature of the modified NSC model in comparison to the non-scaled case.

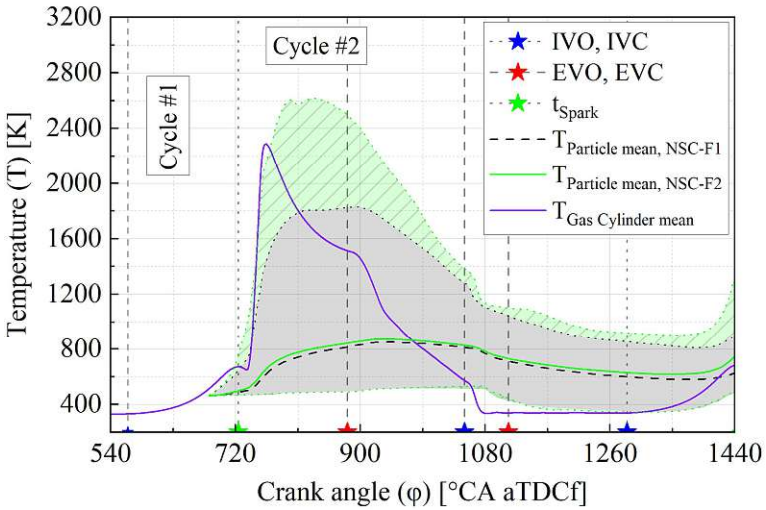

Figure 8.20: Influence of modeled reactive surface area on the predicted particle temperature.

The assumption of wall temperature-controlled initial particle temperatures leads to low carbon oxidation rates and thus heat release during the first engine cycle. Consequently, the particle temperature history is dominated by the ambient gas phase resulting in similar temporal evolutions. The subsequent combustion leads to a sharp increase in surface temperature, enhancing the solid-phase oxidation. The modified case shows a significant steeper gradient in the early phase of the combustion

process, allowing the particles to achieve higher temperature levels before the propagating flame consumes the oxygen. At this point, the expanding cylinder charge dictates the calculated particle temperatures independently of the used reaction kinetic configuration. As a result, the observed temperatures at IVO of both simulation cases converged to almost identical conditions.

The subsequent cooling effect of the incoming fresh air overpowers the predicted heat release from the NSC model even considering the artificially doubled reactive surface area. At IVC, a net increase of ~30 K in the mean particle temperature level and ~60 K in the maximum predicted temperature could be observed compared to the non-scaled simulation. However, the low gas pressure level, as well as particle temperatures in the early phase of the compression stroke, prevent high rates of carbon oxidation, barely compensating the convective heat transfer to the ambient cylinder charge. The intensified thermodynamic conditions towards the end of the compression stroke amplify the predicted heat release resulting in a significantly faster particle heat up, especially in the case of small particles. Although the artificially doubled reactive surface area leads to a substantially increased maximum surface temperature at TDC, the calculated ignition integral of the most critical particle histories does not surpass 0.12.

Consequently, the performed sensitivity analysis confirms the statement of the previous section that the initiation of LSPIs via neat carbon structures is unlikely. This finding is in accordance with experimental observations of artificially introduced particles investigated by Okada [29], Wang [73], and Schweizer [18]. The latter author reported that injected deposits resulting from neat gasoline had not initiated an LSPI under the exact same boundary conditions and engine configuration presented in the previous section.

9. Summary and conclusion

The governing hypothesis involving detached objects inducing LSPIs has emerged from previous work and has been widely accepted in the scientific community. However, there is no consensus on the second phase itself. Though attempts have been published indicating either liquid oil-fuel droplets or solid structures as the root cause for LSPI.

In the case of liquid oil-fuel droplets, it is assumed that the injected gasoline impinges on the cylinder liner. The moving piston collects the not evaporated fuel film leading to an accumulation of liquids inside the piston crevice volume. The low viscosity of the fuel leads to increased mobility of the liquid mixture resulting in droplet detachments due to the induced perturbation from the gliding piston ring or inertia forces due to the reciprocating motion. The missing cooling effect of the wall heat transfer enables such detached droplets to reach higher temperature levels leading to enhanced evaporation rates of long-chained hydrocarbons (lubricant oil species). Such species enhance the chemical reactivity of the surrounding fuel-air gas phase and may lead to autoignition.

The second evolved theory assumes that the hydrocarbon-based operating media forms deposits due to incomplete combustion on the combustion chamber walls. Such growing structures break loose and are heated up via consecutive conventional combustion cycles and may result in an air-borne hot spot-induced ignition.

Although very comprehensive studies are already performed, it is still unclear whether the observed second phases are oil-based droplets or solid structures nor if such detached objects are able to ignite the surrounding air-fuel mixture in time. Therefore, the work at hand presented an analytical investigation of the mechanism of the LSPI phenomenon in highly boosted SI engines utilizing extensive experimental and numerical methods to gain and extend the current knowledge.

In order to achieve a comprehensive understanding of the phenomenology of LSPI combustions, a modified turbocharged SI engine with central gasoline direct injection is mounted on a research engine testbed. The used engine configuration enables thermodynamic as well as optical monitoring of the ignition and combustion process using high- and low-pressure indication and high-speed imaging. Furthermore, fluorescence dye-doped operating media (fuel & lubricating oil) accompanied by wavelength-filtered observations are utilized to characterize in-cylinder recordings.

The optical observation of the combustion chamber revealed two consistent history patterns of LSPI initiations. In both cases, light-emitting spots are detected before the initiation of a deflagrative flame front, finally leading to super-knock combustion. The spots were either flying through the combustion chamber (“object-driven”) or sticking on the piston and liner walls (“deposit-driven”). Whereas the “object-driven” initiation shows no clear pattern with respect to the ignition locations, the “deposit-driven” initiation is located at a specific location near the piston crevice area showing intensive pool fires. The latter is characterized by a sequence of mild premature ignition before super-knock combustion, typically supported by the appearance of an additional ignition source (flying object) inside the combustion chamber. The subsequent super-knock combustion triggers the frequently reported cluster of LSPI follow-up events, independently from the history prior to the initial super-knock event.

The utilization of light-induced fluorescence revealed no liquid oil-containing droplets prior to an initial LSPI event, indicating a pre-oxidized solid state. However, a mist of detached oil droplets could be detected on rare occasions after very strong knocking. Nevertheless, no LSPI with subsequent super-knock combustion could be detected without observing a light-emitting history inside the combustion chamber, confirming the governing two-phase induced LSPI hypothesis.

In order to investigate the influence of mixture preparation and liquid film formation inside the combustion chamber, a variation of the fuel injection pressure and SOI was performed while maintaining the effective power output of the load point. The detailed description of droplet trajectories, evaporation, and mixing behavior of the injected fuel is analyzed by using a high-resolution CFD model of the endoscopically accessed cylinder (~5x10^6 cells @ 333 cm^3 V_{cyl}) incorporating an 11-component fuel surrogate fluid model. The selection of adequate species replicating the real fluid evaporation behavior as well as the basic chemical composition (shares of alkanes, aromatics, naphthenes, etc.) was performed by using an established and well-validated 0D distillation model. Further, the fluid model incorporates activity coefficients calculated by the UNIFAC method to account for mixing effects in the liquid phase.

The numeric analysis identified a correlation between the liquid film mass on the cylinder and piston surface at ignition timing and the recorded LSPI frequency during the experiments observing a runtime period of 20,000 to 50,000 engine cycles. Especially, the film mass on the piston surface correlated exceptionally well with the experimental data, contra-indicating previous literature observations. However, the correlation may result from the specific location of the wetted area being close to the piston crevice volume and further coinciding vertically with fuel film on the cylinder liner. The possible interaction with the wetted area on the liner indicates a superimposing effect of a local oil dilution, resulting in increased mobility of oil-fuel mixtures, and pronounced pool fires near the piston crevice area, promoting deposit formation and detachment.

The investigation of the film species mass fractions showed that components with a normal boiling point above 372 K are accumulated in the evaporating liquid puddles, whereas more volatile species are reduced. Consequently, fuels having an elevated share of low-volatile species will increase spray / wall interactions. This confirms reported literature data on fuel variation, showing an increased LSPI frequency for fuels with an elevated distillation curve above 393 K, highlighting the importance of liquid fuel / wall interactions. The loss of high-volatiles and thus autoignition resistant species may promote the ignitability of possibly detached droplets. However, the model also indicates an accumulation of aromatic species since all gasoline-relevant aromatics have an NBP above the observed threshold. Such species are known to increase RON specification and may counteract the loss of high-volatiles. Additionally, an increased share of aromatic species promotes soot and deposit formation.

Considering the mixing quality determined by the distribution of the injected fuel within the cylinder charge and the resulting gas temperature bandwidth, it could be observed that operating points showing a high LSPI frequency tend to have a poorer mixture preparation at the end of the compression stroke. However, the broader distribution is mainly influenced by the intensity of fuel wall wetting, generating very fuel-rich zones. Besides the observed cross-influence of evaporating liquid puddles, the sensitive response in LSPI frequency by varying injection parameters could not be explained. Consequently, the overall gas phase homogenization and thus the variation in local chemical kinetic speeds of the fuel-air mixture seems to have a subordinate influence on the ignition-inducing mechanism.

In order to achieve a holistic picture of the ignition risk of a detached second phase, both discussed possibilities (particles or droplets) were numerically investigated in detail using the thermodynamic conditions of an LSPI-prone operation point. For that reason, detailed chemical kinetics were utilized to capture the reactive impact on the cylinder charge. The chemical reactivity of the used gasoline was modeled by a TRF-surrogate. The individual share of the three components was determined using the empirically defined modified Linear-by-Volume method based on RON and MON specifications. The ignition delay of long-chained hydrocarbon is mainly defined by the evaporation rate determining the time to form ignitable mixtures at some distance to the droplet surface. Therefore, a 4-component

surrogate is introduced based on the results of a GC analysis. The chemical reactivity is simplified by the highly reactive and well-studied n-heptane species.

LSPI combustions and the associated second phase detachment events are temporally distributed over several thousand engine cycles. Therefore, a stochastic release approach was employed based on the observation made during the experiments and literature data. The initialization of a variety of second phase properties allowed for tracking trajectories inside the combustion chamber and the thermodynamic histories in the vicinity of the detached second phase in a statistical way. The recorded histories were then used as input parameters for detailed reaction kinetic sub-models.

In the case of oil droplets of the size of the piston crevice gap width, the stochastic data showed an insignificant heat-up potential. The ambient gas temperature falls below the oil temperature defined by the HTHS-viscosity standard, limiting the effective time for heat transfer to ~60 °CA. Consequently, low evaporation rates were achieved, leading to a maximum observed oil mass fraction of ~0.2 % in the vicinity of the droplet. The reaction kinetic impact of lubricating oil on the ignition delay time of the ambient fuel-air mixture was studied using a homogeneous reactor model. The model predicted no autoignition even considering thermodynamic worst-case scenarios and the accumulation of semi-stable pre-oxidized species (ketohydroperoxides) accelerating chemical kinetics. An additional sensitivity analysis of the thermodynamic parameters showed that the accelerating effect of n-heptane on the mixture ignition delay time is insufficient at typical in-cylinder temperature levels during the compression stroke. Consequently, this phenomenon can be considered very improbable, especially in series engine configurations.

Whereas oil droplet-induced ignitions appear at some distance to the drop surface due to the contrary evolving gradients of gas temperature and reactive species concentration resulting from the vaporization process, hot particles induce ignitions solely by heat transfer. Therefore, a highly resolved CFD sub-model was established to capture the crucial steep temperature gradients and ignition processes close to the hot surface. In order to couple the results of the microscale sub-model with transient history data achieved by the stochastic release approach, an ignition integral approach is introduced. Therefore, an extensive set of pre-defined conditions are calculated to establish a multi-dimensional ignition delay map considering gas temperature, gas pressure, air-fuel ratio, particle temperature, particle diameter, and relative particle velocity. A sensitivity analysis revealed that particle temperature is by far the most sensitive and decisive parameter. Furthermore, the variation of the ambient air-fuel ratio showed a contrary effect compared to experimentally observed behavior indicating a cross-influence on a solid-phase exothermal reactivity by increasing the oxygen partial pressure.

The thermal histories of detached particles were determined by modeling the second phase according to literature data based on in-cylinder deposits, soot, and coal. Although it is safe to say that accumulated deposit structures are the result of incomplete combustion of the operating media and are thus carbon-based, the exact composition and chemical kinetics of such structures are fairly unknown especially considering inorganic substances originating from additive packages. Therefore, a “reversed engineering” approach was applied to predict the thermal history using inert and chemically reactive particles by assuming carbon oxidation using the well-known NSC model. This method allowed for an isolated analysis of the temperature evolution resulting from the heat transfer of consecutive conventional combustions and the influence of the modeled solid-phase exothermal reactions.

In the case of inert particles, the analysis revealed that the gained temperature during the combustion and exhaust stroke is mostly compensated by the cooling effect of the incoming fresh air due to the high relative velocities and the strong temperature gradient between the solid and the gas phase. This results in a continuous falling particle temperature from IVO to TDC, not matching optical observations of

objects starting to glow close to the end of the compression stroke. Furthermore, the observed cycle-to-cycle increase in particle temperature was comparatively low (~30 K). In contrast, the effectiveness of the gas exchange in reducing the in-cylinder particle count was at least 50 % per cycle and even higher for small particles. None of the released particles led to a predicted ignition in the established simulation model. These observations lead to the conclusion that inert particles are not able to trigger ignition in the investigated engine setup.

Based on the achieved history data, the particle temperature is artificially fixed and iteratively increased to investigate the minimum necessary constant particle temperature to initiate an LSPI close to TDC. The analysis showed that a few particles are predicted to trigger an ignition at a constant temperature of 1160 K. Further, the results revealed that the particle Reynolds number is a decisive parameter, effectively suppressing ignition up to -48 °CA with respect to mean conditions. As a result, a sweet spot between low particle inertia leading to low relative velocities and particle size determining the effective area of heat transfer is found at a particle diameter of 200 µm, perfectly matching experimentally determined size estimations.

Since inert particles are suffering from an insufficient surface temperature, the analysis was repeated, considering the additional heat released from carbon oxidation. The particle temperature at IVO is dominated by the end-gas temperature due to the lack of excess oxygen. This holds true for operation conditions at stoichiometric to fuel-rich in-cylinder conditions, which are typical in series engine applications considering high loads. After the IVO event, the oxygen partial pressure rapidly increases, enabling carbon oxidation. However, the heat transfer to the cold ambient overpowers the chemical heat release leading to a decelerated cooling effect of the modeled particles. The ongoing compression resulted in a non-linear increase in oxygen partial pressure, amplifying carbon oxidation and significantly increasing surface temperature. As a result, some instances of particles surpassed the Draper point, as observed in the non-filtered optical observations. Nevertheless, the simulated particle temperatures during the compression stroke are predicted to be insufficient to initiate an ignition before spark timing. Based on the achieved simulation data, the heat release resulting from particle oxidation would need to increase by an estimated factor of 3.2 to trigger LSPI.

Overall, the achieved results highlight the importance of catalytically active substances with respect to “object-driven” LSPIs. However, numerical methods and experimental observations did not show any evidence of oil-based droplet-induced autoignitions, even considering accelerated reaction kinetics. In contrast, numerical results of carbon-based reactive particles did match the observed LSPI phenomenon derived from optical recording and thermodynamic testbed results. Furthermore, the predicted heat release of spherical carbon structures calculated by the NSC model appeared to be insufficient confirming experiments of artificially injected soot and carbon black. Consequently, formed deposits require an embedded share of catalytically active substances most likely coming from lubricant oil additive packages.

10. Outlook

Many aspects of the LSPI phenomenon were investigated in the presented work at hand. However, there is still a lack of knowledge concerning detached structures. Until now, the occurrence of the initial LSPI is considered to be statistically distributed without showing a repetitive pattern. Therefore, a detailed cycle-to-cycle analysis of the key processes inside the combustion chamber is essential to gain further insights and enable a deterministic approach instead of using statistical methods.

Numerical and experimental investigations suggested a significant influence of lubricating oil on the formation of LSPI critical deposits. Therefore, one identified key process is the transport mechanism of lubricating oil inside the combustion chamber. Especially, the influence of enhanced oil mobility resulting from fuel dilution seems to be a crucial factor regarding LSPI frequency. Consequently, the transition to a non-ensemble averaged model approach enabling the determination of cycle-to-cycle variations concerning gas flow patterns and thus fuel droplet trajectories would be necessary with respect to numerical simulations. Further, the determination and implementation of the lubricating oil film on the cylinder liner and inside the piston crevice volume using a spatial discretizing modeling approach (i.e., VoF) may enable a better prediction of fluid interactions and dynamics.

Another identified key process is the mechanism of oil oxidation and deposit formation. Especially the influence of fuel dilution needs to be studied in detail. Therefore, a precise exploration of the involved chemical reactions triggered by consecutive conventional combustion events resulting in adhering carbon-based solid structures is essential to extend the current state of knowledge. Especially the influence of inorganic substances on the chemical reaction kinetics would improve the prediction quality of the thermal history and thus ignition risk of detached particles substantially. Additionally, the interaction of a possibly absorbed liquid phase inside the porous structure should be further investigated in subsequent studies.

Finally, an in-depth analysis of the mechanical stresses on the formed deposits resulting in a detachment event is vital to pave the way toward deterministic prediction approaches. Especially, the influence of surface treatments and detergent substances provided by the liquid operating media may limit adhesive forces and thus the effective detached particle diameters.

References

[1] Statista, available online: https://de.statista.com/ (accessed on 10.10.2021)

[2] Regulation (EG) Nr. 443/2009 of the european parliament

[3] Fraidl, G., Enzi, B., Kapus, P., Martin, C., Rothbart, M., Passenger car powertrains and future energy scenarios: From technical facts towards political reality. In Proceedings of the 42nd International Vienna Motor Symposium, Vienna, Austria, 29–30 April 2021, ISBN: 978-3-9504969-0-1.

[4] Xue, M., Wang, Q., Lin, B.L., Tsunemi, K., Mitigation of greenhouse gas and reactive nitrogen from the Japanese passanger car fleet. J. Clean. Prod. 277(123440), 2020.

[5] Bisenius, A., Groß, J., Hackmann, M., Schenk, J., Stanek, R., The CO2 footprint in the life cycle of passenger cars—A comparison of hybrid, plug-in and electric vehicles with a detailed consideration of battery production and the country-specific energy mix. In Proceedings of the 42nd International Vienna Motor Symposium, Vienna, Austria, 29–30 April 2021, ISBN 978-3-9504969-0-1.

[6] Clerk, D., The Theory of the Gas Engine. In: Minutes of Proceedings of the Institution of Civil Engineers, Vol. LXIX, London, 1882.

[7] Wang, Z., Liu, H., Reitz, R.D., Knocking combustion in spark-ignition engines. Progress in Energy and Combustion Science 61, p. 78-112, 2017, doi: http://dx.doi.org/10.1016/j.pecs.2017.03.004.

[8] Heywood, J.B., Internal combustion engine fundamentals. McGraw-Hill series in mechanical engineering. McGraw-Hill, New York, 1988.

[9] Ollivier, E., Bellettre, J., Tazerout, M., Roy, G.C., Detection of knock occurrence in a gas SI engine from a heat transfer analysis. Energy Conversion and Management, 47, p. 879-893, 2006, doi:10.1016/j.enconman.2005.06.019.

[10] Wang, W., Wang, Y., Reitz, R.D., Pressure Oscillation and Chemical Kinetics Coupling during Knock Process in Gasoline Engine Combustion. Energy & Fuels 26, p. 7107-7119, 2021, doi: dx.doi.org/10.1021/ef301472g.

[11] Douaud, A., Analysis of knock and its effects. Rev 1 Fr Petrole 38, p. 665-674, 1983.

[12] Enomoto, Y., Kitahara, N., Takai, M., Heat losses during knocking in a four-stroke gasoline engine. JSME Int. J. Ser B 37(3), p. 668-676, 1994, doi: https://doi.org/10.1299/jsmeb.37.668

[13] Syrimis, M., Characterization of knocking combustion and heat transfer in a spark ignition engine. PhD thesis, University of Illinois, Chicago, 1996.

[14] Grandin, B., Denbratt, I., The Effect of Knock on Heat Transfer in SI-engines. SAE technical paper 2002-01-0238, 2002, doi: https://doi.org/10.4271/2002-01-0238.

[15] Heiss, M., Approach for Modelling the Initiation Process of Low-Speed Pre-Ignition in Downsized SI-Engines. Ph.D. Thesis, Vienna University of Technology, Vienna, Austria, 2015.

[16] Vangraefschepe, F., Zaccardi, J.M., Analysis of destructive abnormal combustions appearing at high load and low engine speed on high performance gasoline engines. SIA Conference "The Spark Ignition Engine of the Future", Strasbourg, France, 2007.

[17] Palaveev, S., Untersuchungen zu den Ursachen von stochastischen Vorentflammungen bei aufgeladenen Ottomotoren. Ph.D. Thesis, Karlsruhe Institute of Technology, Karlsruhe, Germany, 2018.

[18] Schweizer, T.; Zöbinger, N.; Kubach, H., Lauer, T.; Koch, T. Experimental and numerical Low-speed pre-ignition analysis and mechanism synthesis on a turbocharged gasoline engine with direct injection. SAE International Journal of Engines 16(3), 2022, doi: 10.4271/03-16-03-0018.

[19] Schweizer, T., Kubach, H., Zöbinger, N., Lauer, T., Eder, M., Grabner, P., Schießl, R., Liu, C., Initial Pre-ignition. Final Report of the FVV-project no. 1328, FVV-Frankfurt am Main, 2021.

[20] Zahdeh, A., Rothenberger, P., Nguyen,W., Anabrarasu, M., Schmuck-Soldan, S., Schaefer, J., Goebel, T., Fundamental Approach to Investigate Pre-Ignition in Boosted SI Engines. SAE International Journal Engines 4(1), p. 246–273, 2011, doi: https://doi.org/10.4271/2011-01-0340.

[21] Kieberger, M., Untersuchung des Phänomens der Vorentflammung bei der ottomotorischen Verbrennung zur Bestimmung von Einflussfaktoren und von Auslösemechanismen. Ph.D. Thesis, Vienna University of Technology, Vienna, Austria, 2012.

[22] Hülser, T., Grünefeld, G., Brands, T, Günther, M., Pischinger, S., Optical Investigation on the Origin of Pre-Ignition in a Highly Boosted SI Engine Using Bio-Fuels. SAE Technical Paper 2013-01-1636, 2013, doi:10.4271/2013-01-1636.

[23] Dahnz, C., Han, K., Spicher, U., Magar, M., Schießl, R., Maas, U., Investigations on Pre-Ignition in Highly Supercharged SI Engines. SAE Int. J. Engines 3, p. 214–224, 2010.

[24] Günther, M., Morcinkowski, B., Kremer, F., Pischinger, S., Characterization of gasoline biofuels regarding combustion anomalies. Proceedings of the 14th Suttgart International Symposium - Automotive and Engine Technology 1, p. 417-434, 2013.

[25] Döhler, A., Pritze, S., A contribution to better understanding the pre-ignition phenomenon in highly charged internal combustion engines with direct fuel injection. Conference Proceedings on Knocking in Gasoline Engines, p. 41-61, Berlin, Germany, 2013.

[26] Kassai, M., Shiraishi, T., Noda, T., Fundamental Mechanism Analysis on the Underlying Process of LSPI Using Experimental and Modeling Approaches. International Conference on Knocking in Gasoline Engines, p. 89-111, 2017, doi: https://doi.org/10.1007/978-3-319-69760-4_6.

[27] Birkigt, A., Analyse von Vorentflammungsphänomenen an hoch aufgeladenen Ottomotoren mit Direkteinspritzung. Ph.D. Thesis, University of Erlangen-Nürnberg, 2011.

[28] Palaveev, S., Magar, M., Kubach, H., Schiessl, R., Spicher, U., Maas, U., Premature Flame Initiation in a Turbocharged DISI Engine – Numerical and Experimental Investigations. SAE Int. J. Engines 6(1), p. 54-66, 2013, doi: https://doi.org/10.4271/2013-01-0252.

[29] Okada, Y., Miyashita, S., Izumi, Y., Hayakawa, Y., Study of Low-Speed Pre-Ignition in Boosted Spark Ignition Engine. SAE Int. J. Engines 7(2), p. 584-594, 2014, doi:10.4271/2014-01-1218.

[30] Spicher, U., Gohl, M., Magar, M., Hadler, J., Die Bedeutung des Motoröls bei der Entstehung der Vorentflammung. MTZ Motortechnische Zeitschrift 77, p. 62-67, 2016, doi: https://doi.org/10.1007/s35146-015-0156-z.

[31] Lauer, T., Heiss, M., Bobicic, N., Holly, W., A Comprehensive Simulation Approach to Irregular Combustion. SAE technical paper 2014-01-1214, 2014, doi: 10.4271/2014-01-1214.

[32] Schünemann, E., Witt, A., Selder, M., Schwarz, C., Pre-ignition analysis on a turbocharged gasoline engine with direct injection. Conference Proceedings on Knocking in Gasoline Engines, p. 380-393, Berlin, Germany, 2013.

[33] Tanaka, J., Visualization of lubricating oil droplets near ring crevice on pre-ignition of super charged SI engine. Proceedings of the 15th Conference "The Working Process of the Internal Combustion Engine", Graz, Austria, 24-25 September, 2015.

[34] Tanaka, J., Visualization of lubricating oil droplets from piston crown on pre-ignition of super charged SI engines. Proceedings of the 16th Conference "The Working Process of the Internal Combustion Engine", Graz, Austria, 28-29 September, 2017.

[35] Moriyoshi, Y., Yamada, T., Tsunoda, D., Xie, M., Kuboyama, T., Morikawa, K., Numerical Simulation to Understand the Cause and Sequence of LSPI Phenomena and Suggestion of CaO Mechanism in Highly Boosted SI Combustion in Low Speed Range. SAE Technical Paper 2015-01-0755, 2015, doi: 10.4271/2015-01-0755.

[36] Doppler, M. Modellierung der Tropfenablösung aus dem Feuersteg eines Ottomotors mit einem Volume of Fluid Ansatz. Diploma Thesis, Vienna University of Technology, Vienna, Austria, 2020.

[37] Palaveev, S., "Untersuchungen zu den Ursachen von stochastischen Vorentflammungen bei aufgeladenen Ottomotoren," Ph.D. Thesis, KIT, Karlsruhe, Germany, 01/2018, ISBN:978-3-8325-4705-9.

[38] Singh, E., Mubarak Ali, M.J., Ichim, A., Morganti, K., Dibble, R., Effect of Mixture Formation and Injection Strategies on Stochastic Pre-Ignition. SAE Technical Paper 2018-01-1678, 2018, doi:10.4271/2018-01-1678.

[39] Leach, B., Smith, A., Pearson, R., Williams, J., Yates, R., Ritchie, C., Weall, A., Li, C., and Cooper, B., "Management of Low Speed Pre-Ignition via Fuel and Lubricant Formulation," 26th Aachen Colloquium Automobile and Engine Technology 2017, Aachen, 2017, p. 333-348.

[40] Morikawa, K., Moriyoshi, Y., Kuboyama, T., Imai, Y., Yamada, T., Hatamura, K., Investigation and Improvement of LSPI Phenomena and Study of Combustion Strategy in Highly Boosted SI Combustion in Low Speed Range. SAE Technical Paper 2015-01-0756, 2015, doi: 10.4271/2015-01-0756.

[41] Amann, M., Mehta, D., Alger, T., Engine Operating Condition and Gasoline Fuel Composition Effects on Low-Speed Pre-Ignition in High-Performance Spark Ignited Gasoline Engines. SAE Int. J. Fuels Lubr. 4(3), 2011-01-0342, 2011, doi: 10.4271/2011-01-0342.

[42] Mayer, M., Hofmann, P., Geringer, B., Williams, J., Moss, J., Kapus, P., Influence of Different Oil Properties on Low-Speed Pre-Ignition in Turbocharged Direct Injection Spark Ignition Engines. SAE Technical Paper 2016-01-0718, 2016, doi: 10.4271/2016-01-0718.

[43] Amann, M., Alger, T., Westmoreland, Rothmaier, A., The Effects of Piston Crevices and Injection Strategy on Low-Speed Pre-Ignition in Boosted SI Engines. SAE Int. J. Engines 5(3), 2012, doi: 10.4271/2012-01-1148.

[44] Ohtomo, M., Miyagawa, H., Koike, M., Yokoo, N., Nakata, K., Pre-Ignition of Gasoline-Air Mixture Triggered by a Lubricant Oil Droplet. SAE Int. J. Fuels Lubr. 7, p. 673-682, 2014, doi: 10.4271/2014-01-2627.

[45] Fei, S., Wang, Z., Qi, Y., Wang, Y., Investigation on Ignition of a Single Lubricating Oil Droplet in Premixed Combustible Mixture at Engine Relevant Conditions. SAE Technical Paper 2019-01-0298, 2019, doi:10.4271/2019-01-0298.

[46] Long, Y., Wang, Z., Qi, Y., Xiang, S., Zeng, G., Zhang, P., He, X., Effect of Oil and Gasoline Properties on Pre-Ignition and Super-Knock in a Thermal Research Engine (TRE) and an Optical Rapid Compression Machine (RCM). SAE Technical Paper 2016-01,0720, 2016, doi:10.4271/2016-01-0720.

[47] Yasueda, S., Takasaki, K., Tajima, H., Abnormal Combustion caused by Lubricating Oil in High BMEP Gas Engines. MTZ Industrial 3 (1), p. 34-39, 2013.

[48] Palaveev S., Magar, M., Koch, T., Untersuchung des Auftretens und der Ursache von Selbstzündungen vor Zündeinleitung bei aufgeladenen Motoren mit hohem Verdichtungsverhältnis. Final Report, Karlsruhe Institute of Technology (KIT), Informationstagung Motoren, Magdeburg, 2014.

[49] Blin-Simiand, N., Jorand, F., Keller, K., Fiderer, M., Sahetchian, K., Ketohydroperoxides and Ignition Delay in Internal Combustion Engines. Combustion and Flame 112 (1-2), p. 278-282, 1998.

[50] Magar, M., Wirbser, H., Schießl, R., Maas, U., Numerical Study on the Impact of Stable Intermediates on Engine Combustion. 4th European Combustion Meeting, Vienna, 2009.

[51] Magar, M., Numerische Untersuchung unkontrollierter vorzeitiger Selbstzündprozesse unter motorrelevanten Bedingungen. Ph.D. Thesis, Karlsruhe Institute of Technology, Karlsruhe, Germany, 2016.

[52] Dahnz, C., Han, K.-M., Magar, M, Vorentflammung bei Ottomotoren. Final Report of the FVV-project no. 931, FVV-Frankfurt am Main, 2009.

[53] Marran, D. F., Long, M. B., Studzinski, W. M., Swindal, C., Acker, W. P., Planar Laser-induced fluorescence imaging of crevice hydrocarbon emissions in a spark-ignited engine. Proceedings of the Combustion Institute 27(2), p. 2069-2076, 1998, doi: https://doi.org/10.1016/S0082-0784(98)80053-2.

[54] Basshuysen, R., Schäfer, F., Handbuch Verbrennungsmotor. 7th edition, Springer Vieweg, Wiesbaden, 2015, doi: 10.1007/978-3-658-04678-1.

[55] Mansfield, A., Chapman, E., Briscoe, K., Impact of Fuel Octane Rating and Aromatic Content on Stochastic Pre-Ignition. SAE Technical Paper 2016-01-0721, 2016, doi: 10.4271/2016-01-0721.

[56] Dec, J.E., Sjöberg, M., Isolating the Effects of Fuel Chemistry on Combustion Phasing in an HCCI Engine and the Potential of Fuel Stratification for Ignition Control. SAE Technical Paper 2004-01-0557, 2004, doi:10.4271/2004-01-0557.

[57] Kalghatgi, G., Fuel/Engine Interactions. Warrendale, PA: SAE International, 2014, doi: 10.4271/R-409.

[58] Dedl, J., Geringer, B., Budak, O., Pischinger, S., Kraftstoffkennzahlen zur Beschreibung von Vorentflammungen in Ottomotoren. MTZ Motortechnische Zeitschrift 79, p. 76-81, 2018, doi: https://doi.org/10.1007/s35146-018-0024-8.

[59] Dedl, J., Entwicklung und Validierung potenzieller Prüfmethoden zur Selbstzündungscharacterisierung von Ottokraftstoffen. Ph.D. Thesis, Vienna University of Technology, Vienna, Austria, 2019.

[60] Bobicic, N., Hofmann, P., Garbe, T., Hönig, M., Prüfverfahren zur Bestimmung der Vorentflammungsstabilität von Kraftstoffen. MTZ Motortechnische Zeitschrift 82, p. 26-35, 2021, doi: https://doi.org/10.1007/s35146-021-0717-2.

[61] Bobicic, N., Ermittlung des Kraftstoffeinflusses auf die ottomotorische Vorentflammung und Entwicklung eines Prüfverfahrens für die Bestimmung der Vorentflammungsstabilität von Kraftstoffen. Ph.D. Thesis, Vienna University of Technology, Vienna, Austria, 2020.

[62] Martin, C., Graf, J., Geringer, B., Luef, R., Grabner, P., Eichlseder, H., Neue Prüfmethodiken des Klopfens und der Vorentflammung von Kraftstoffen und Ölen hochaufgeladener Ottomotoren. 35. International Vienna Motor Symposium, Vienna, 2014.

[63] DIN 51581: Testing of Petroleum Products – Determination of Evaporation Loss. 2011.

[64] Takeuchi, K., Fujimoto, K., Hirano,S., Yamashita, M., Investigation of Engine Oil Effect on Abnormal Combustion in Turbocharged Direct Injection - Spark Ignition Engines. SAE Int. J. Fuels Lubr. 5(3), p. 1017-1024, 2012, doi: 10.4271/2012-01-1615.

[65] Andrews, A., Burns, R., Dougherty, R., Deckman, D., Patel, M., Investigation of Engine Oil Base Stock Effects on Low Speed Pre-Ignition in a Turbocharged Direct Injection SI Engine. SAE Int. J. Fuels Lubr. 9(2), p. 400-407, 2016, doi:10.4271/2016-01-9071.

[66] Welling, O., Collings, N., Williams, J., Moss, J., Impact of Lubricant Composition on Low-speed Pre-Ignition. SAE Technical Paper 2014-01-1213, 2014, doi:10.4271/2014-01-1213.

[67] Morikawa, K., Moriyoshi, Y., Kuboyama, T., Yamada, T., Suzuki, M., Investigation of Lubricating Oil Properties Effect on Low Speed Pre-Ignition. SAE Technical Paper 2015-01-1870, 2015, doi:10.4271/2015-01-1870.

[68] DIN 51773: Testing of liquid fuels – Determination of ignition quality (cetane number) of Diesel fuels with the BASF-engine. 2010.

[69] Onodera, K., Kato, T., Ogano, S., Fujimoto, K., Kato, K., Kaneko, T., Engine Oil Formulation Technology to Prevent Pre-ignition in Turbocharged Direct Injection Spark Ignition Engines. SAE Technical Paper 2015-01-2027, 2015, doi:10.4271/2015-01-2027.

[70] Hirano, S., Yamashita, M., Fujimoto, K., Kato, K., Investigation of Engine Oil Effect on Abnormal Combustion in Turbocharged Direct Injection - Spark Ignition Engines (Part 2). SAE Technical Paper 2013-01-2569, 2013, doi:10.4271/2013-01-2569.

[71] Fletcher, K., Dingwell, L., Yang, K., Lam, W., Steyer, J., Engine Oil Additive Impacts on Low Speed Pre-Ignition. SAE Int. J. Fuels Lubr. 9(3), p. 612-620, 2016, doi:10.4271/2016-01-2277.

[72] Liang, X., Wang, Y., Wang, K., Wang, Y., Zhang, H., Zhao, B., Lv, X., Experimental study of impact of lubricant-derived ash on oxidation reactivity of soot generated in diesel engines. Proceedings of the Combustion Institute 38 (4), p. 5635-5642, 2021, doi: https://doi.org/10.1016/j.proci.2020.06.335.

[73] Wang, Z., Qi, Y., Liu, H., Long, Y., Wang, J.X., Experimental Study on Pre-Ignition and Super-Knock in Gasoline Engine Combustion with Carbon Particle at Elevated Temperatures and Pressures. SAE Technical Paper 2015-01-0752, 2015, doi:10.4271/2015-01-0752.

[74] Gupta, A., Seeley, R., Shao, H., Remias, J., Roos, J., Wang, Z., Qi, Y., Impact of Particle Characteristics and Engine Conditions on Deposit Induced Pre-Ignition and Super-knock in Turbocharged Gasoline Engines. SAE Int. J. Fuels Lubr. 10 (3), p. 830–841, 2017, doi: 10.4271/2017-01-2345.

[75] Merker, G.P., Teichmann, R., Grundlagen Verbrennungsmotoren. 7th edition, Springer-Vieweg, Wiesbaden, Germany, 2014, ISBN 978-3-658-03194-7.

[76] Pilling, M. J., Compton, R. G., Hancock, G., Low-Temperature Combustion and Autoignition. Comprehensive Chemical Kinetics Vol. 35. Elsevier, Amsterdam, Netherlands, 1997, ISBN: 9780080535654.

[77] Peters, N., Paczko, G., Seiser, R., Seshadri, K., Temperature Cross-Over and Non-Thermal Runaway at Two-Stage Ignition of n-Heptane. Combustion and Flame 128 (1-2), p. 38-59, 2002, doi: https://doi.org/10.1016/S0010-2180(01)00331-5.

[78] Westbrook, C. H., Chemical kinetics of hydrocarbon ignition in practical combustion systems. Proceedings of the Combustion Institute 28 (2), p. 1563-1577, 2000, doi: https://doi.org/10.1016/S0082-0784(00)80554-8.

[79] Leppard, W. R., The Chemical Origin of Fuel Octane Sensitivity. SAE technical paper, 902137, 1990, doi: https://doi.org/10.4271/902137.

[80] Curran, H. J., Gaffuri, P., Pitz, W. J., Westbrook, C. K., A Comprehensive Modeling Study of n-Heptane Oxidation. Combustion and Flame 114 (1-2), p. 149-177, 1998, doi: https://doi.org/10.1016/S0010-2180(97)00282-4.

[81] Curran, H. J. et al.: A comprehensive modeling study of iso-octane oxidation. Combustion and Flame 129 (3), p. 253-280, 2002, doi: https://doi.org/10.1016/S0010-2180(01)00373-X.

[82] Mohamed, C., Suppression of reaction during rapid compression and its effect on ignition delay. Combustion and Flame 112 (3), p. 438-444, 1998, doi: https://doi.org/10.1016/S0010-2180(97)00135-1.

[83] Glassmann, I., Yetter, R. A., Combustion. 4th edition, Academic Press, Elsevier, Oxford, UK, 2008, ISBN: 978-0-12-088573-2

[84] Warnatz, J., Maas, U., Dibble, R. W., Verbrennung. 3rd edition, Springer-Verlag Berlin-Heidelberg, Germany, 2001, ISBN: 3-540-42128-9.

[85] Semenov, N. N., Chemical Kinetics and Chain Reactions., Oxford University Press, 1935.

[86] Zeldovich, Y. B., Barenblatt, G.I., Librovich, V.B., and Makhviladze, G.M., Combustions and Explosions. Consultants Bureau, 1985.

[87] He, L., Clavin, P., Premixed Hydrogen-Oxygen Flames. Part II: Quasi-Isobaric Ignition Near the Flammability Limits. Combustion and Flame 93 (4), p. 408–420, 1993, doi: https://doi.org/10.1016/0010-2180(93)90141-O.

[88] Zöbinger, N., Schweizer, T., Lauer, T., Kubach, H., Koch, T., Experimental and Numerical Analysis on Two-Phase Induced Low-Speed Pre-Ignition. Energies 14(16), 5063, 2021. doi: https://doi.org/10.3390/en14165063.

[89] Schweizer, T., Kubach, H.; Koch, T., "Investigations to characterize the interactions of light radiation, engine operating media and fluorescence tracers for the use of qualitative light-induced fluorescence in engine systems," Automot. Engine Technol., 2021, doi: https://doi.org/10.1007/s41104-021-00092-3.

[90] DIN EN 228: Automotive Fuels—Unleaded Petrol-Requirements and Test Methods; German version EN 228:2008; Deutsches Institut für Normung e.V.: Berlin, Germany, 2008.

[91] Baehr, H.D., Stephan, K., Wärme- und Stoffübertragung, 10th edition, Springer: Berlin, Germany, 2019; p. 644–654, ISBN: 978-3-662-58441-5.

[92] Pöschl, M., Sattelmayer, T., Influence of temperature inhomogeneities on knocking combustion. Combustion and Flame 153 (4), p. 562–573, 2008, doi: https://doi.org/10.1016/j.combustflame.2007.11.009.

[93] Siemens: Methodology STAR-CD (Version 4.30), Siemens Product Lifecycle Management Software Inc., Nürnberg, Germany, 2017.

[94] Bai, C., Gosman, A.D., Development of Methodology for Spray Impingement Simulation. SAE Technical Paper 1995, 950283, doi: https://doi.org/10.4271/950283.

[95] Bai, C., Gosman, A.D., Mathematical modeling of wall films formed by impinging sprays. SAE Technical Paper 1996, 960626, doi: https://doi.org/10.4271/960626.

[96] Chauveau, C., Halter, F., Lalonde, A., Gökalp, I., An Experimental Study on the Droplet Vaporization: Effects of Heat Conduction through the Support Fiber. ILASS Technical Paper 4-1, 2008.

[97] Nomura, H. and UJiie, Y., Experimental Study on High-Pressure Droplet Evaporation Using Microgravity Conditions. Proceedings of the 26th Symposium (International) on Combustion, p. 1257-1273, 1996.

[98] VDI-Gesellschaft Verfahrenstechnik und Chemieingenieurwesen, VDI-Wärmeatlas. 11.Edition, Springer-Verlag Berlin Heidelberg, 2013, ISBN: 978-3-642-19981-3.

[99] Reitz, R.D. and Diwakar, R., Effect of drop breakup on fuel sprays. SAE Technical paper 860469, 1986, https://doi.org/10.4271/860469.

[100] Duronio, F., De Vita, A., Allocca, L., Anatone, M., Gasoline direct injection engines – A review of latest technologies and trends. Part 1: Spray breakup process. Fuel 265, 2020, doi: 10.1016/j.fuel.2019.116948.

[101] Paredi, D., Lucchini, T., D'Errico, G., Onorati, A., Montanaro, A., Allocca, L., and Ianniello, R., Combined Experimental and Numerical Investigation of the ECN Spray G under Different Engine-Like Conditions. SAE Technical Paper 2018-01-0281, 2018, doi:10.4271/2018-01-0281.

[102] Fischer, S., Simulation of the Urea-Water-Solution Preparation and Ammonia Homogenization with a Validated CFD-Model for the Optimization of Automotive SCR Systems. Ph.D. Thesis, Vienna University of Technology, Vienna, Austria, 2012.

[103] Wruck, N., Transientes Sieden von Tropfen beim Wandaufprall. Ph.D. Thesis, RWTH Aachen, Aachen, Germany, 1998.

[104] Panão, M. R. O., Moreira, A. L. N., Thermo- and fluid dynamics characterization of spray cooling with pulsed sprays. Experimental Thermal and Fluid Science 30(2), p. 79-96, 2005, doi: //doi.org/10.1016/j.expthermflusci.2005.03.020.

[105] Fest-Santini, S., Wärmeübergang bei der Spraykühlung mit intermittierenden Srays. Ph.D. Thesis, Otto-von-Guericke-University Magdeburg, Magdeburg, Germany, 2009.

[106] Köpple, F., Untersuchung der Potentiale der numerischen Strömungsberechnung zur Prognose der Partikelemissionen in Ottomotoren mit Direkteinspritzung. Ph.D. Thesis, University of Stuttgart, Stuttgart, Germany, 2015, doi: 10.1007/978-3-658-11138-0.

[107] Köpple, F., Jochmann, P., Kufferath, A., Bargende, M, Investigation of the Parameters Influencing the Spray-Wall Interaction in a GDI Engine – Prerequisite for the Prediction of Particulate Emissions by Numerical Simulation. SAE Int. J. Engines 6(2), p. 911-925, 2013, doi: https://doi.org/10.4271/2013-01-1089.

[108] Zigan, L., Schmitz, I., Flügel, A., Knorsch, T., Wensing, M., Leipertz, A., Effect of Fuel Properties on Spray Breakup and Evaporation Studied for a Multihole Direct Injection Spark Ignition Injector. Energy Fuels 24, pp. 4341-4350, 2010, doi:10.1021/ef1003914.

[109] Ipp, W., Egermann, J., Schmitz, I., Wagner, V., Leipertz, A., 2D Mapping and Quantification of the In-Cylinder Air/Fuel-Ratio in a GDI Engine by Means of LIF and Comparison to Simultaneous Results from 1D Raman Measurements. SAE Technical Paper 2001-01-1977, 2001, doi: https://doi.org/10.4271/2001-01-1977.

[110] Myong, K.-J., Arai, M., Tanaka, T., Senda, J., Fujimoto, H., An Experimental Investigation and Numerical Analysis of Multi-component Fuel Spray. JSME International Journal Series B 47(2), p. 200-206, 2004, doi: https://doi.org/10.1299/jsmeb.47.200.

[111] ASTM D86: Standard Test Method for Distillation of Petroleum Products. American Society for Testing Materials: Philadelphia, PA, USA; Volume 5.01, pp. 237–242.

[112] DIN EN ISO 3405: Petroleum and Related Products from Natural or Synthetic Sources–Determination of Distillation Characteristics at Atmospheric Pressure; Deutsches Institut für Normung e.V., Berlin, 2017.

[113] Poling, B. E., Prausnitz, J.M., O'Connell J. P., The properties of Gases and Liquids", 5th edition, McGraw-Hill, New York, 2001, doi: 10.1036/0070116822.

[114] Fredenslund, A., Jones, R.I., Prausnitz, J.M., Group-Contribution Estimation of Activity Coefficients in Nonideal Liquid Mixtures. AIChE Journal 21, p. 1086-1099, 1975, doi: https://doi.org/10.1002/aic.690210607.

[115] Jess, A., Wasserscheid, P., Chemical Technology, 1st edition, WILEY-VCH Verlag GmbH & Co KGaA, 2013, ISBN: 978-3-527-30446-2.

[116] Greenfield, M.L., Lavoie, G.A., Smith, C.S., Curtis, E.W., Macroscopic Model of the D86 Fuel Volatility Procedure. SAE Technical Paper 982724, 1998, doi: 10.4271/982724.

[117] Abrams, D.S., Prausnitz, J.M., "Statistical Thermodynamics of Liquid Mixtures: A New Expression for the Excess Gibbs Energy of Partly or Completely Miscible Systems", AIChE Journal 21, p. 116-128, 1975, doi: https://doi.org/10.1002/aic.690210115.

[118] Maurer G., Prausnitz, J.M., On the Derivation and Extension of the UNIQUAC Equation. Fluid Phase Equilibrium 2(2), p. 91-99, 1978, doi: https://doi.org/10.1016/0378-3812(78)85002-X.

[119] Batteh, J. J., Curtis, E. W., Modeling Transient Fuel Effects with Alternative Fuels. SAE Technical Paper 2005-01-1127, 2005, doi: 10.4271/2005-01-1127.

[120] National Institute of Standards and Technology, NIST Chemistry WebBook, SRD 69, accessed August 2019. https://webbook.nist.gov/chemistry/fluid/

[121] Kubach, H., Weidenlener, A., Pfeil, J., Koch, T., Kittel, H., Roisman, I., Tropea, C., Investigations on the Influence of Fuel Oil Film Interaction on Pre-Ignition Events in Highly Boosted DI Gasoline Engines. SAE Technical Paper 2018-01-1454, 2018, doi: 10.4271/2018-01-1454.

[122] Splitter, D., Kaul, B., Szybist, J., Speed, L., Zigler, B., Luecke, J., Fuel-Lubricant Interactions on the Propensity for Stochastic Pre-Ignition. SAE Technical Paper 2019-24-0103, 2019, doi: 10.4271/2019-24-0103.

[123] Andrae, J. C. G., Brinck, T., Kalghatgi, G. T., HCCI experiments with toluene reference fuels modeled by a semidetailed chemical kinetic model. Combustion and Flame 155(4), p. 696–712, 2008, doi:10.1016/j.combustflame.2008.05.010.

[124] Morgan, N., Smallbone, A., Bhave, A., Kraft, M., Cracknell, R., Kalghatgi, G., Mapping surrogate gasoline compositions into RON/MON space. Combustion and Flame 157(6), p. 1122-1131, 2010, doi: 10.1016/j.combustflame.2010.02.003.

[125] Kuti, O. A., Yang, S. Y., Hourani, N., Naser, N., Roberts, N. L., Chung, S. H., Sarathy, S. M., A fundamental investigation into the relationship between lubricant composition and fuel ignition quality. Fuel 160, p. 605-613, 2015, doi: https://doi.org/10.1016/j.fuel.2015.08.026.

[126] Wang, F. C.-Y., Zhang, L., Chemical Composition of Group II Lubricant Oil Studied by High-Resolution Gas Chromatography and Comprehensive Two-Dimensional Gas Chromatography. Energy & Fuels 21(6), p. 3477-3483, 2007, doi: https://doi.org/10.1021/ef700407c.

[127] Touchard, S., Fournet, R., Glaude, P. A., Warth, V., Battin-Leclerc, F., Vanhove, G., Ribaucour, M., Minetti, R., Modeling of oxidation of large alkenes at low temperature. Proceedings of the Combustion Institute 30(1), p. 1073-1081, 2005, doi: 10.1016/j.proci.2004.07.004.

[128] Westbrook, C. K., Pitz, J. W., Herbinet, O., Curran, H. J., Silke, E., J., A comprehensive detailed chemical kinetic reaction mechanism for combustion of n-alkane hydrocarbons from n-octane o n-hexadecane. Combustion and Flame 156 (1), p. 181-199, 2009, doi: 10.1016/j.combustflame.2008.07.014.

[129] Sarathy, S. M., Westbrook, C. K., Mehl, M., Pitz, W. J., Togbe, C., Dagaut, P., Wang, H., Oehlschlaeger, M. A., Niemann, U., Seshadri, K., Veloo, P. S., Ji, C., Egolfopoulos, F. N., Lu, T., Comprehensive chemical kinetic modeling of the oxidation of 2-methylalkanes from C_7 to C_{20}. Combustion and Flame 158 (12), p. 2338-2357, 2011, doi: 10.1016/j.combustflame.2011.05.007.

[130] Frühhaber, Jens, Numerische Analyse der Zündung und der turbulenten Flammenausbreitung in Diesel-Gas Dual-Fuel-Motoren. Ph.D. Thesis, Vienna University of Technology, Vienna, Austria, 2022.

[131] Ritzke, J., Andree, S., Theile, M., Henke, B., Schleef, K., Nocke, J., Hassel, E., Simulation of a Dual-Fuel Large Marine Engines using combined 0/1-D and 3-D Approaches. CIMAC Congress, Helsinki, June 6-10, 2016.

[132] Eder, L., Ban, M., Pirker, G., Vujanovic, M., Priesching, P., Wimmer, A., Development and Validation of 3D-CFD Injection and Combustion Models for Dual Fuel Combustion in Diesel Ignited Large Gas Engines. Energies 11(3), 643, 2018, doi: https://doi.org/10.3390/en11030643.

[133] Stiesch, G., Modeling Engine Spray and Combustion Processes. Heat and Mass Transfer. Springer-Verlag Berlin Heidelberg New York, 2003, doi: 10.1007/978-3-662-08790-9.

[134] Scott Goldsborough, S., A chemical kinetically based ignition delay correlation for iso-octane covering a wide range of conditions including the NTC region. Combustion and Flame 156(6), p. 1248-1262, doi: 10.1016/j.combustflame.2009.01.018.

[135] Gauthier, B. M., Davidson, D. F., Hanson, R. K., Shock tube determination of ignition delay times in full-blend and surrogate mixtures. Combustion and Flame 139(4), p. 300-311, 2004, doi: 10.1016/j.combustflame.2004.08.015.

[136] DIN 51435: Test of petroleum products – Determination of boiling range distribution – Gas chromatography method. 2010.

[137] Hessisches Landesamt für Umwelt und Geologie, Auswertung von Mineralöl-Gaschromatogrammen. Handbuch Altlasten, Band 3, Teil 5, Wiesbaden, 2005, ISBN: 3-89026-808-0.

[138] Gey, M. H., Instrumentelle Analytik und Bioanalytik. 2nd edition, Springer-Verlag Berlin Heidelberg, 2008, ISBN: 978-3-540-73803-9.

[139] Distaso, E., Amirante, R., Calò, G., De Palma, P., Tamburrano, P., Reitz, R., Lubricant-Oil-Induced Pre-ignition Phenomena in Modern Gasoline Engines: Using Experimental Data and Numerical Chemistry to Develop a Practical Correlation. SAE Technical Paper 2021-24-0052, 2021, doi: 10.4271/2021-24-0052.

[140] Stauch, R., Lipp, S., Maas, U., Detailed numerical simulations of the autoignition of single n-heptane droplets in air. Combustion and Flame 145(3), p. 533-542, 2006, doi: 10.1016/j.combustflame.2005.12.013.

[141] Stauch, R., Maas, U., The auto-ignition of single n-heptane/iso-octane droplets. International Journal of Heat and Mass Transfer 50(15-16), pp. 3047-3053, 2007, doi: 10.1016/j.ijheatmasstransfer.2006.12.005.

[142] ACEA European Oil Sequences for Service-Fill Oils, Rev. 2, December 2016.

[143] Magar, M., Numerische Untersuchung unkontrollierter vorzeitiger Selbstzündprozess unter motorrelevanten Bedingungen. Ph.D. Thesis, Karlsruhe Institute of Technology, Karlsruhe, Germany, 2016.

[144] Coronel, S. A., Melguizo-Gavilanes, J., Mevel, R., Shepherd, J. E., Experimental and numerical study on moving hot particle ignition. Combustion and Flame 192, p. 495-506, 2018, doi: 10.1016/j.combustflame.2018.02.027.

[145] Glushkov, D.O., Legros, J.-C., Strizhak, P.A., Zakharevich, A.V., Experimental and numerical study of heat transfer and oxidation reaction during ignition of diesel fuel by a hot particle. Fuel 175, p. 105–115, 2016, doi:10.1016/j.fuel.2016.02.042.

[146] Kalghatgi, G.T., Bradley, D., Pre-ignition and 'super-knock' in turbocharged spark-ignition engines. International Journal of Engine Research 13, p. 399–414, 2012, doi:10.1177/1468087411431890.

[147] Douaud, A.; Eyzat, P., Four-Octane-Number Method for Predicting the Anti-Knock Behavior of Fuels and Engines. SAE Technical Paper 780080, 1978.

[148] Rifkin, E.B., Walcutt, C. A, Basis for Understanding Anti-Knock Action. SAE Technical Paper 570046, 1957.

[149] Burger, M., Schmehl, R., Koch, R., Wittig, S., Bauer, H.-J., DNS of droplet-vortex interaction with a Karman vortex street. International Journal of Heat and Fluid Flow 27(2), p. 181-191, 2006, doi: 10.1016/j.ijheatfluidflow.2005.09.004.

[150] Green, S., Fluid Vortices. Kluwer Academic Publishers, Dordrecht: Springer Netherlands, 1995, ISBN: 0792333764

[151] Lienhard, J. H., Synopsis of lift, drag and vortex frequency for rigid circular cylinders. College of Engineering Research Division bulletin 300, Technical Extension Service, Washington State University, 1966.

[152] Williamson, C. H. K., Defining a universal and uontinuous Strouhal-Reynolds number relationship for the laminar vortex shedding of a circular-cylinder. Physics of Fluids 31, p. 2742-2744, 1988, doi: http://dx.doi.org/10.1063/1.866978

[153] Tennekes, H., Lumley, J. L., A first course in turbulence. MIT Press, 1972, ISBN: 9780262200196 0262200198.

[154] Pope, S. B., Tubulent Flows. 4th edition, Cambridge University Press, 2006, ISBN: 978-0-521-59886-6.

[155] Livengood, J. C., Wu, P. C., Correlation of Autoignition phenomena in internal combustion engines and rapid compression machines. Symp. Int. Combust. 5, p. 347-356, 1955, doi: 10.1016/S0082-0784(55)80047-1.

[156] Nishiwaki, K., Hafnan, M., The Determination of Thermal Properties of Engine Combustion Chamber Deposits. SAE Technical paper 2000-01-1215, 2000, doi: https://doi.org/10.4271/2000-01-1215.

[157] Li, K., Liu, Q., Rimmer, S., Huggett, W., Zhang, S., Investigation of the carbon structure of naturally graphitized coals from Central Hunan, China, by density-gradient centrifugation, X-ray diffraction, and high-resolution transmission electron microscopy. International Journal of Coal Geology 232, 2020, doi: https://doi.org/10.1016/j.coal.2020.103628.

[158] Sethian, J. A., Level Set Methods and Fast Marching Methods: evolving interfaces in computational geometry. Fluid mechanics, computer vision, and materials science 3, Cambridge University Press, 1999.

[159] Peters, N., Turbulent Combustion. Cambridge University Press, 2000.

[160] Chen, M., Herrmann, M., Peters, N., Flamelet modelling of lifted turbulent methane/air and propane/air jet diffusion flames. Proceedings of the Combustion Institute 28(1), p. 167-174, 2000, doi: https://doi.org/10.1016/S0082-0784(00)80208-8.

[161] Reinecke, M., Hildebrandt, W., Niemeyer, J. C., Klein, R., Gröbl, A., A new model for deflagration fronts in reactive fluids. Astronomy and Astrophysics 2, p. 1-12, 1999.

[162] Gülder, Ö. L., Correlations of Laminar Combustion Data for Alternative S.I. Engine Fuels. SAE Technical Paper 841000, 1984, doi: https://doi.org/10.4271/841000.

[163] Lackner, M., Palotás, Á. B., Winter, F., Combustion: from basics to applications. WILEY-VCH Verlag GmbH & Co KGaA, 2013, ISBN: 978-3-527-33376-9.

[164] Kreuzwirth, G., Knaus, O., Integrierte thermische Analyse von Zylinder und Kolbengruppe. MTZ – Motortechnische Zeitschrift 77(11), p. 54-59, 2016.

[165] Mahle GmbH, Kolben und motorische Erprobung. ATZ/MTZ Fachbuch, Springer-Vieweg, 2.Auflage, 2015, doi:10.1007/978-3-658-09558-1.

[166] Ratzke, A., Modellierung der Flammenausbreitung und des Flammenlöschens im Gasmotor. Ph.D. Thesis, Gottfried Wilhelm Leibniz University Hannover, Hannover, Germany, 2013.

[167] Mayer, D., Köpple, F., and Bargende, M., Analyzing wall heat transfer modeling in diesel engines supporting numerical investigations of strategies for increasing thermal efficiency. Proceeding of AVL International Simulation Conference, 27 - 29 August, 2017.

[168] Nagle, J., Strickland-Constable, R. F., Oxidation of carbon between 1000-2000 °C. Proceedings of the 5th Carbon Conference 1, p. 154-164, 1962.

[169] Walls, J. R., Strickland-Constable, R. F., Oxidation of carbon between 1000-2400 °C. Carbon 1(3), p. 333-338, 1964, doi: https://doi.org/10.1016/0008-6223(64)90288-X.

[170] Kelesidis, G. A., Pratsinis, S. E., Estimating the internal and surface oxidation of soot agglomerates, Combustion and Flame 209 , p. 493-499, 2019, doi: https://doi.org/10.1016/j.combustflame.2019.08.001.

[171] Vander Wal, R. L., Tomasek, A. J., Soot oxidation: dependence upon initial nanostructure. Combustion and Flame 134 (1-2), p. 1-9, 2003, doi: https://doi.org/10.1016/S0010-2180(03)00084-1.

[172] Camacho, J., Tao, Y., Wang, H., Kinetics of nascent soot oxidation by molecular oxygen in a flow reactor. Proceedings of the Combustion Institute 35, p. 1887-1894, 2015, doi: http://dx.doi.org/10.1016/j.proci.2014.05.095.

[173] Lide, D. R., ed., CRC Handbook of Chemistry and Physics. Internet Version 2005, <http://www.hbcpnetbase.com>, CRC Press, Boca Raton, FL, 2005.

A-1. Appendix

A-1.1. Scientific contributions

In the context of this dissertation, the following listed scientific contributions were published, the content of which is partly congruent with the present work.

Contribution	Status
Zöbinger, N., Lauer, T., Numerical Investigation of the Influence of Oil Dilution on the Ability to Initiate a Pre-Ignition Combustion. SAE Int. J. Advances & Curr. Prac. in Mobility 2(4), p. 1935-1962, 2020, doi:10.4271/2020-01-0611.	Published
Zöbinger, N., Schweizer, T., Lauer, T., Kubach, H., Koch, T., Experimental and Numerical Analysis on Two-Phase Induced Low-Speed Pre-Ignition. Energies 14(16), 5063, 2021. doi: https://doi.org/10.3390/en14165063.	Published
Schweizer, T., Kubach, H., Zöbinger, N., Lauer, T., Eder, M., Grabner, P., Schießl, R., Liu, C., Initial Pre-Ignition. FVV Spring Conference, Frankfurt, Germany, 2021.	Published
Schweizer, T., Kubach, H., Zöbinger, N., Lauer, T., Eder, M., Grabner, P., Schießl, R., Liu, C., Initial Pre-ignition. Final Report of the FVV-project no. 1328, FVV-Frankfurt am Main, 2021.	Published
Schweizer, T.; Zöbinger, N.; Kubach, H., Lauer, T.; Koch, T. Experimental and numerical Low-speed pre-ignition analysis and mechanism synthesis on a turbocharged gasoline engine with direct injection. SAE International Journal of Engines 16(3), 2022, doi: 10.4271/03-16-03-0018.	Published
Zöbinger, N., Lauer, T., Prediction of the wall film composition in a direct injection SI-engine using the UNIFAC method. International Multidimensional Engine Modeling User's Group meeting at the SAE Congress, Detroit, Michigan, USA, 2020.	Accepted (conference canceled)

A-1.2. Validation of the 0D distillation model – extended data

The section "6.2.3. Implementation of a multi-component fuel surrogate" already showed an excerpt of sample surrogate fluids used for validation. In this Appendix section, all surrogate formulations used to validate the 0D distillation model are shown. Table A-1 shows the specific surrogate formulations taken from the literature and Figure A-1 shows the results achieved using the established distillation model. All validation cases are in good agreement with measurement data, although a slight shift towards higher predicted distillation temperatures can be observed in some cases. The figures are sorted by the share of ethanol in the surrogate formulation.

Table A-1: Surrogate formulations published by Batteh [119] and Greenfield [116] and used for validation.

Species	Chemical group	BP [K] @ 1 bar	Indolene [%-m/m]	E85 [%-m/m]	Syngas [%-m/m]	Hesitation fuel [%-m/m]	Synfuel [%-m/m]	Synfuel + 10.5 % Ethanol [%-m/m]
n-butane	Paraffin	272.65	4.00	3.00	-	2.66	-	-
Iso-pentane	Iso-paraffin	301.15	16.00	1.00	40.00	-	-	-
n-pentane	Paraffin	308.85	-	-	-	12.95	17.03	15.25
cyclopentane	Naphthenic	321.95	-	-	5.00	-	-	-
1-hexene	Olefin	336.25	-	-	5.00	-	-	-
n-hexane	Paraffin	342.15	2.50	7.00	-	-	-	-
Ethanol	Oxygenate (Alcohol)	351.47	-	86.00	-	-	-	10.48
Cyclohexane	Naphthenic	353.45	-	-	-	18.43	24.23	21.69
Iso-octane	Iso-paraffin	372.15	32.00	1.00	-	-	-	-
Toluene	Aromatic	384.15	25.50	-	18.00	13.19	17.35	15.53
n-octane	Paraffin	399.15	-	-	25.00	14.53	19.11	17.11
Ethylbenzene	Aromatic	408.85	-	-	-	11.19	12.71	11.38
n-decane	Paraffin	447.15	-	-	-	21.67	8.49	7.60
1,2,3-trimethylbenzene (TMB)	Aromatic	449.15	18.00	2.00	7.00	-	-	-
Naphthalene	Aromatic	490.55	-	-	-	5.38	1.08	1.05
Tridecane	Paraffin	508.15	2.00	-	-	-	-	-

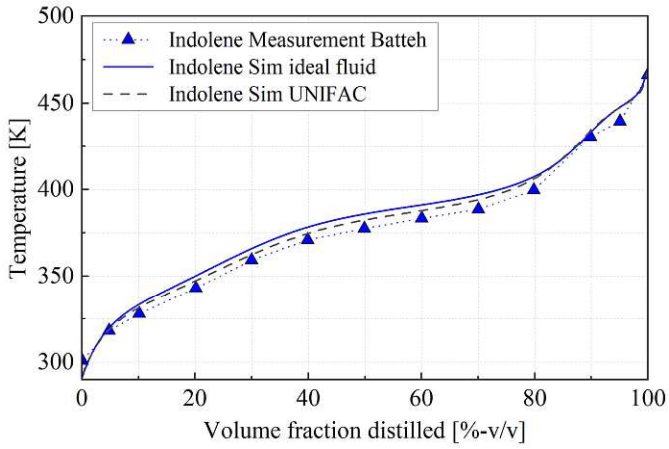

(**a**) „Indolene“

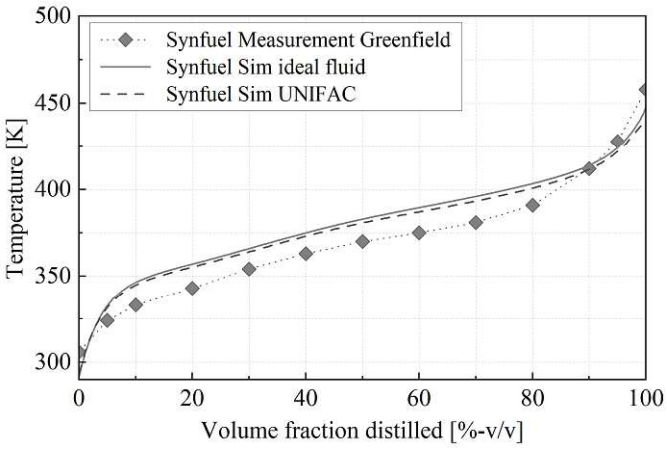

(**b**) „Synfuel“

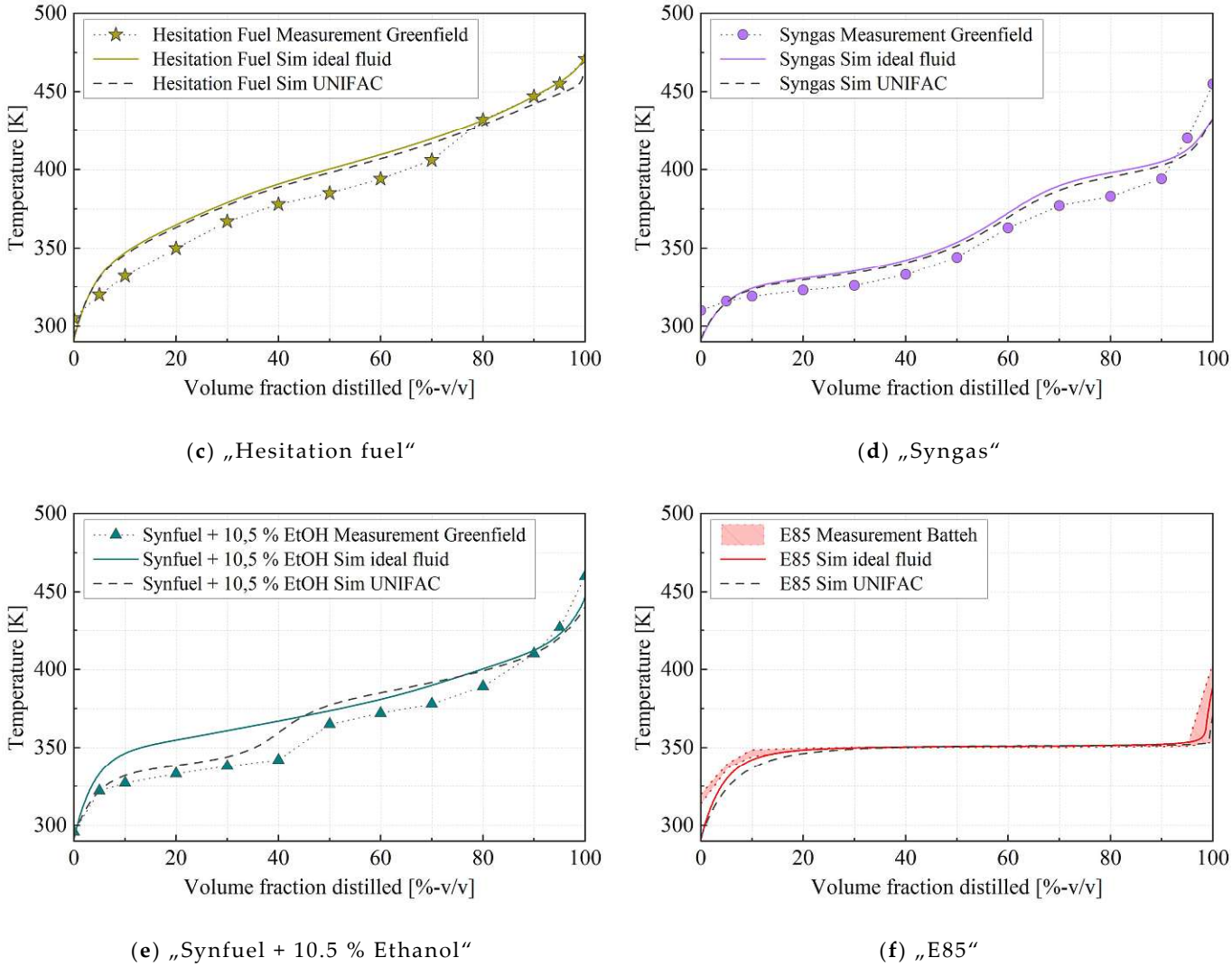

Figure A-1: Comparison of measured and predicted distillation curve for (**a**) Indolene, (**b**) Synfuel, (**c**) Hesitation fuel, (**d**) Syngas, (**e**) Synfuel + 10.5 % Ethanol, and (**f**) E85.

A-1.3. Thermodynamic properties of the oil surrogate species

In order to define the thermodynamic properties of large n-alkane molecules, the following databases are used: VDI Heat atlas [98], NIST thermophysical database [120], and the database of the CRC-Handbook of chemistry [173]. The first two mentioned databases provide a detailed view of all species properties by applying fitted polynomial functions (PPDS-equations) up to a chain length of $C_{19}H_{40}$ (n-alkanes). The CRC-Handbook of Chemistry additionally provides the saturation pressure curve for n-alkanes from $C_{20}H_{42}$ up to $C_{29}H_{60}$ at discrete pressure points. The GC analysis showed in section 7.2.2. revealed that the investigated lubricating oil consists of even larger molecules than it is covered in the aforementioned databases. Consequently, the missing data is predicted by extrapolating the existing databases.

In order to extrapolate a temperature-dependent behavior of larger alkanes, a two-step extrapolation procedure is used, as shown in Figure A-2. In the first step, a carbon chain length-based extrapolation of data is performed. Figure A-3 shows all available data from the databases as solid symbols. Furthermore, the fitted trend function is displayed as dashed lines.

All used fit functions and the corresponding fitted parameters are summarized next to the individual property. Discrete data points can be forecasted for larger molecule sizes by using the established trend functions. In a second extrapolation step, the predicted data is used to fit a temperature-dependent function based on the behavior of $C_{19}H_{40}$. This species is used as a reference since it is the largest alkane where all fluid properties are available. In Figure A-4 the resulting temperature-dependent fit functions and the corresponding parameters for the used oil species are shown. Additionally, the chain length-based forecasted data are shown as solid symbols.

Finally, it should be noted that although the extrapolation of the fluid data is done carefully, it is always a source of inaccuracy.

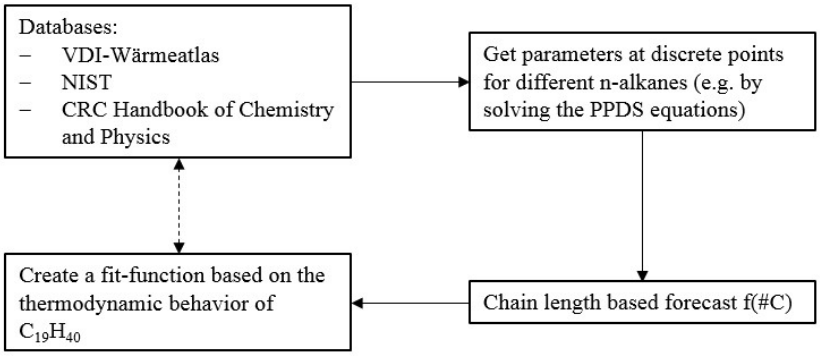

Figure A-2: Methodology overview of the extrapolation procedure.

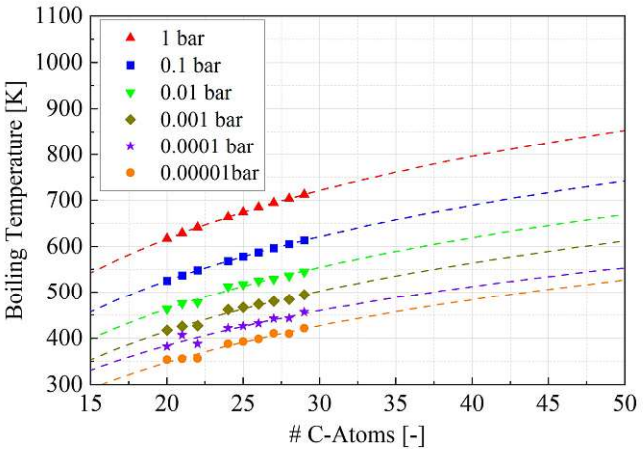

(a)

Fitted function Saturation pressure $p_s(\#C) = k * ln(\#C) + d$	**k**	**d**	**R²**
1 bar	258.48	-157.65	1.000
0.1 bar	237.01	-184.71	1.000
0.01 bar	225.15	-211.21	0.976
0.001 bar	214.64	-227.62	0.976
0.0001 bar	184.93	-169.55	0.919
0.00001 bar	195.61	-238.26	0.966

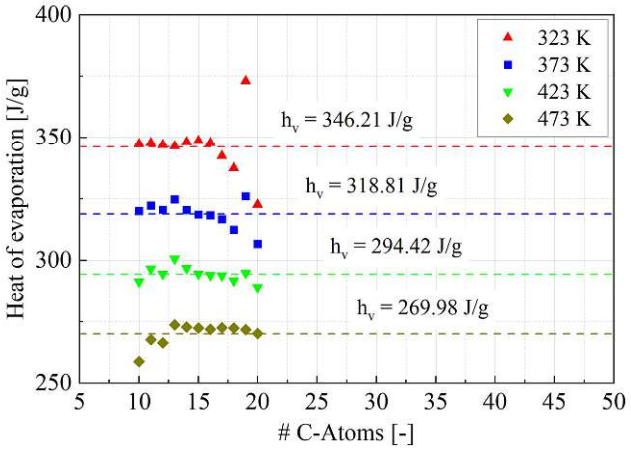

(**b**)

Fitted function Heat of evaporation $\Delta h_v(\#C) = d$	**Averaged value**
323 K	269.98
373 K	294.42
423 K	318.81
473 K	346.21

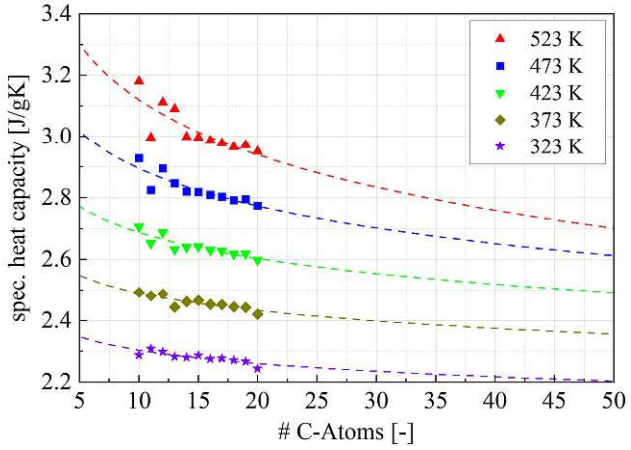

(**c**)

Fitted function Spec. heat capacity $c_p(\#C) = k * ln(\#C) + d$	**k**	**d**	**R²**
323 K	-0.260	3.720	0.658
373 K	-0.175	3.299	0.745
423 K	-0.121	2.967	0.786
473 K	-0.083	2.682	0.776
523 K	-0.062	2.447	0.707

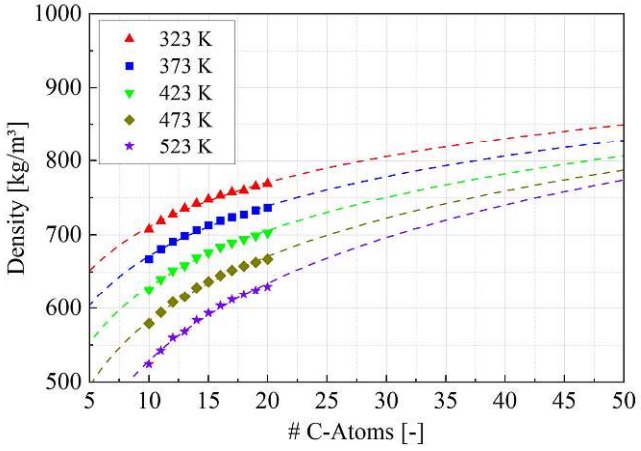

(**d**)

Fitted function Density $\rho(\#C) = k * ln(\#C) + d$	**k**	**d**	**R²**
323 K	86.341	512.058	0.989
373 K	97.276	447.589	0.991
423 K	110.116	375.941	0.992
473 K	127.077	290.411	0.993
523 K	152.151	178.918	0.992

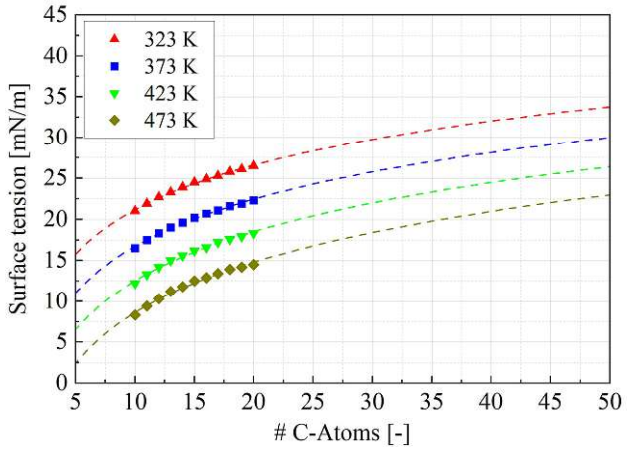

(e)

Fitted function Surface tension $\sigma(\#C) = k * ln(\#C) + d$	**k**	**d**	**R²**
323 K	7.812	3.198	0.997
373 K	8.246	-2.258	0.996
423 K	8.626	-7.333	0.992
473 K	8.903	-11.868	0.990

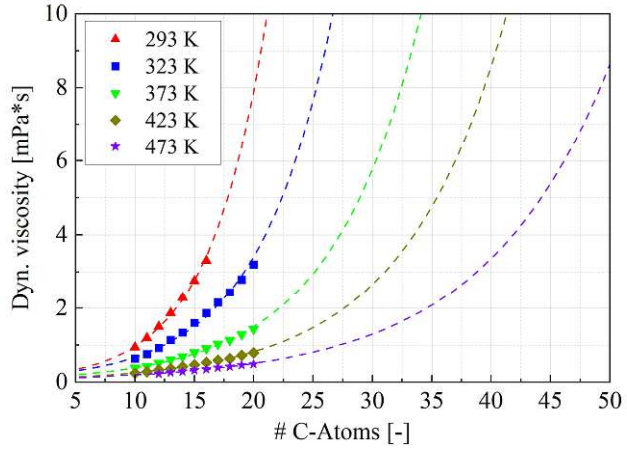

(f)

Fitted function Dyn. viscosity $\eta(\#C) = k * e^{(d*(\#C))}$	**k**	**d**	**R²**
293 K	0.119	0.209	0.997
323 K	0.134	0.162	0.993
373 K	0.102	0.135	0.995
423 K	0.0789	0.117	0.993
473 K	0.0763	0.0945	0.994

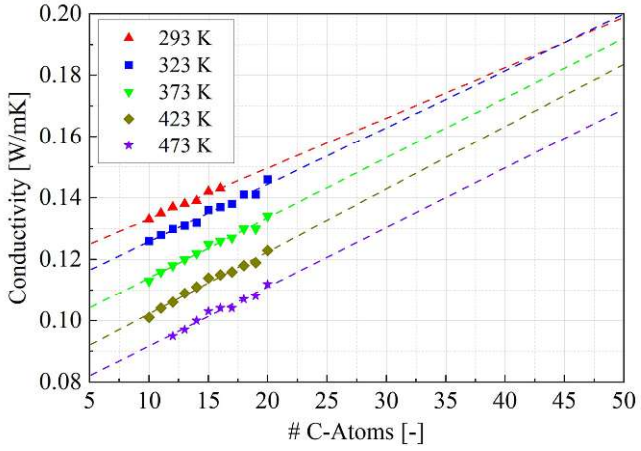

(g)

Fitted function Conductivity $\lambda(\#C) = k * (\#C) + d$	**k**	**d**	**R²**
293 K	0.00164	0.117	0.983
323 K	0.00185	0.107	0.978
373 K	0.00195	0.0944	0.986
423 K	0.00204	0.0818	0.982
473 K	0.00193	0.0724	0.967

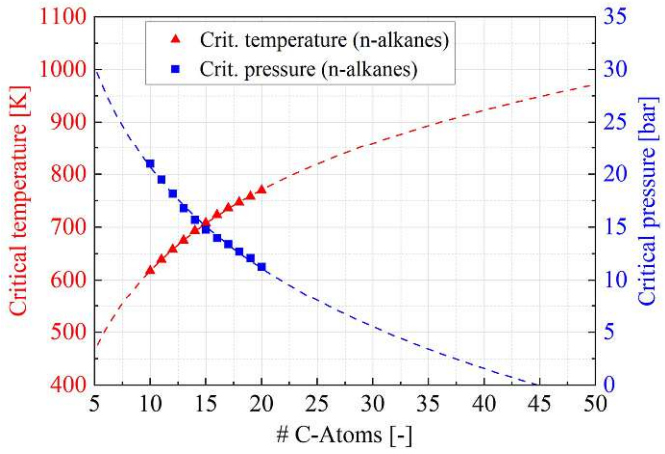

(**h**)

Fitted function Critical Prop. $T_{crit}, p_{crit}(\#C) = k * ln(\#C) + d$	**k**	**d**	**R²**
T_{crit}	219.738	112.286	1.000
p_{crit}	-13.778	52.398	0.994

Figure A-3: Carbon chain length-based trend functions.

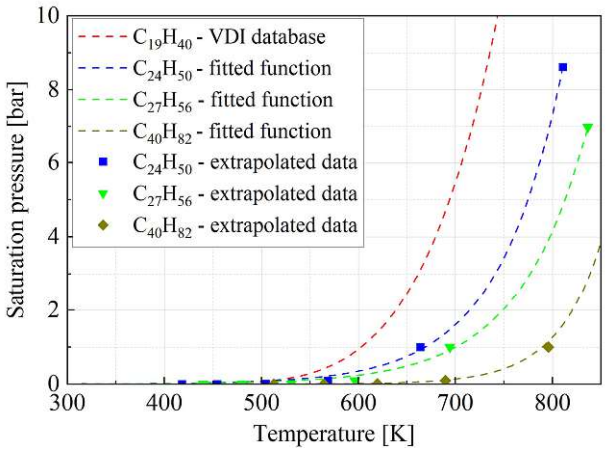

(**a**)

Fitted function Saturation pressure $p_s(T) = A * e^{(B*T)}$	**A**	**B**	**R²**
$C_{24}H_{50}$	3.966	0.01516	1.000
$C_{27}H_{56}$	4.659	0.01425	0.999
$C_{40}H_{82}$	0.00244	0.02221	1.000

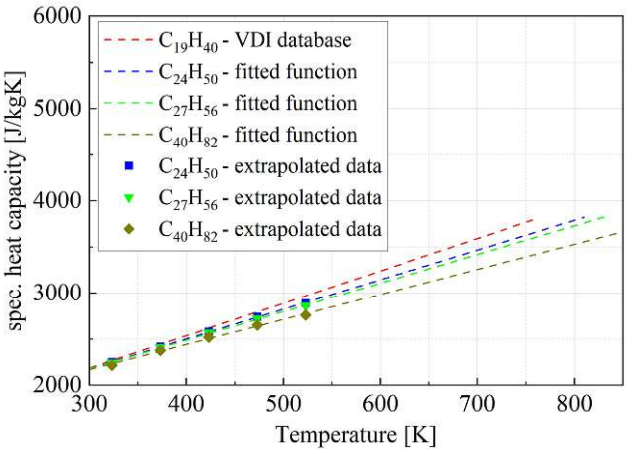

(**b**)

Fitted function Spec. heat capacity $c_p(\#C) = A * T + B$	**A**	**B**	**R²**
$C_{24}H_{50}$	3.2202	1213.8	1.000
$C_{27}H_{56}$	3.1053	1245.9	0.999
$C_{40}H_{82}$	2.7218	1352.9	0.995

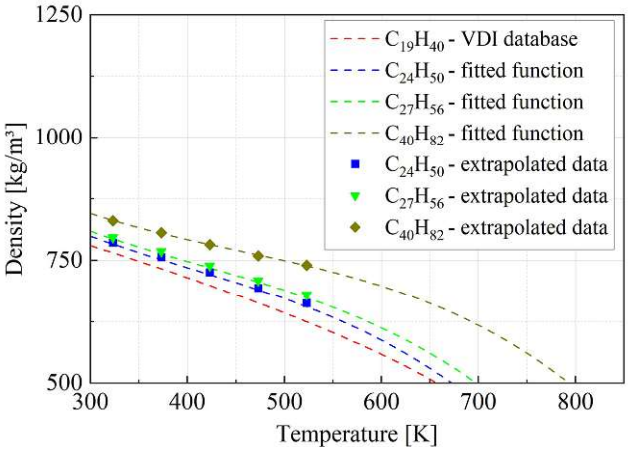

(c)

Fitted function Density $\rho(T) = A * T^3 + B * T^2 + C * T + D$	A [x10^{-6}]	B [x10^{-3}]	C	D	R^2
$C_{24}H_{50}$	-3.746	4.5455	-2.438	1221.76	1.000
$C_{27}H_{56}$	-3.488	4.3316	-2.358	1221.23	1.000
$C_{40}H_{82}$	-3.242	4.4155	-2.424	1262.89	1.000

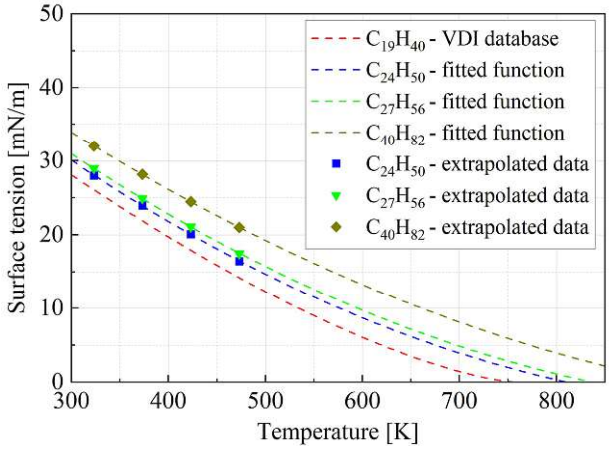

(d)

Fitted function Surface tension $\sigma(T) = A * T^2 + B * T + C$	A [x10^{-5}]	B	C	R^2
$C_{24}H_{50}$	5.8307	-0.1237	61.937	1.000
$C_{27}H_{56}$	5.4894	-0.1201	62.057	1.000
$C_{40}H_{82}$	4.4754	-0.1092	62.649	1.000

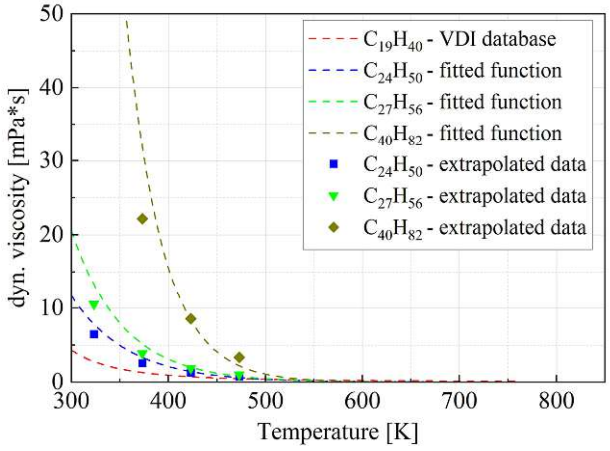

(e)

Fitted function Dyn. viscosity $\eta(T) = A * e^{(B*T)}$	A	B [x10^{-2}]	R^2
$C_{24}H_{50}$	1989.58	-1.712	0.960
$C_{27}H_{56}$	5908.11	-1.887	0.957
$C_{40}H_{82}$	6603.26	-2.664	0.945

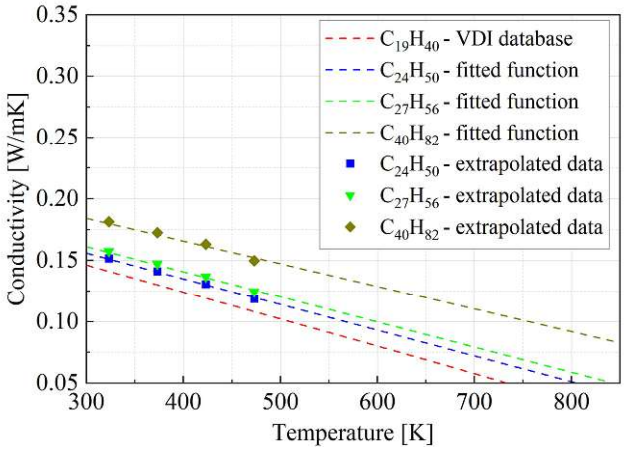

(f)

Fitted function Conductivity $\lambda(T) = A * T + B$	**A** [x10^{-4}]	**B**	**R²**
$C_{24}H_{50}$	-2.0952	0.21878	0.996
$C_{27}H_{56}$	-2.0483	0.22267	0.994
$C_{40}H_{82}$	-1.8452	0.23950	0.968

Figure A-4: Resulting temperature-dependent fit functions of the used oil surrogate species.

A-1.4. Results of the 4D ignition delay map simulations

All simulation results concerning the 4D ignition delay map are summarized in Table A-2. For calculation purposes, data points are interpolated stepwise mono-dimensional by taking advantage of the found characteristic described in section 8.2.

Table A-2: 4D ignition delay map.

T_P [K]	T_G [K]	p_G [bar]	λ_{TRF} [-]	t_{ign} [ms]		T_P [K]	T_G [K]	p_G [bar]	λ_{TRF} [-]	t_{ign} [ms]
1000	500	10	0.5	147.72		1000	500	10	1	723.08
1000	500	30	0.5	23.65		1000	500	30	1	138.90
1000	500	50	0.5	11.49		1000	500	50	1	69.53
1200	500	10	0.5	13.80		1200	500	10	1	35.27
1200	500	30	0.5	4.22		1200	500	30	1	8.53
1200	500	50	0.5	3.26		1200	500	50	1	5.25
1300	500	10	0.5	5.47		1300	500	10	1	10.92
1300	500	30	0.5	2.62		1300	500	30	1	3.38
1300	500	50	0.5	2.45		1300	500	50	1	2.47
1400	500	10	0.5	2.75		1400	500	10	1	4.08
1400	500	30	0.5	2.04		1400	500	30	1	1.80
1400	500	50	0.5	2.14		1400	500	50	1	1.60
1500	500	10	0.5	1.73		1500	500	10	1	1.75
1500	500	30	0.5	1.82		1500	500	30	1	1.19
1500	500	50	0.5	2.02		1500	500	50	1	1.26
1600	500	10	0.5	1.34		1600	500	10	1	0.90
1600	500	30	0.5	1.73		1600	500	30	1	0.93
1600	500	50	0.5	1.97		1600	500	50	1	1.10
2000	500	10	0.5	1.17		2000	500	10	1	0.44
2000	500	30	0.5	1.67		2000	500	30	1	0.74
2000	500	50	0.5	1.92		2000	500	50	1	0.98
1000	575	10	0.5	67.22		1000	575	10	1	239.09
1000	575	30	0.5	13.05		1000	575	30	1	56.94
1000	575	50	0.5	6.98		1000	575	50	1	30.13

T_P [K]	T_G [K]	p_G [bar]	λ_{TRF} [-]	t_{ign} [ms]		T_P [K]	T_G [K]	p_G [bar]	λ_{TRF} [-]	t_{ign} [ms]
1200	575	10	0.5	9.80		1200	575	10	1	22.18
1200	575	30	0.5	3.33		1200	575	30	1	6.06
1200	575	50	0.5	2.64		1200	575	50	1	3.86
1300	575	10	0.5	4.26		1300	575	10	1	7.70
1300	575	30	0.5	2.20		1300	575	30	1	2.62
1300	575	50	0.5	2.05		1300	575	50	1	2.00
1400	575	10	0.5	2.25		1400	575	10	1	3.11
1400	575	30	0.5	1.75		1400	575	30	1	1.48
1400	575	50	0.5	1.81		1400	575	50	1	1.36
1500	575	10	0.5	1.46		1500	575	10	1	1.42
1500	575	30	0.5	1.56		1500	575	30	1	1.02
1500	575	50	0.5	1.70		1500	575	50	1	1.09
1600	575	10	0.5	1.13		1600	575	10	1	0.77
1600	575	30	0.5	1.48		1600	575	30	1	0.81
1600	575	50	0.5	1.66		1600	575	50	1	0.97
2000	575	10	0.5	0.98		2000	575	10	1	0.39
2000	575	30	0.5	1.42		2000	575	30	1	0.65
2000	575	50	0.5	1.62		2000	575	50	1	0.86
1000	650	10	0.5	33.38		1000	650	10	1	87.59
1000	650	30	0.5	7.85		1000	650	30	1	24.25
1000	650	50	0.5	4.59		1000	650	50	1	13.42
1200	650	10	0.5	7.06		1200	650	10	1	14.19
1200	650	30	0.5	2.64		1200	650	30	1	4.26
1200	650	50	0.5	2.17		1200	650	50	1	2.86
1300	650	10	0.5	3.35		1300	650	10	1	5.53
1300	650	30	0.5	1.83		1300	650	30	1	2.05
1300	650	50	0.5	1.74		1300	650	50	1	1.63
1400	650	10	0.5	1.86		1400	650	10	1	2.40
1400	650	30	0.5	1.47		1400	650	30	1	1.23
1400	650	50	0.5	1.55		1400	650	50	1	1.15
1500	650	10	0.5	1.23		1500	650	10	1	1.17
1500	650	30	0.5	1.32		1500	650	30	1	0.87
1500	650	50	0.5	1.46		1500	650	50	1	0.95
1600	650	10	0.5	0.96		1600	650	10	1	0.66
1600	650	30	0.5	1.25		1600	650	30	1	0.71
1600	650	50	0.5	1.42		1600	650	50	1	0.85
2000	650	10	0.5	0.82		2000	650	10	1	0.34
2000	650	30	0.5	1.20		2000	650	30	1	0.57
2000	650	50	0.5	1.38		2000	650	50	1	0.76
1000	725	10	0.5	17.72		1000	725	10	1	35.73
1000	725	30	0.5	5.05		1000	725	30	1	10.94
1000	725	50	0.5	3.18		1000	725	50	1	6.43
1200	725	10	0.5	5.13		1200	725	10	1	9.19
1200	725	30	0.5	2.10		1200	725	30	1	3.03
1200	725	50	0.5	1.74		1200	725	50	1	2.13
1300	725	10	0.5	2.65		1300	725	10	1	4.02
1300	725	30	0.5	1.51		1300	725	30	1	1.62
1300	725	50	0.5	1.45		1300	725	50	1	1.33
1400	725	10	0.5	1.54		1400	725	10	1	1.88
1400	725	30	0.5	1.24		1400	725	30	1	1.02
1400	725	50	0.5	1.30		1400	725	50	1	0.98
1500	725	10	0.5	1.04		1500	725	10	1	0.96
1500	725	30	0.5	1.11		1500	725	30	1	0.75
1500	725	50	0.5	1.23		1500	725	50	1	0.82
1600	725	10	0.5	0.82		1600	725	10	1	0.57
1600	725	30	0.5	1.05		1600	725	30	1	0.62
1600	725	50	0.5	1.19		1600	725	50	1	0.74

T_P [K]	T_G [K]	p_G [bar]	λ_{TRF} [-]	t_{ign} [ms]		T_P [K]	T_G [K]	p_G [bar]	λ_{TRF} [-]	t_{ign} [ms]
2000	725	10	0.5	0.69		2000	725	10	1	0.30
2000	725	30	0.5	1.00		2000	725	30	1	0.50
2000	725	50	0.5	1.15		2000	725	50	1	0.66
1000	500	10	0.8	407.89		1000	500	10	1.2	1382.62
1000	500	30	0.8	74.57		1000	500	30	1.2	235.25
1000	500	50	0.8	35.84		1000	500	50	1.2	121.66
1200	500	10	0.8	24.77		1200	500	10	1.2	48.47
1200	500	30	0.8	6.13		1200	500	30	1.2	11.89
1200	500	50	0.8	3.94		1200	500	50	1.2	7.20
1300	500	10	0.8	8.18		1300	500	10	1.2	14.25
1300	500	30	0.8	2.68		1300	500	30	1.2	4.49
1300	500	50	0.8	2.11		1300	500	50	1.2	3.28
1400	500	10	0.8	3.28		1400	500	10	1.2	5.07
1400	500	30	0.8	1.56		1400	500	30	1.2	2.33
1400	500	50	0.8	1.49		1400	500	50	1.2	2.08
1500	500	10	0.8	1.52		1500	500	10	1.2	2.09
1500	500	30	0.8	1.12		1500	500	30	1.2	1.51
1500	500	50	0.8	1.25		1500	500	50	1.2	1.63
1600	500	10	0.8	0.83		1600	500	10	1.2	1.08
1600	500	30	0.8	0.92		1600	500	30	1.2	1.18
1600	500	50	0.8	1.14		1600	500	50	1.2	1.40
2000	500	10	0.8	0.43		2000	500	10	1.2	0.60
2000	500	30	0.8	0.77		2000	500	30	1.2	0.98
2000	500	50	0.8	1.04		2000	500	50	1.2	1.29
1000	575	10	0.8	151.99		1000	575	10	1.2	352.02
1000	575	30	0.8	32.87		1000	575	30	1.2	89.99
1000	575	50	0.8	16.73		1000	575	50	1.2	49.40
1200	575	10	0.8	16.25		1200	575	10	1.2	29.37
1200	575	30	0.8	4.47		1200	575	30	1.2	8.14
1200	575	50	0.8	3.00		1200	575	50	1.2	5.30
1300	575	10	0.8	5.97		1300	575	10	1.2	9.78
1300	575	30	0.8	2.14		1300	575	30	1.2	3.39
1300	575	50	0.8	1.74		1300	575	50	1.2	2.60
1400	575	10	0.8	2.56		1400	575	10	1.2	3.79
1400	575	30	0.8	1.31		1400	575	30	1.2	1.89
1400	575	50	0.8	1.28		1400	575	50	1.2	1.74
1500	575	10	0.8	1.25		1500	575	10	1.2	1.69
1500	575	30	0.8	0.96		1500	575	30	1.2	1.29
1500	575	50	0.8	1.08		1500	575	50	1.2	1.39
1600	575	10	0.8	0.71		1600	575	10	1.2	0.92
1600	575	30	0.8	0.80		1600	575	30	1.2	1.03
1600	575	50	0.8	0.99		1600	575	50	1.2	1.23
2000	575	10	0.8	0.38		2000	575	10	1.2	0.52
2000	575	30	0.8	0.67		2000	575	30	1.2	0.86
2000	575	50	0.8	0.91		2000	575	50	1.2	1.12
1000	650	10	0.8	61.17		1000	650	10	1.2	120.47
1000	650	30	0.8	15.35		1000	650	30	1.2	36.10
1000	650	50	0.8	8.32		1000	650	50	1.2	20.74
1200	650	10	0.8	10.82		1200	650	10	1.2	18.13
1200	650	30	0.8	3.28		1200	650	30	1.2	5.64
1200	650	50	0.8	2.29		1200	650	50	1.2	3.75
1300	650	10	0.8	4.41		1300	650	10	1.2	6.83
1300	650	30	0.8	1.72		1300	650	30	1.2	2.60
1300	650	50	0.8	1.44		1300	650	50	1.2	2.07
1400	650	10	0.8	2.02		1400	650	10	1.2	2.88
1400	650	30	0.8	1.10		1400	650	30	1.2	1.54
1400	650	50	0.8	1.10		1400	650	50	1.2	1.45

T_P [K]	T_G [K]	p_G [bar]	λ_{TRF} [-]	t_{ign} [ms]		T_P [K]	T_G [K]	p_G [bar]	λ_{TRF} [-]	t_{ign} [ms]
1500	650	10	0.8	1.03		1500	650	10	1.2	1.37
1500	650	30	0.8	0.83		1500	650	30	1.2	1.09
1500	650	50	0.8	0.94		1500	650	50	1.2	1.19
1600	650	10	0.8	0.61		1600	650	10	1.2	0.79
1600	650	30	0.8	0.70		1600	650	30	1.2	0.89
1600	650	50	0.8	0.86		1600	650	50	1.2	1.07
2000	650	10	0.8	0.33		2000	650	10	1.2	0.45
2000	650	30	0.8	0.59		2000	650	30	1.2	0.74
2000	650	50	0.8	0.79		2000	650	50	1.2	0.97
1000	725	10	0.8	27.10		1000	725	10	1.2	46.56
1000	725	30	0.8	7.78		1000	725	30	1.2	15.11
1000	725	50	0.8	4.54		1000	725	50	1.2	9.16
1200	725	10	0.8	7.29		1200	725	10	1.2	11.36
1200	725	30	0.8	2.42		1200	725	30	1.2	3.91
1200	725	50	0.8	1.76		1200	725	50	1.2	2.73
1300	725	10	0.8	3.30		1300	725	10	1.2	4.84
1300	725	30	0.8	1.38		1300	725	30	1.2	2.01
1300	725	50	0.8	1.20		1300	725	50	1.2	1.66
1400	725	10	0.8	1.61		1400	725	10	1.2	2.21
1400	725	30	0.8	0.93		1400	725	30	1.2	1.26
1400	725	50	0.8	0.94		1400	725	50	1.2	1.22
1500	725	10	0.8	0.86		1500	725	10	1.2	1.12
1500	725	30	0.8	0.71		1500	725	30	1.2	0.93
1500	725	50	0.8	0.82		1500	725	50	1.2	1.02
1600	725	10	0.8	0.53		1600	725	10	1.2	0.67
1600	725	30	0.8	0.61		1600	725	30	1.2	0.77
1600	725	50	0.8	0.75		1600	725	50	1.2	0.92
2000	725	10	0.8	0.29		2000	725	10	1.2	0.40
2000	725	30	0.8	0.51		2000	725	30	1.2	0.62
2000	725	50	0.8	0.69		2000	725	50	1.2	0.84